DEEP-DRAFT VESSEL WAKE AND WIND WAVE HYDRODYNAMICS NEAR A MIXED-SEDIMENT EMBANKMENT IN GALVESTON BAY, TEXAS

A Thesis

by

WILLIAM PATRICK FULLER

Submitted to the Graduate and Professional School of
Texas A&M University
in partial fulfillment of the requirements for the degree of

MASTER OF SCIENCE

Chair of Committee,	Jens Figlus
Committee Members,	Timothy Dellapenna
	Russell Feagin
Head of Department,	Sharath Girimaji

December 2021

Major Subject: Ocean Engineering

Copyright 2021 William Fuller

Abstract

Vessel-generated waves are well-documented sources for a substantial amount of the energy impacting shorelines and embankments lining shipping channels. An approximately year-long study was conducted in Galveston Bay, Texas adjacent to the Houston Ship Channel, one of the busiest commercial navigation lanes in the United States. Hydrodynamic data were collected at two research platforms just offshore of a beneficial-use dredge material dike approximately one kilometer eastward of the ship channel. The hydrodynamic data were then analyzed through time-localizing signal analysis techniques known as wavelet transforms. Wavelet transforms facilitate the use of time-frequency domain transformations on nonstationary data (i.e., hydrodynamic bursts containing vessel wake signatures). Time-localizing abilities are the major shortcoming to the standard signal-analysis techniques utilizing Fourier-based transformations. An algorithm was constructed with the wavelet analysis results to identify wake events in the measured data via usage of multiple statistical measures, linear wave theory principles, and hydrodynamic signal behaviors unique to wake events. Data were then investigated for correlations with vessel traffic information, thereby providing direct associations between the observed wake effects and the specific deep-draft vessel inducing the wake event. Results confirmed that wake events, particularly those from inbound traveling deep-draft vessels, were responsible for an outsized portion of the total wave energy impacting the site. Although occurring during less than 5% of the study period, inbound wake events accounted for just over 20% of the total measured wave energy. The median maximum wave energy per minute of inbound and outbound wake events were about 9 and 1.5 times larger than that of wind-only periods, respectively. The strongest correlation between wake events and vessel traffic was by the nondimensional velocity head and length Froude number for inbound vessels with an R^2 between 0.44 and 0.52 depending on the tidal elevation. The presented data analysis helps quantify the hydrodynamic energy resulting from vessel traffic available to drive shallow-bay sediment dynamics and shoreline erosion and enables predictions based on expected future vessel traffic volumes and patterns. In addition, this extensive data set is being used to improve our capability to numerically model ship wakes and their impacts in shallow-bay systems.

Contributors and Funding Sources

Contributors

I would like to give a special thanks to the members of my advisory committee – Dr. Jens Figlus, Dr. Tim Dellapenna, and Dr. Rusty Feagin for backing me throughout my graduate journey, from start to finish. The time, effort, and expertise each of the Professors lent to me and this project was invaluable, and I could not have asked for a better cadre of dedicated mentors. Some of my favorite moments from this chapter of my life are the site visits and following meals shared after a long day's work, memories I will never forget. I keenly hope that I will be able to pay their contributions forward for the next generation of future engineers sometime down the road.

The next shout-out is to the colleagues who assisted this project, whether through helping in field work or conceptual discussions. Most are current or former members of the Texas A&M Coastal Engineering Lab spearheaded by Dr. Figlus, namely Dr. Katherine Anarde, Dr. Tariq Alrushaid, Mick Prouse, and Fangzhou Tong. The main colleague outside of the lab group I'd like to recognize is Dr. Thomas Huff, who was an absolute pleasure to work alongside during the several site visits he kindly joined.

This project would have never left the ground were it not for the professionals from the U.S. Army Corps of Engineers who enabled and assisted the data collection side of the project. This includes Dr. Mike Ramirez, Dr. Joseph Gailani, Dr. Richard Styles, and Douglass Krafft from the Engineer Research and Development Center, and Coraggio Maglio from the Galveston District.

I finally want to thank my family who have supported me, not just during this project, but throughout my entire life. Knowing I had everyone believing in me carried me forward during trying times more than once, and I doubt I would be where I am today were it not for the unconditional love and support that they continuously sent my way.

Funding Sources

This research was supported by the U.S. Army Corps of Engineers through Cooperative Ecosystem Studies Unit (CESU) agreement No. W912HZ-17-2-0023: "In-situ measurements of physical forces and biological parameters in coastal and estuarine systems, Galveston District.

Table of Contents

List of Figures

List of Tables

1.0 Introduction

1.1 Background

Contemporary studies estimate that the maritime transportation industry facilitates upwards of 80% of all international trade by volume [UN, 2017]. Societal reliance on the tankers and bulk carriers comprising the global fleet indicates these vessels will remain common throughout our local waterways into the foreseeable future. Along with the economic opportunities arising from these massive vessels are also several undesirable consequences. One of the main concerns is the inevitable generation of wake phenomena along shorelines and embankments.

This paper outlines the work completed as part of a Master's Thesis in Ocean Engineering. The work aimed to advance our state-of-the-art coastal protection capabilities by providing novel insights on the impacts of vessel-generated wake (herein VGW) events along a beneficial-use mixed sediment dike placed adjacent to a deep-draft navigation channel in an enclosed shallow-bay. Novel additions to the broader VGW knowledgebase include:

- Detailed analysis results of hydrodynamic measurements at the field site resulting from inbound and outbound deep-draft vessel motions utilizing wavelet transforms;
- An algorithm capable of identifying VGW events across a range of environmental- and vessel-related conditions solely using hydrodynamic data streams
- Correlation between the long-term marine traffic history and corresponding in-situ hydrodynamic data;
- Allocation of the field site's total energy budget into the constituent wave-energy sources including VGW events of ships with inbound and outbound transit headings and fetch-limited wind waves;

The research portion of this project was structured around investigations into links between VGW and corollary hydrodynamics. Vessel parameters considered during analysis range from hull shape and draft size to the recorded transit speed of the vessel at the point of wake generation. Wake hydrodynamics are quantified with statistics such as wave heights or wave periods along with relevant environmental conditions described in weather reports or water depths. The hydrodynamic statistics presented are the product of a wavelet analysis performed on recorded in-situ measurements. Essentially continuous hydrodynamic data collection occurred throughout the 10 months of field deployments spanning November of 2017 through September of 2018.

The overarching field research objective called for assessing the impacts of wind waves and VGW events around a recently constructed beneficial-use, mixed-sediment dike enclosing an incipient beneficial-use marsh. Encouraging dredgers to commit increasing amounts of extracted sediments to beneficial-use endeavors effectively limits the rate of wasteful dumping and

therefore constitutes a favorite precept for the Engineering With Nature (herein EWN) initiative [ERDC, 2019]. The next section further explains the benefits realized from the adherence to EWN principles.

1.2 Motivation

A growing recognition that nature-centric engineering designs enjoy augmented long-term outcomes is steadily galvanizing the proliferation of EWN. By choosing to either work with - or actually employ - naturally occurring processes to attain project objectives, engineers are observing benefits ranging from cost savings due to less original construction and later maintenance efforts to engineered structures exhibiting longer lifespans. Principles both embraced by the EWN community and applicable to this project are tabulated in Table 1.

Table 1 – Aspects of the project related to Engineering With Nature and corresponding beneficial effects.

Feature	Phase	Effects	Impacts
Dredged Material Beneficial Use	Dike construction	Dike composed of mixed sediments dredged from HSC rather than hauling in rip-rap	Reduced rip-rap purchase and transport; reduced transport of dredged sediments to disposal site; increased on-station time of dredge
Dredged Material Beneficial Use	Wetland construction	Previous area low in biological value transformed into highly productive habitat	Habitat for migratory birds; new spawning grounds for bay fish supporting fishing and ecotourism industry; aesthetically pleasing
Avoids Hard-Armoring	Dike construction and erosion	Temporary protection for enclosed tidal marsh before naturally eroding	Incipient vegetation given chance to take root and grow while sheltered; dike erodes after several years, connecting the marsh to the Bay and forming open habitat supporting wildlife

Researchers have remarked on the relative scarcity of long-term, real-world coastal hydrodynamic data for decades, particularly high-fidelity data exhibiting the distinct signatures of VGW phenomena [Herbich & Schiller, 1984; Velegrakis et al., 2006; Garel et al., 2008). Successfully executing data collection thus furnished the first meaningful contribution by addressing longstanding in-situ VGW data deficiencies. The coalescence of the nearly year-long

hydrodynamic measurement campaign into a vast data repository supporting the observations and conclusions of this study may be but the "tip of the iceberg" for the findings to be ultimately derived from this dataset.

Coastal Texas planners and engineers face a looming crisis instigated by the long-term exposure of GB to what we would consider today as substandard dredge material disposal and similar bed-use practices. This unsustainable past creates a future potentially lacking in the subaqueous space needed for local developmental or industrial needs. This issue is not necessarily unique to GB or Texas; any body of water experiencing extensive historical development is likely encountering such problems, especially if dredging operations use local areas as disposal grounds. Usage of these underwater spaces may involve laying new pipelines for the oil and gas industries common to Gulf states, installing new oyster reefs to combat water quality issues and attenuate wave energy while supporting the shellfish industry, or simply providing the open channels required for safe navigation around the waterbody. Embracing beneficial use endeavors for dredge material presents a viable method for aiming to ensure the long-term vitality of coastal environments.

Although beyond the scope of this thesis, the ultimate end-goal is currently envisioned as taking the form of a robust sediment transport model specifically pertinent to closed coastal systems hosting large navigation or shipping channels. The model's inclusion of parameters such as hull design, vessel transit speed, and local bathymetry would yield increasingly high-resolution estimations for sediment transport resulting from theoretical navigation scenarios [Tate et. al, 2008]. Short-term studies such as the high-resolution VGW example would provide researchers and scientists with fresh perspectives on the instantaneous mechanisms modulating vessel wake generation. The converse side to the short-term model is naturally a long-term variant, specifically one operating on multi-month to multi-year scales. Establishing novel linkages between observed hydrodynamics and the responsible marine traffic patterns (localized in both time and space, i.e., site-specific) would directly aid in long-term model formulations. Longevity models will likely attempt to resolve large-scale dynamics (such as those occurring across an entire bay system) into small or local scaled effects such as shoreline erosion, increased water surface fluctuation variabilities, and habitat degradation rates.

1.3 Conceptual Overview

1.3.1 Vessel Wakes

1.3.1.1 General background

Investigations into wake-related topics began with efforts to resolve experimental relationships between scaled models and the original object [Froude, 1874]. From these attempts came the

realization of linkages between vessel shapes, vessel speeds, and "hydrodynamic resistance" (the wave-making tendencies of the fluid [Sorensen, 1973]). When organized in equation form, the concept of hydrodynamic resistance is referred to as the Froude number. The Froude number, a dimensionless ratio between inertial (ratio numerator) and gravitational (ratio denominator) forces, is frequently manipulated into slightly variant forms so as to best address the unique hydrodynamic flow-regime conditions to be investigated. Two basic forms of the Froude number are useful in vessel wake studies: the depth (1a) and vessel length (1b) formulations:

$$Fr_d = \frac{V_s}{(gh)^{0.5}} \tag{1a}$$

$$Fr_l = \frac{V_s}{(gl)^{0.5}} \tag{1b}$$

Wherein V_s is the velocity of the disturbance (i.e., ship), g is the gravitational acceleration, h is the water depth at the point of initial disturbance (i.e., navigation channel), and l is the disturbance length-scale (i.e., vessel hull length). Notably arising from (1a) is the form of the equation known as the depth-limiting Froude number. The equation's depth-limiting version is useful for approximating the threshold depth where orbital fluid motions created by propagating waves fail to interact with the seafloor – thereby providing quantitative justification for whether to employ depth-dependent linear wave theory (herein LWT) simplifications as shown in Fig. 1 [Sorensen, 1997; Torsvik et al., 2006].

Substituting the LWT depth-to-wavelength ratio (h/λ) threshold of no less than 0.5 in the depth Froude number transforms the equation such that along the vessel's sailing line:

$$Fr_h = \frac{V_s}{(gh)^{0.5}} = \frac{(g\lambda/2\pi)^{0.5}}{(gh)^{0.5}} = 0.56 \tag{1c}$$

At first glance, a logical conclusion to the (1c) result appears to be that deep-water assumptions are only viable for $Fr_h \leq 0.56$, however in practice this threshold is actually closer to 0.6 or 0.7 due to shallow water (i.e., refraction or diffraction) considerations [Weggel & Sorensen, 1986; Sorensen 1997]. Hence, deviations of in-situ Froude behavior from the general theory often exist.

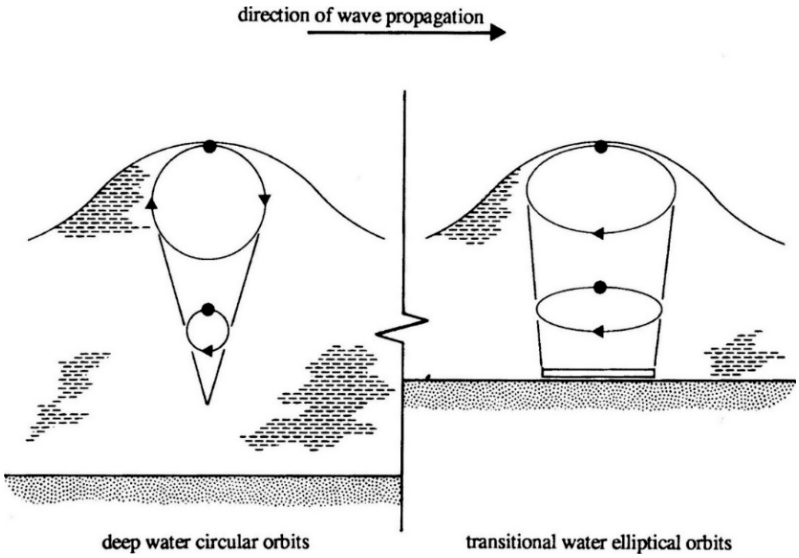

Fig. 1 – Orbital fluid motions induced by wave propagation under deep-water simplifications (left) and either transitional or shallow-conditions (right). Deep-water orbitals attenuate prior to reaching the bottom and thus have negligible bed impacts. Figure adapted from Chadwick (2021).

An additional form of the Froude number that further includes a coefficient summarizing the ship hull form, described as a "modified" Froude number [Kriebel & Seelig, 2005], has also proven useful in VGW analysis (1d):

$$Fr_m = Fr_l * \exp\left(\alpha \frac{d}{h}\right) \tag{1d}$$

$$\alpha = 2.35(1 - C_b) \tag{1e}$$

$$C_b = \frac{\nabla}{lbd} \tag{1f}$$

$$\nabla = \frac{w}{\rho} \tag{1g}$$

Wherein d is the vessel draft, α is the hull-form empirical coefficient, C_b is the block coefficient, ∇ is the vessel displacement, b is the vessel beam, w is the vessel weight (i.e., tonnage), and ρ is the water density. The block coefficient (1f) is commonly used during vessel-related investigations as it aggregates the vessel length, width, draft, and weight into a single, comprehensive value.

Wavefields created by VGW events are complex phenomena easiest understood by decomposing the event into two main components: higher frequency surface waves and lower frequency displacements in the water surface elevation.

1.3.1.2 Surface wave component (Kelvin or Havelock waves)

Thomson, known through his moniker Lord Kelvin, introduced the seminal theory for articulating how surface wave fields introduced by Froude (1877) develop in conjuncture with a transiting vessel [Thomson, 1887]. This framework shed further light on bow-induced divergent and stern-induced transverse VGW surface waves, as well as describing the notion of an empirically definable cusp line. The two surface wave components and the cusp line eventually formed are sketched in Fig. 2. The cusp line is understood to arise along the locations of interaction by the divergent and transverse waves. The delineation of where this cusp line materializes can prove highly valuable during wave-energy investigations; the largest wave heights (i.e., energy transmissions) measured during wake events generally spawn from superimposing waves along these cusps [Sorensen, 1973; Stumbo & Fox, 1998].

Although the Thomson (1887) deep-water wake theory (i.e., Kelvin wavefields) sufficiently described much of the wake generation process, major deficiencies remained, especially when attempting to calculate cusp amplitudes. Inherent “mathematical limitations” in Lord Kelvin’s framework would translate into singularities cropping up during cusp-line amplitude calculations, precluding the maximum wave height calculations critical to engineering design [Sorensen, 1973]. Furthermore, as his methodology assumed constant depth, the VGW theory neglected the effects of water depths essential to wave-generation and propagation processes. Failing to include depth effects would not present an issue assuming only deep-water conditions were considered, however this is certainly not the case as depths grow shallower (Fig. 1).

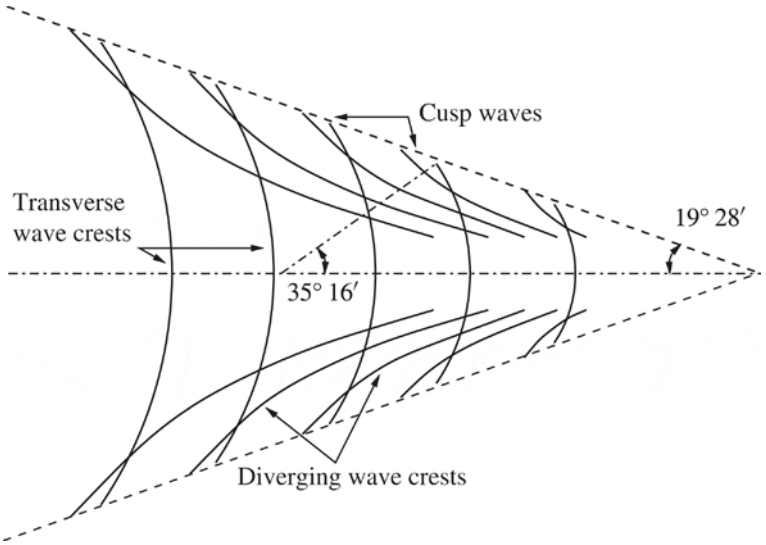

Fig. 2 – Wave-field pattern generated by a vessel moving from left-to-right as described by Lord Kelvin [Thompson, 1887]. The respective oblique and stern-normal propagation directions for diverging and transverse waves are readily seen; the cusp-line interaction of the two wake components formed roughly 19.47° away from the bow is indicated by the dashed lines forming the outer reach of the wake field. Figure adapted from Torsvik et al. (2015).

A solution for the drawbacks of Lord Kelvin's theory came during attempts to resolve the wake generation process while only considering shallow water conditions [Havelock, 1908]. It was found that when generated in successively shallower (i.e., increasing Fr_d) conditions, the VGW response would be to proportionally shift the diverging wave propagation angle forward until a right-angle is formed with the sailing line. The empirical description for the deviation of the divergent wave away from Kelvin's theory is found in (2a-b):

$$\cos^2(\alpha) = \frac{8(1-\beta)}{(3-\beta)^2} \tag{2a}$$

$$\beta = \frac{2kh}{\sinh(2kh)} \tag{2b}$$

Wherein α and k denote the divergent wave propagation angle away from the ship and LWT wavenumber, respectively. The creation of a right-angled diverging wave will only occur at a Fr_d

ratio of unity, signifying the flow regime has jumped from subcritical to critical flow. An additional VGW response can be expected once the diverging bow-waves and sailing line reach orthogonality. Physical limitations (as derived from LWT) that govern propagating waves have determined that while at a depth h, a wave may not have a velocity surpassing the shallow water wave celerity $(g * h)^{0.5}$. This limiting threshold effectively defines the demarcation between trans-critical and critical flow regimes, as is confirmed via the relation in (3):

$$C = C_g = (gh)^{0.5} \qquad \forall\, h \mid Fr_h = 1 \tag{3}$$

Wherein C quantifies wave celerity, C_g the wave group velocity, and the qualifying notation is read as "for all depths such that the depth Froude number equals unity." Such flow regime transitions become especially pertinent during nonlinear vessel wake effect considerations; standing and precursor soliton waves are two of several known nonlinear processes to potentially form along the border separating a fluid body existing in multiple regime states [Torsvik & Soomere, 2008]. The majority of further detail discussing nonlinear VGW phenomena presented in this proposal are found in a later section.

While revising Lord Kelvin's original deep-water VGW surface wave-field theory for the facilitation of shallow-water applications, Havelock also formulated the approximation for VGW wave-amplitude decay rates while in shallow-water conditions (i.e., Havelock wavefields) [Havelock, 1908]. He found that as a transverse VGW component propagates along the sailing line, but in the direction reverse to that of the source vessel, then wave amplitudes will exhibit an inversely proportional decay rate relative to the square-rooted distance that the wave has traveled from stern.

In addition to providing the visible effects of a wake most people are familiar with, Kelvin or Havelock waves are notable due to their direct association with shoreline erosion. These surface waves are the only wake component where waves will physically break, thus transmitting wave energy into the surfzone via the impact. The amount of energy imparted by each wave can be calculated using LWT (4):

$$E = \frac{\rho g H^2}{8}\,\lambda \tag{4}$$

Wherein E defines the average energy transmitted per unit wavelength λ and H defines the wave height.

1.3.1.3 Water surface elevation displacement component (Bernoulli Waves)

Unlike the surface waves that are a result of the interaction between a moving hull and the surrounding water, displacements in water surface elevations stem from a pressure distribution created by the water displaced by a moving vessel. As the vessel travels forward, water is forced into relatively tight streamlines around the hull and a velocity field is formed [Sorensen, 1973; Allenstrom et al., 2003]. This velocity field is naturally coupled with a corresponding pressure field as described by the Bernoulli equation (5):

$$p + \frac{1}{2}\rho V^2 + \rho g h = C \tag{5}$$

Wherein p is the pressure, V is the water velocity, and C is a constant. Increases in velocity field magnitudes are therefore readily understood as proportionally increasing the pressure field magnitudes, resulting in undulating water surface elevations called Bernoulli waves.

The exact nature of the pressure distribution created by a moving vessel were first documented in Todd (1967), who describes the actual water surface profile by decomposing it into several constituent components (Fig. 3). The components are summarized by Sorensen (1973) using three general descriptions:

1) The pressure distribution instigating a hydrostatic response.
2) Wave systems at the bow and stern that begin with a wave peak.
3) Wave systems at the forebody and afterbody that begin with a wave trough

Depending on the conditions (i.e., water depth and basin geometry), Bernoulli waves can exist without any stark visible effects. This is due to the longer-period nature of the water surface elevation undulations, where wave periods are typically 1-2 minutes long and waves propagate without ever breaking along the shoreline. Bernoulli waves have their greatest visibility when the leading trough, known as the drawdown, is particularly strong. Large drawdowns result from confined basin geometries, larger vessels, and faster vessel speeds [Herbich & Schiller Jr., 1984; Allenstrom et al., 2003]. An observer near the shore will notice a steady retreat of the water line followed by a steady resurgence that will either return or temporarily overshoot the waterline relative to the original elevation (Fig. 4).

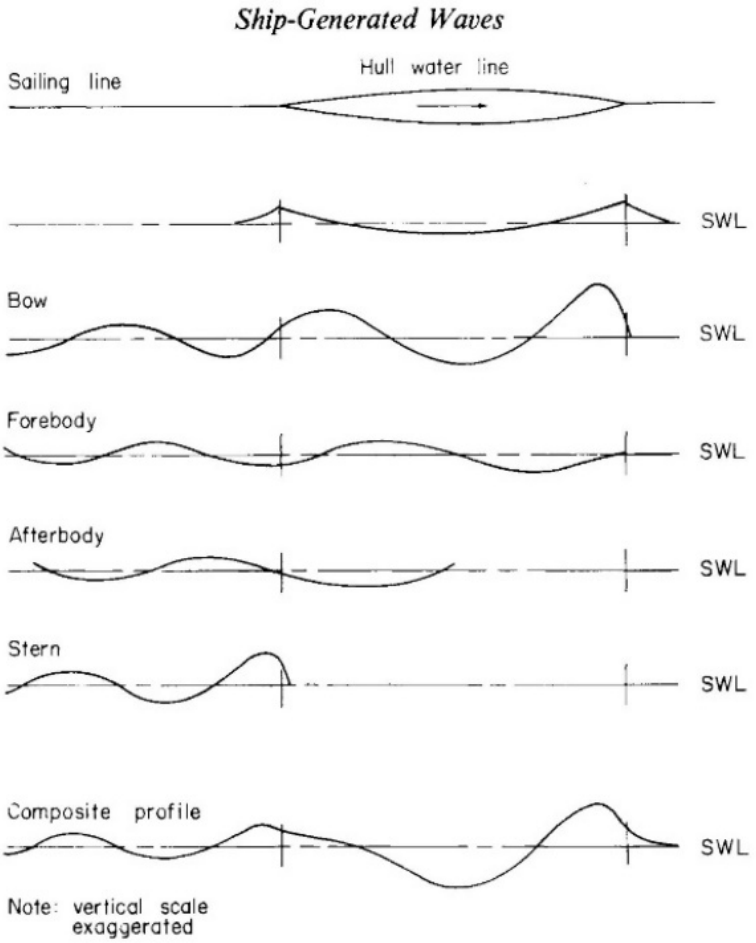

Fig. 3 – Visual representation for the various components of the pressure field created by a transiting vessel. Figure adapted from Sorensen (1973).

Fig. 4 – Before and after a 140.5-second long, 0.55-meter Bernoulli wave drawdown caused by inbound tanker "ALASKA" (seen in the top image). Bottom image taken 5 minutes after the top and illustrates the maximum extent of the drawdown magnitude as well as the arrival of the leading Havelock surface wave marking the onset of the return surge.

1.3.1.4 Parameters modulating wake formation

Prior investigations have concluded that the parameters modulating vessel wake generation, in no particular order, are: vessel hull shape and dimensions (namely length, beam, and draft), vessel displacement, transit velocity and acceleration, sailing line location, water depth, and basin geometry [Kriebel & Seelig, 2005]. Examples of such investigations are:

- Sorensen (1967) – 111 VGW events recorded from about a dozen shallow to medium draft vessels in a narrow, confined waterway. Concluded that wave heights depend more on transit velocity and water depth than vessel displacement or hull geometry.
- Herbich & Schiller Jr. (1984) – Roughly 50 VGW events recorded from vessels with drafts ranging from shallow to deep in a narrow, confined waterway. Concluded deep-draft vessel surges were a function of vessel draft and speed while shallow-draft vessel surface waves mostly a function of transit speed.
- Allenstrom et. al (2003) – Performed several transits of a single scale modeled deep-draft vessel passing the entrance of a confined, square-shaped harbor. Concluded that basin geometry, water depth, and proximity of the sailing line to shoreline banks were the greatest factors in the Bernoulli wave formation.
- Velegrakis et. al (2006) – 2 ferries of similar size, one conventional and one high-speed, with 3 VGW events each were compared in a deep, unconfined waterway. Concluded that the wave heights of the faster ferry were nearly double that of the slower ferry while the faster ferry also created multiple wave packets as opposed to the single packet of the slower ferry.

1.3.2 Wavelet Analysis

As with Fourier transforms (herein FT), wavelets transforms (herein WT) are time-to-frequency domain transformations packaged into two overarching varieties – continuous (CWT) and discrete (DWT) transforms. CWT operate as their name implies, continuously across an infinite range of wavelet-modulating parameters to be discussed shortly. DWT instead consider transforms narrowly defined by a finite set of parameters. Consequently, CWT analyses are typical for when qualitative results are desired (i.e., high-resolution contour plots showing the temporal evolution of a signal across an infinite set of frequencies). When quantitative results are the end-goal (i.e., the temporal evolution of a signal contributed by a specific frequency), a DWT is then the tool of choice. Notably different than the infinitely continuous FT is the temporal localization possible by WT. Signals containing chirps, discontinuities, or otherwise nonstationary evolutions (such as VGW events) are by definition non-continuous and thus technically violate the assumption of a continuously stationary signal fundamental to Fourier-based methodologies. Both versions of the WT technically rely on two governing mathematical constructs, a mostly

analogous initial wavelet function (ψ) and a wavelet size/shape modulating function (ϕ) that assumes slightly different behaviors depending on a continuous or discrete method of operation.

WT introductions begin with motivation and findings of seminal papers from J. Morlet and A. Grossman [Grossman & Morlet, 1984; Grossman et al., 1985; Grossman & Morlet, 1985]. These papers first propose the use of wavelets during a seismic trace analysis via first introducing the pair of fundamental dilation (a) and translation (b) parameters requisite for a CWT, respectively used to manipulate the scale of the wavelet resolution and to translate the wavelet along the time series temporally. Implementing the two manipulations was as simple as combining them with the index of each data point (t) into a single term and substituting the modified index for the original time point (6):

$$t = \frac{t\ -\ b}{a} \tag{6}$$

With the necessary wavelet modulations in place, the base, or "mother," continuous Morlet wavelet function prior to modulation was derived (ψ; 7a), along with the post-modulation version ($\psi_{a,b}$; 7b). The generalized form for a CWT function was then extrapolated from the Morlet wavelet and can be found in (8):

$$\psi(t) = \left(\frac{1}{\pi^{0.25}}\right) * \exp(i * 2\pi * f_0 * t) * \exp\left(\frac{-t^2}{2}\right) \tag{7a}$$

$$\psi\left(\frac{t-b}{a}\right) = \left(\frac{1}{\pi^{0.25}}\right) * \exp\left(i * 2\pi * f_0 * \frac{t-b}{a}\right) * \exp\left(\frac{-1^2}{2} * \frac{t-b}{a}\right) \tag{7b}$$

$$\psi_{a,b}(t) = \left(\frac{1}{\sqrt{a}}\right) * \psi * \left(\frac{t-b}{a}\right) \tag{8}$$

Wherein variables i, f_0, and t, respectively, represent the imaginary unit, central mother wavelet frequency, and arbitrary time point. Mother wavelets define the initial, basic structure of the wavelet function whereby all translated and dilated forms of the wavelet can be traced back to. Verbally, (7a) reads as the wavelet function at time t equates to the (wavelet-dependent) normalization factor multiplied by the mother wavelet and a Gaussian bell curve, each at time t (i.e., the Gaussian bounds the wavelet envelope) [Addison, 2017]. Resulting from the infinitely

shrinking time steps assumed during the transform, the behavior of the shape modulation function ϕ for a CWT simplifies to a continuous vector of all real numbers bounded by the user-defined range of the dilation parameter (a). As will be seen shortly, the DWT equivalent of the scale function ϕ has no such simplification due to discretization of the constituent signal frequencies.

The Morlet wavelet is classified as an analytic function due to the complex nature of the sinusoidal term allowing for a selective analysis able to limit frequency considerations to sets of only positive components [Kaiser, 1994]. The choice between a real- or complex-valued function centers around the goal of the analysis; real-valued wavelets are useful for signals exhibiting sudden discontinuities while complex-valued wavelets specialize in relaying the phase and amplitude information for signals of a more steady, oscillatory nature [Farge, 1992]. Unlike their real-valued counterparts, complex functions such as the Morlet wavelet are often employed to examine both phase and amplitude information.

Figure 5 displays the complex Morlet wavelet in terms of the real (i.e., signal amplitude; black line) and imaginary (i.e., signal phase; red line) components for a mother wavelet (panel A) varying in frequency (B1), dilation (B2), or scale (C1-2). The energy spectrum of the wavelet in panel A is also plotted in panel D, resembling the Fourier spectrum but with relatively lower frequency resolution. The derivation of the wavelet energy spectrum (panel D) is given by (9):

$$\left|\hat{\psi}(f)\right|^2 = (2\pi^{0.5}) * \exp(-(2\pi * f - 2\pi * f_0)^2) \tag{9}$$

Wavelet spectra resulting from (9) similarly adheres to the statistical relationship described in Percival's Theorem (also mandatory to Fourier spectra) in that the variance of a signal process is equal to the integrated spectrum [Percival, 1995].

The loss in frequency resolution is a direct impact of temporal localizations. The time and frequency domain resolutions are governed by an implication of Heisenberg's Uncertainty Principle, effectively meaning that any change to the resolution of one must be offset by an equal and opposite change to the other. The imaginary component is observed maintaining a one-quarter forward phase-shift relative to the real, behavior attributed to the normalization factor term forcing unit energy in the wavelet (7a) [Addison, 2017].

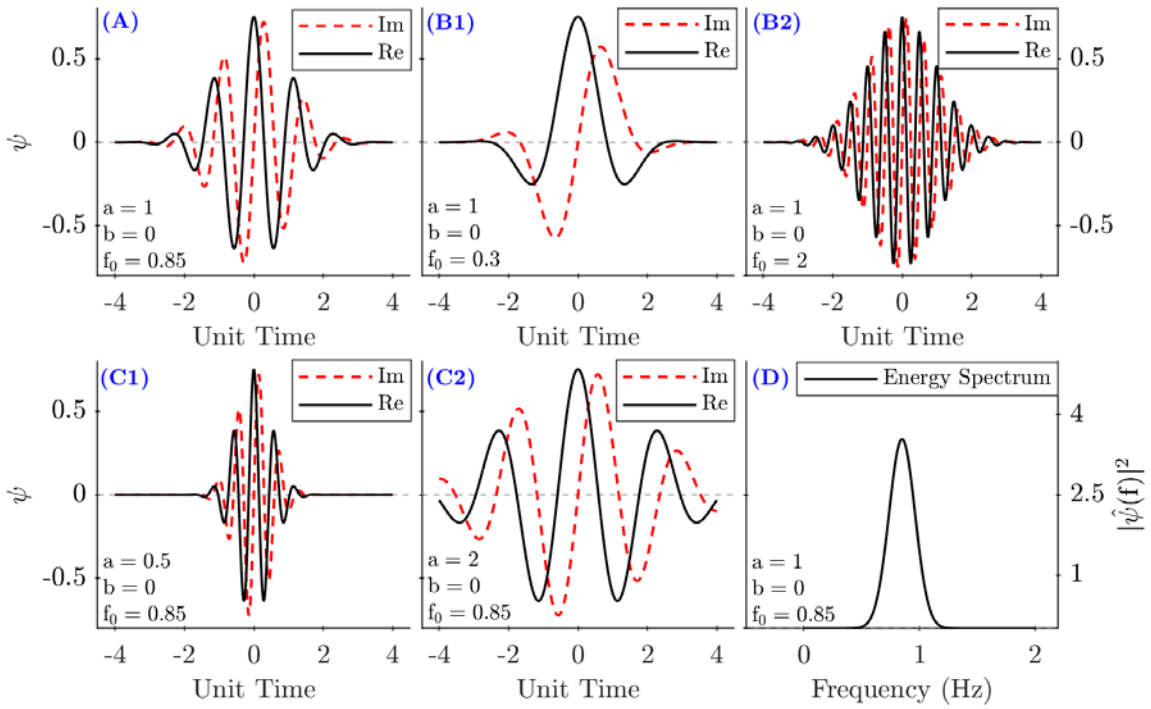

Fig. 5 – The complex Morlet wavelet (ψ) partitioned into phase (i.e., imaginary) components in red and amplitude (i.e., real) components in black. The unmanipulated mother wavelet at a frequency of 0.85 is plotted in panel A; changes in wavelet frequency with dilation and translation each held constant are found in B1-2; changes in dilation with frequency and translation constant are shown in C1-2; the wavelet energy spectrum ($|\hat{\psi}(f)|2$) of the mother wavelet A is shown in D. Axis values for panels A, B1-2, and C1-2 are identical while the panel D axis values are found to the bottom and right. Figure modified from a similar figure in Addison (2017).

Further illustration of the fundamental WT operations is given in Fig. 6. In the figure, an arbitrary signal (i.e., the water surface elevation for a fixed location) propagating through time is overlaid with an analyzing wavelet function, in this case the Mexican hat wavelet. The upper panel (a) visually relates how the WT calculates quantitative values using translations and dilations; as the magnitude in wavelet translation increases the wavelet "slides" across the abscissa, while changes to the wavelet dilation magnitude control how the wavelet scales in size relative to the unaltered signal. Instances of strong positive or negative agreement between the wavelet and signal produce large values in the transformed wavelet coefficients, while strong disagreement then output large negative values.

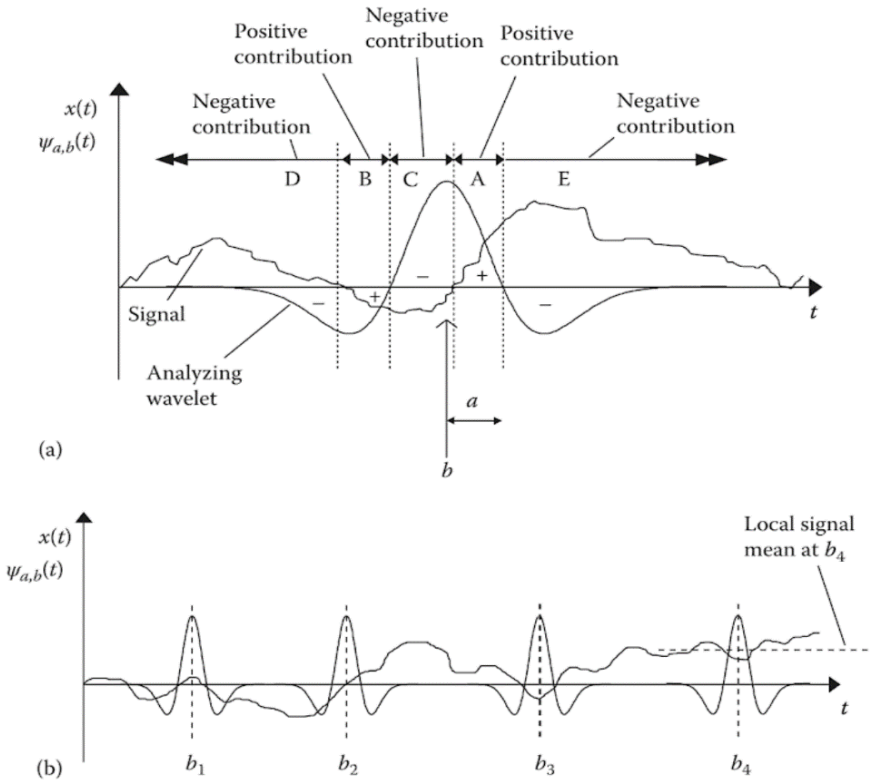

Fig. 6 – The Mexican hat wavelet undergoing transformations during signal analysis; positive and negative contribution explanations highlighted in the top panel (A) are shown during four distinct time point translations yielding strong positive (b_1), weak positive or negative (b_2), and strong negative (b_3-b_4) values. Figure adapted from Addison (2017).

The lower panel (b) focuses on the translation of the wavelet at a fixed dilation at four separate points in time (b_1-b_4). The wavelet has strong agreement with the signal at b_1, and thus a large positive value results from the WT. A rough split of the wavelet by the signal during a zero-upcrossing event at point b_2 yields a relatively small value after the split in agreement effectively cancels out for much of the wavelet. Disagreement between the wavelet and signal signs at all locations in b_3 coinciding with the mirrored concavity produces a large negative WT result. Lastly, another source of large negative values is given at b_4 due to sign disagreement at the wavelet edges and concavity disagreements at the wavelet maximum. The "continuous" in "continuous wavelet transform" is justified at this step in the analysis – the lower panel in Fig. 6 has just a single scale dilation with only 4 translations and would therefore yield just 4 datapoints; a CWT in theory yields an infinite number of dilations along an infinite number of translations.

Further advancements for wavelet analysis took place with the advent of wavelet "frames" following the linkage of wavelet functions to preexisting linear algebra mapping constructs known as subspaces [Daubechies et al., 1986]. Essentially, when the components forming a signal are disaggregated (i.e., projected) into their relative contributions, the resulting components exist in the subspace created during the projection. The incredible mathematical power inherent to these subspaces rapidly facilitated new wavelet applications as researchers realized the benefits of a narrowly defined set of orthonormal subspaces known as Hilbert space (Hʊ) were now relevant to WT analyses. Although mostly beyond the scope of this proposal, an articulation of the Hilbert space criteria is given in (10) as the orthonormality of Hʊ with respect to wavelets substantiates a key DWT technique central to this proposal.

$$\text{Hʊ} \equiv \{ f: \mathbb{R} \rightarrow \mathbf{C}: f \text{ is measureable and } \| f \|^2 \equiv \int_{-\infty}^{\infty} dt \, |f(t)|^2 < \infty \} \tag{10}$$

Which is read as when a set of numbers with individual points (t) potentially spanning all read numbers ($\mathbb{R}$), Hilbert subspaces (Hʊ; i.e., orthonormal spaces) will:

- equate to functions (*f*) having a viable complex number (**C**) for each point (*f*(t))
- be measurable (i.e., finite)
- Have a squared inner-product (i.e., squared norm) ($||f||^2$) equal to the integration of the sampling increment (*dt*) multiplied by the absolute value of the sample magnitude of each point squared ($|f(t)|^2$) over all real numbers.

A set of values forming a coherent signal (i.e., water surface elevation timeseries) meeting the criteria required by Hilbert spaces (10) by definition has orthonormality [Daubechies, 1988]. In layman's terms, signals or data series meeting the requisite criterion above are effectively guaranteed to be decomposable into an arbitrary number of scaled subsets; these subsets represent the proportional contribution by the local forcing processes operating at the given scale of the overall signal at any given point in time. This translates to the water surface elevation measurements recorded by coastal researchers having the ability to be broken up into various ranges, or bins, that contain the energy imparted on the water surface by waves propagating at a period within the bounds of the particular bin.

Consequentially, these orthonormal bases would unlock the necessary proofs required for showing DWT could be performed with high fidelity signal decompositions. The basic wavelet function for a discrete wavelet is similar to that of a continuous wavelet, and is given in (11a):

$$\psi_{m,n}(t) = \left(\frac{1}{\sqrt{a_0^m}}\right) * \Psi * \left(\frac{t - n b_0 a_0^m}{a_0^m}\right) \tag{11a}$$

Wherein *m* and n are both integers respectively controlling the dilation and translations, a0 is a discretized dilation step (i.e., scale factor), and b0 is the discretized spatial coordinate. Common protocols for selecting discretized values for a0 and b0 stem from the power of 2 composition of the DWT frequency subbands, whereby respective values of 2 and 1 are chosen to preserve logarithmic relationships. The updated form of the DWT general equation using a0 and b0 parameter values of 2 and 1 is provided in (11b):

$$\psi_{m,n}(t) = \left(2^{-m/2}\right) * \psi * ([2^{-m} * t] - n) \tag{11b}$$

As was mentioned in the WT introduction, the scaling function (ϕ) of a DWT is not simplified to unity as is possible with the CWT scaling function. Instead, the scaling function ($\phi(t)$) is presented as a summation of all scaling equations derived during dilation and translation modulations of the original $\phi(t)$ (12):

$$\phi(t) = \sum_{k} c_k * \phi(2t - k) \tag{12}$$

Wherein "contracted versions" of the scaling function ($\phi(t)$) defines the $\phi(2t - k)$ term. These contracted versions have undergone translation manipulations at the interval step (k) according to the relative scaling coefficient (c_k). Addison (2017) notes that the implications from (12) confirm unique scaling functions at a certain scale can be derived from one or more scaling equations at the previous scale. This concept of a finite number of scaling equations (ϕ) superimposing to form the scaling function ($\phi(t)$) was first discovered by I. Daubechies in what she coined "compactly supported wavelets" [Daubechies, 1988].

Partitioning a non-stationary data series into orthonormal subsets was first accomplished shortly after I. Daubechies derived the first orthonormal wavelet functions and came in the form of the multiresolution analysis (herein MRA) [Mallat, 1989a; Mallat, 1989b; Meyer, 1989]. Derivations of the MRA algorithm employed to split the initial data series, a process referred to as "additive decomposition," were first formed during an image processing application known as digital compression.

In the MRA, S. Mallat was able to prove that by setting bounded frequency filters increasing by sequential powers of 2 (i.e., octaves, or bins with either twice or half the frequency of adjacent bins), variations in the overall signal resulting from a specific octave (D_j) could be discerned and separated from the octave one scale coarser in resolution (A_{2i+1}). The algorithm used for additive decomposition is given in Fig. 7.

Considering both high-pass ($\tilde{G}$) and low-pass ($\tilde{H}$) filters are used to bound the frequency bins, each iteration of the algorithm effectively establishes a band-pass filter doubling in bin frequency range size (Fig. 7). When the filters combining to form the band-pass are also "mirrors" of each other (i.e., in the sense that they are each half an octave away from the mean of the corresponding frequency bin), they are known as quadrature mirror filters [Mallat, 1989a]. Starting with the last (i.e., lowest resolution) frequency bin, the full signal ($f(t)$) undergoes the first decomposition beginning with the highest possible frequency; in most cases this frequency is determined by the sampling rate of the data.

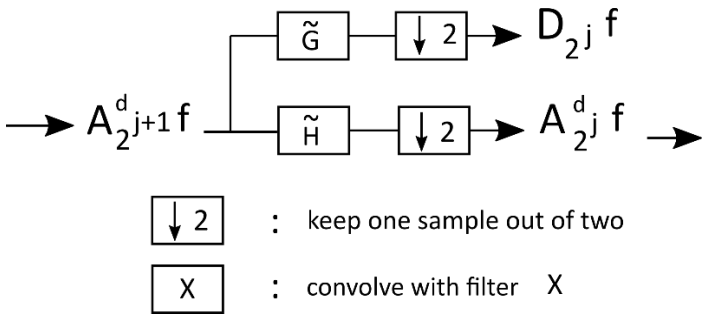

Fig. 7 – One iteration of additive decomposition from the algorithm used to synthesize the multiresolution analysis technique. An approximation of the variability in the original signal (A_j) attributable to forces existing in the frequency detail bin D_j is the result of a high-pass filter ($\tilde{G}$) convolved with the approximation for the signal function calculated in the previous bin (A_{j+1}). The filtered data then tosses every other point, leaving half the total number of points relative to the previous bin. Figure adapted from Mallat (1989a).

Data sampling rates that are powers of 2 allow for considerably simpler operations due to the quadrature nature of the bounding filters working more efficiently around octave expansions. In practice, this implies the highest viable frequency (i.e., the low-pass filter for the first detail bin) possible is given in (13-14):

$$\tau_j = 2^{j-1} , \qquad j = 0, \dots, J \tag{13}$$

$$f_{max} = \tau_j * \Delta t , \qquad j = 0, \dots, J \tag{14}$$

Wherein J defines the total number of frequency subbands, known as levels, to be calculated from the original signal ($f(t)$), j defines the index of the current iteration of the algorithm, τ_j scales the length of the j^{th} detail subband (i.e., number of data points), and Δt represents the sampling rate of the original data. Therefore, if an MRA of level 9 is performed for data collected by a 2 Hz sampling regime, the highest possible frequency in the first detail subband would be 2^{1-1}*0.5 or 0.5 seconds (i.e., the sampling frequency) while the lowest possible frequency in the final detail subband (i.e., level J) would be 2^{9-1}*0.5*2 or 256 seconds (doubled due to the low-pass filter doubling the high-pass). From there, the frequency thresholds sequentially increase by 2^j*0.5 seconds, giving the first three bands as between 0.5 through 1 second, 1 through 2 second, and 2 through 4 second periods, respectively.

Referring back to the algorithm (Fig. 7) and coming full circle, each iteration j receives the resulting signal from the previous $(j+1)$ detail band and determines a maximum allowed frequency (low-pass threshold) that is twice that of the previous band due to the length scale parameter increasing as an octave (14). In setting this maximum frequency, the algorithm removes any signal variations of the original signal due to lower order subbands (i.e., $j-1$, $j-2$, $j-3$, …, $J-(J-1)$), thereby ensuring the only information remaining is per force corresponding to the current bandpass frequency range. This remaining data forms the orthonormal subset defined by (9) for all but the highest subband; the highest subband J first requires the second half of the quadrature mirror, namely the high-pass filter that sets the lowest allowable frequency for the current subband.

As the first iteration (i.e., subband J) enacts its high-pass filter, all information failing due to association with an undesirably low frequency is collected and stored in a $(J^{th}+1)$ dataset. For data series that did not undergo mean-value removal prior to the MRA (i.e., such that the inputted signal does not fluctuate around zero), any non-zero mean information is similarly dumped into this $J^{th}+1$ subband. Therefore, the $J^{th}+1$ subband basically acts as a catch-all for any signal variation information not included in the MRA. For a mean-extracted data series with a properly determined level size, this $J^{th}+1$ subband should be negligible; without a background mean value and any signal variation worth considering existing somewhere between the first and last subbands, there is no forgotten or leftover variation left to be collected.

All of the data failing the current low-pass threshold (i.e., insinuating relevance to a lower subband level) is aggregated into the leftover signal approximation dataset and passed along to the next subband iteration (i.e., to $j-1$). Now that both the high and low pass filters have activated, only level j data remains, representing the projection of the original signal ($f(t)$) onto the subspace of the j^{th} level as discussed with (14). The algorithm then repeats, until the final subband (i.e., the first level) is all that remains.

As was mentioned, the MRA was initially created for image processing, yet due to the orthonormal nature of the MRA bases or frequency subbands numerous applications are possible. Additional examples of early MRA implementations for signal processing topics include

Percival & Mofjeld (1997) for ocean waves and Kumar & Foufoula-Georgiou (1997) for rainfall intensity.

A significant caveat for setting up an MRA involves the selection of the wavelet; three applicable wavelet functions (ψ; panels A2-C2) with their appropriate scaling function (ϕ; panels A1-C1) are plotted for comparison in Fig. 8. Each of the three wavelet types (i.e., Daubechies Least Asymmetric (db4), Symlet (sym5), and Coifman (coif3) are energy preserving orthogonal wavelets with multiple forms identified by the numeric ending to the wavelet abbreviation. The numeric endings correspond to the number of vanishing moments the functions possess [MathWorks, 2019]. Of the myriad of potential orthogonal wavelets, these three were foremost chosen in recognition of their physical shape resembling that of a VGW event; wavelets better simulating the original signal ($f(t)$) will yield better MRA results as compared to those of greater variation (Fig. 6). Additional rationale includes the "db" wavelet sets concentrating their energy near the start of the support (i.e., the peak of the scaling function), "sym" wavelet sets having a nearly linear phase, and "coif" wavelet sets consisting of scaling functions ($\phi(t)$) nearly identical to the wavelet function ($\psi(t)$).

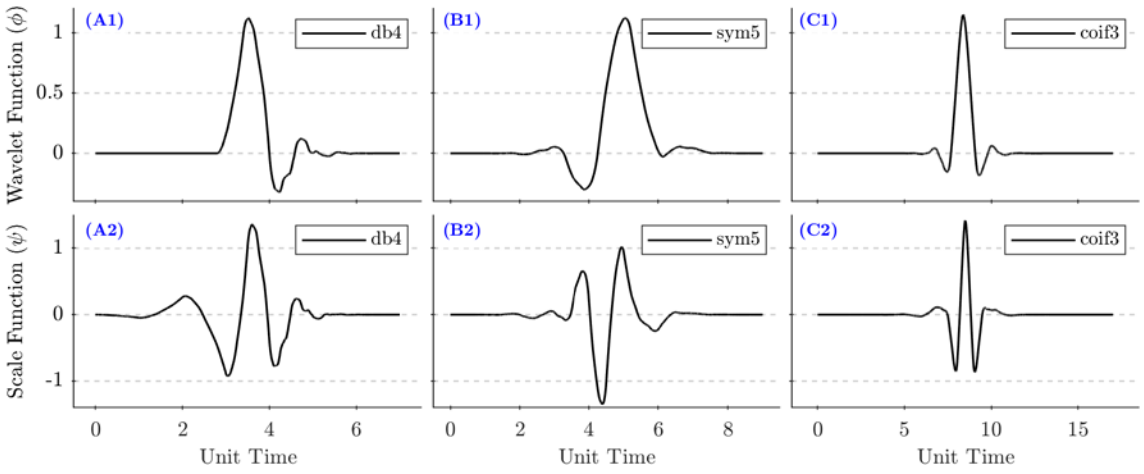

Fig. 8 – Three wavelet functions (ψ) (bottom three panels) along with their corresponding scaling functions (Φ) (top three panels) that were examined as potential wavelets for the multiresolution analysis performed in this proposal. During the discrete wavelet transform, the convolution of the wavelet function (ψ) and the data signal (f(t)) is scaled via multiplication of the scaling function (Φ).

The first interpretations of wavelet coefficients as comparable to Fourier coefficients came from the last major paper discussing wavelet transform bases before the final version of the bases were presented [Meyer, 1989]. Soon after Y. Meyer, Gamage & Hagelberg investigated the applicability of Parseval's theorem of signal variance in relation to the signal spectrum. They show that the power spectrum resulting from a local wavelet transform in fact constitutes a vertical slice of the entire global spectrum [Gamage & Hagelberg, 1990]. In a follow-up paper employing wavelets for the detection of microfront-related weather phenomena, the fact that an "ideal" choice of scaling and basis set for a wavelet exists and further can be deduced from a new method known as a covariance transform is presented [Gamage & Hagelberg, 1993]. Additional details on the findings include the discovery that the main discrepancy between Fourier and wavelet transforms reside in how the basis function are supported; wavelet coefficients are impacted by local events as Fourier coefficients exhibit behaviors pervading the entire domain [Gamage & Hagelberg 1993; Farge, 1992; Kaiser, 1994].

Coincident to these explorations of Fourier and wavelet comparisons were the first investigations into the exact use of variance in wavelet transform analysis [Percival & Guttorp, 1994; Qiu & Meng, 1995; Percival, 1995; Percival & Mofjeld, 1997]. Percival (1995) defines decompositions of variance as a "measure of how much a weighted average of bandwidth of the process changes from one time period of bandwidth-length to the next." In the same paper he further shows that the "global" or complete spectrum is in fact an unbiased and consistent estimate of the true signal spectrum.

2.0 Research Questions

Two investigative research questions (RQ) were formulated to help structure the fieldwork providing in-situ data measurements as well as the complementary analysis that followed.

RQ1 Are there any vessel related parameters (a1-a4) that can be shown to correlate with the wake characteristics (A1-A3) measured at the research site? Parameters to be investigated for such long-term correlations with VGW events include:

a1) Vessel length and draft
a2) Hull-geometry ratios (i.e., block coefficient)
a3) Direction of vessel transit
a4) Variants of the Froude number

While wake characteristics quantified through collected data include:

A1) Measured wave height (historically the most prevalent indicator)
A2) Change in water surface elevation during drawdown

A3) Time duration separating the beginning of a drawdown and the wake arrival

RQ2 What are the relative contributions of each wave-generating condition (b1-b3) to the total wave energy levels at the study site? Conditions applicable to the field site are assigned to one of the following groups:

b1) Wind generated waves
b2) VGW from inbound vessels
b3) VGW from outbound vessels

3.0 Field Site

3.1 General Information

3.1.1 Geography

Data measurements originated from twin elevated platforms installed in Galveston Bay, Texas, (herein GB) known as "Simon" and "Garfunkel" (Fig. 9). The platforms are roughly 2.5 m square, stand 400 m apart, and are both around 100 m away from the adjacent dredge island shoreline. Simon afforded the closest proximity to the HSC, located just under 1.2 km eastward. A team comprised of USACE and ERDC engineers led platform design and construction in late November of 2017. Initial timelines expected dike construction would soon follow, however the active 2017 hurricane season forced 6 months of delays as dredge assets were needed for high-priority maintenance. ERDC researchers lent additional field support with periodic, as-needed platform upgrades and maintenance during the data collection phase.

GB is notoriously shallow with average and maximum undredged depths of approximately 2 m and 3 m, respectively. Such shallows depths are even more unexpected when kept in the context that GB forms the 7th largest estuarine system in the United States. Depths immediately around the project site tend to be even shallower, in part due to the raised seabed resulting from the initial dredging required to build the mixed sediment dike. The area surrounding the site, and therefore the material dredged from HSC nearby, is predominately cohesive sediment (i.e., roughly 40% clay, 40% silt, and 20% sand).

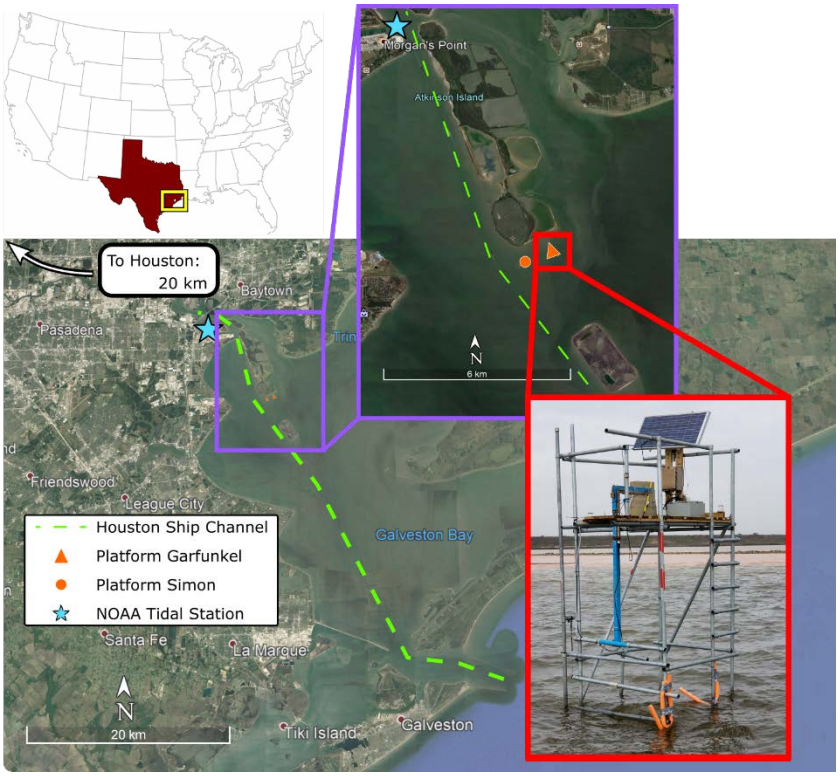

Fig. 9 – Site location in Galveston Bay, Texas.

3.1.2 Vessel Traffic

The HSC remains one of the most heavily-trafficked ship lanes in America; the greater Houston port complex reported handling 260 million short tons of seaborne product in 2017, the most total tonnage of any port second only to the Port of South Louisiana [Port of Houston, 2018]. Port statistics show two liquid bulk carriers (herein tanker vessel) are expected to traverse HSC for every dry bulk carrier (herein cargo vessel). A preponderance of liquid carriers is reasonable due to nearly half the nation's oil extraction job salaries are collected by Houston-based professionals [Gilmer, 2018].

3.1.3 Meteorological

As the field site is located in the middle of a relatively large bay system (Fig. 9), wind- and storm-driven events constitute a non-negligible influence on the local hydrodynamics. Frontal systems impinging the site are typically either maritime tropical (herein mT), maritime polar (herein mP), or continental polar (herein cP) [Henry, 1979; Schroeder & Buck, 1970]. A fourth frontal type known as continental arctic also are possible. These are, however, combined into the cP category for simplicity. Arctic fronts seldom penetrate as far south as GB, and when they do the effects are similar to the effects of the cP except with colder temperatures. Table 2 briefly summarizes the relevant details from each frontal type.

Table 2 – Notable details for each of the primary frontal types that have the potential to impact the field site. Abbreviations include maritime tropical (mT), maritime polar (mP), and continental polar (cP). Orientation describes the typical angle of the boundary line from due North measured clockwise (i.e., 0° is a vertical boundary running north-south). Note frontal event arrivals are not limited to the listed primary season.

Front	Type	Boundary Orientation	Primary Season	Description	Miscellaneous Notes
mT	Warm	-	Summer	Warm, moist, unstable	Only front originating south of Galveston Bay
mP	Cold	40-50°	Spring	Cool, moist, unstable	Front most likely to reverse course and become warm front in winter
cP	Cold	90°	Summer	Cool, dry, stable	Front most likely to reverse course and become warm front in summer
cP	Cold	60-65°	Winter	Cold, dry, stable	-

Galveston Bay generally experiences the majority of fronts under winter conditions and the fewest during summer. The exact number and composition of frontal systems during any given year is a function of several climactic processes, most notably the modulation of the atmospheric jet stream [Henry, 1979]. Another potentially significant process is the long-term pattern of the El Nino-Southern Oscillation (herein ENSO). During ENSO, phases of warming (i.e., El Nino) and

cooling (i.e., La Nina) of the Pacific Ocean alter tropical air masses and, by extension, weather patterns around the world [NOAA, 2021a]. As a transition from weak La Nina to weak El Nino occurred during mid-2018 [NOAA, 2021b], impacts from ENSO on the site hydrodynamics were assumed negligible.

In addition to frontal systems, the other notable atmospheric contributors to the local weather patterns of the project site are known as the sea/bay breeze effects. Unlike the longer-term jet stream and ENSO patterns, sea/bay breeze effects are relatively short term as the timescale is linked to Earth's daily rotation. These coastal breezes are the result of stark temperature gradients forming along shorelines that then trigger a cycle of onshore-offshore airflow. This airflow is able to penetrate tens or even hundreds of kilometers inland along the Gulf Coast [Kocen, 2013]. The formation of temperature gradients stem from water having a specific heat roughly five times that of dry soil [Engineering Toolbox, 2003]. As the sun rises in the morning and begins heating the surface, the landward side of the coastline warms quicker than the seaward side, translating into the air column above the land heating faster than the air column above the water. Since air density is inversely proportional to the temperature, landward air rises at a rate exceeding that of the seaward air. The rising, less-dense landward air mass effectively creates a zone of lower pressure, prompting the denser seaward air mass to migrate inland in the form of a sea/bay breeze. At night the process will reverse into a land breeze, as now the land rapidly cools relative to the gradual heat loss of the water.

3.1.4 Tidal Hydrodynamics

GB is classified as having a diurnal tidal schedule due to its positioning along the Gulf of Mexico. The relatively confined Gulf effectively limits the tidal action to just a single daily cycle, translating to GB typically receiving only 1 high and low tide pairing each day. In actuality, there is an additional intermittent cycle of tidal constituent phase lag that operates on timescales lasting for weeks rather than a day [NOAA, 1989; Rayson et al., 2015]. The effect of this slightly longer-term process leads to only 2-3 weeks of any given month exhibiting the diurnal regime. The remaining 1-2 weeks are temporarily transformed into a mixed semidiurnal regime, often resulting in a reduced tidal range concurrent to the development of the second high and low tide pairing. Figure 10 provides an example of the two regimes alternating as the governing influence in GB over a 3-week period.

The timeseries in Fig. 10 begins as a standard diurnal tide that oscillates at a tidal range of 0.3 m for approximately a week. The single high tide peak begins the process of forming a secondary peak on March 16th, gradually culminating into the 2 distinct high tides of a mixed semi-diurnal regime 3 days later on March 19th. What was previously a 0.3 m tidal range is now observed as having lost over half of its initial magnitude, marking the start of the retransformation back into the diurnal regime. The mixed semidiurnal tide does not fully shed its second peak until March

22nd, a full 6 days after the secondary peak began showing. The diurnal tide is back to a 0.3 m tidal range within a couple of days, eventually reaching a maximum range of 0.4 m on March 25th.

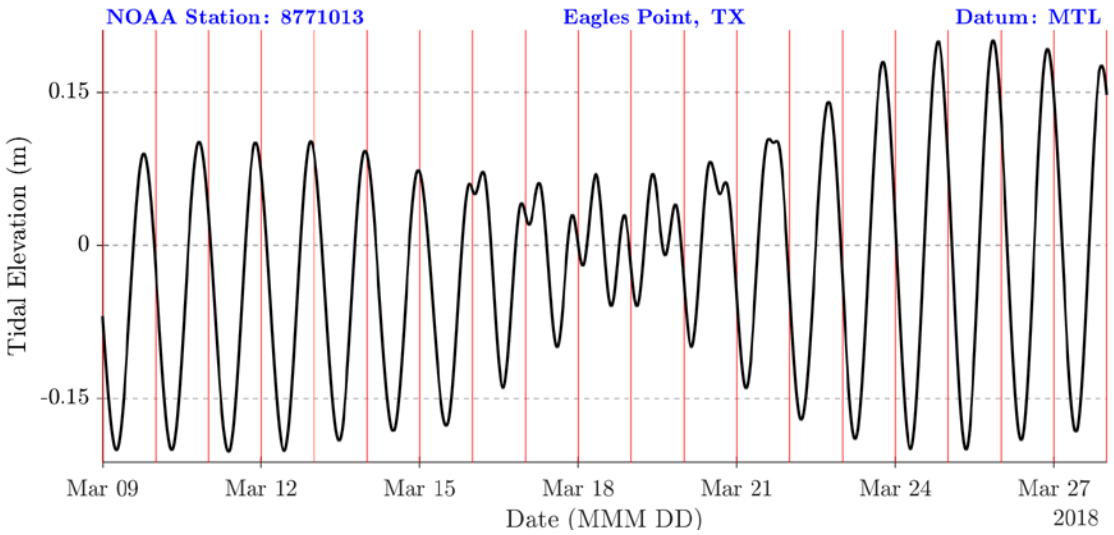

Fig. 10 – Tidal elevation time series from March 09th-28th, 2018 as recorded by NOAA Station #8771013 located in Eagles Point, TX. Datum set to mean tide level (i.e., the arithmetic mean of mean high water and mean low water). The selected date range exhibits both of the potential tidal regime variations in Galveston Bay; a mixed semidiurnal tide is observed from March 16th-21st while the more typical diurnal tide is present across the remaining days. Vertical red lines indicate the start of a new day.

A key effect of the bay's relatively large surface area is the variability in phase lag of the tidal constituents depending on what section of the bay is under consideration. Rayson et. al (2015) were able to estimate the tidal phase lag between the entrance channel and the northern sections near Trinity Bay/Morgan's Point at around 5 or 6 hours. Their results further indicated the greatest phase lag shifts occur in the lower reaches of the bay, likely between the main inlet and Eagle Point, or just south of this project's site platforms. A second notable discovery stemming from the harmonic analysis involved how the main semidiurnal tidal constituent (i.e., M_2) evolved while propagating into GB. The amplitude of the M_2 constituent was found to dampen by about 75% between the inlet entrance and Eagle Point, however it immediately rebounded - nearly doubling in amplitude as it traveled between Eagle Point and Morgan's Point (i.e., while passing directly next to this project's field site). As the M_2 constituent experienced

amplification and phase lagging simultaneously, it was theorized that tidal reflections at the back of GB were in fact spawning standing waves along the nearby shorelines. Due to these standing waves existing relatively near the project site and the presence of the aforementioned phase lag throughout the bay, comparisons between tidal elevations and the long-term free surface elevation recorded at the platforms should keep these tidal phenomena under consideration.

3.2 Instrumentation

3.2.1 Platform Configuration

Figure 11 provides a labeled schematic of an installed platform that notes the location for each sensor or piece of equipment. Brief notes on the instruments such as brand, basic functionality, and measurement sampling regimes are given in Table 3.

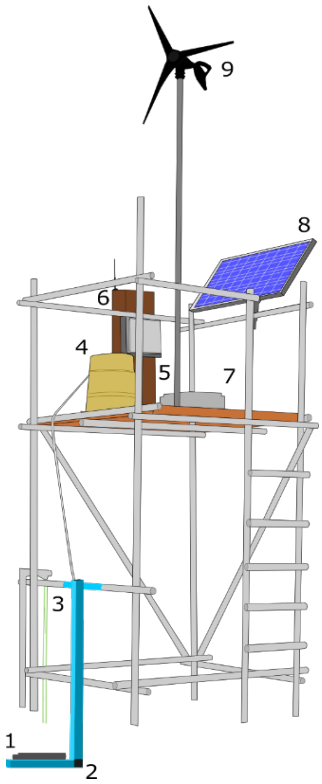

Fig. 11 – General platform schematic; equipment descriptions in Table 3

Table 3 – Instrumentation inventory along with other pertinent details corresponding to the platform found in *Fig. 11*

#	*Sensor*	*Brand*	*Function*	*Sample Rate*
1	Acoustic Doppler Current Profiler	Nortek	Current velocity and pressure	17 min burst @ 2 Hz
2	Hydroacoustic Altimeter	EchoLogger	Depth to bed	Continuous @ 1 Hz
3	Wave Gage	Akamina	Water surface elevation	Continuous @ 8 Hz
4	Water Sampler	ISCO	Suspended sed. concentration	One sample per day
5	Computer Server	-	Upload data to web	-
6	Camera	MOBOTIX	Photograph vessel transits	One picture per 5 min
7	Battery Well	-	Power storage	-
8	Solar Panel	BP	Poly-crystalline	-
9	Wind Turbine	Nature Power	Blade diameter of 116.8 cm	400 Watt

3.2.2 Acoustic Doppler Current Profiler Operation

Capable of recording both sea-surface elevation and current velocity timeseries, the primary instrument supporting hydrodynamic analysis was the Acoustic Doppler Current Profiler (herein ADCP) manufactured by Nortek. Sea-surface elevations and current velocities were measured via a pressure transducer housed in the sensor head (Fig. 12) and via the 3 transducers on the sensor face (Fig. 13), respectively.

The ADCP has two main modes of operation for current measurements, both of which are detailed in Table 4 [Nortek, 2008a; Nortek, 2008b]. Each operation mode transmits acoustic wave beams through the axial transducers and then monitors frequency changes in the acoustic waves reflected back. The reflections result from the acoustic waves rebounding off moving particles or bubbles entrained in the current. These frequency changes are known as the Doppler effect. By assuming the particles travel at the same speed and direction of the surrounding water, current velocity information is then indirectly calculated.

The sampling frequency of pressure measurements mirrors that of the active current measurement sampling regime (Table 4). This means that for each sampling cycle the current profile mode will create a single pressure record, while the wave burst mode creates an entire pressure timeseries.

Table 4 – Description of Nortek ADCP operation modes for measuring current velocity directions and magnitudes.

Mode	*Spatial Function*	*Doppler Method*	*Measurements per Cycle*
Current Profile	Samples multiple vertically stacked cells; creates a water column “profile”	Monitor change in frequency of a single reflected acoustic pulse	A single magnitude and direction for all cells
Wave Burst	Samples a single cell; creates a high-resolution record for a point in the column	Monitor phase shift between successive acoustic pulse reflections	A timeseries of magnitudes and directions for the cell

Fig. 12 – Photograph of the ADCP pressure transducer (round black section)

Fig. 13 – Photograph of the 3 ADCP velocity transducers

Despite the additional spatial information provided by the vertical cell array of current profile mode, analysis only considers data from wave burst mode. Current profile mode allows a maximum sampling frequency of 1 Hz if wave burst mode is kept inactive, while wave burst mode can double this sample rate with a max frequency of 2 Hz. Each collection cycle of wave burst mode data (herein burst) lasted a maximum of 17 minutes at 2 Hz, resulting in a total burst length of 2048 datapoint. The ADCP can also only measure data in one mode at any given time, effectively extending the sampling frequency of current profile mode to one measurement per 20 minutes when using wave burst mode. As the high frequency component of VGW events typically contain waves with 1-second periods, the 2 Hz sampling frequency of wave burst mode constituted the minimum frequency necessary to resolve these short period waves. This minimum sampling frequency threshold is known as the Nyquist frequency (15):

$$f_{Nyq} = f_{max} * 2 \quad (15)$$

Wherein f_{Nyq} is the Nyquist frequency and f_{max} is the maximum resolvable wave frequency in the collected data.

Figures 14-15 illustrate the operation of an ADCP in wave burst mode above and below surface level; Fig. 14 is an image of a deployed ADCP at platform Simon while Fig. 15 is a schematic detailing the process of current sampling. The blue beam seen in the highlighted portion of Fig. 14 is the subaerial section of the blue "L" shaped beam anchoring the ADCP in Fig. 15. The orange box in Fig. 15 defines the cell volume where wave burst sampling occurs, roughly a 0.5 m wide cube centered about 0.5 m above the seafloor that starts 0.1 m away from the sensor (i.e., a 0.1 m blanking distance). The middle of the box was anywhere from 0.3-1.7 m below still water level, however given the relatively weak tides in GB, using the 10th and 90th percentile depths will shorten this range to between 0.5-1.2 m.

A typical ADCP deployment cycle began at the off-site lab by confirming all data from the instrument's previous deployment was downloaded and cleared from the internal memory. Data transfers were accomplished via connecting the ADCP to a computer using a specialized cable and software provided by Nortek. Following the stored memory check, the deployment settings were then initialized in the software application using a saved setting regime that ensured deployment conditions were consistent throughout the project. Data collection was set to begin around an hour after the instrument was expected to be deployed at the site; an ending time to stop data collection was unnecessary as the instrument could be switched off once retrieved and returned to the off-site lab. Biofouling prevention was then applied to ensure maximum fidelity of the collected data, a new internal battery was connected, and at this stage the ADCP was primed for field deployment.

Deployments typically lasted for about a month as this stretch of time would drain most of the single-use internal battery while also providing the maximum amount of time before the ADCP accumulated a problematic amount of biofouling in the warmer months. At the end of a deployment period, the ADCP would be raised from the water, swapped out for a fresh ADCP, brought back to the lab, have the data downloaded, and then undergo a full cleaning to remove any accumulated biofouling. Biofouling would typically accumulate on the 3 main acoustic transducers (Fig. 13), inside the pressure transducer (Fig. 12), and all along the body of the instrument. With the cleaning completed, the internal battery was at last removed, and the ADCP was stored until the time came for the next deployment.

Fig. 14 – Photograph of the platform section presented in Fig. 14.

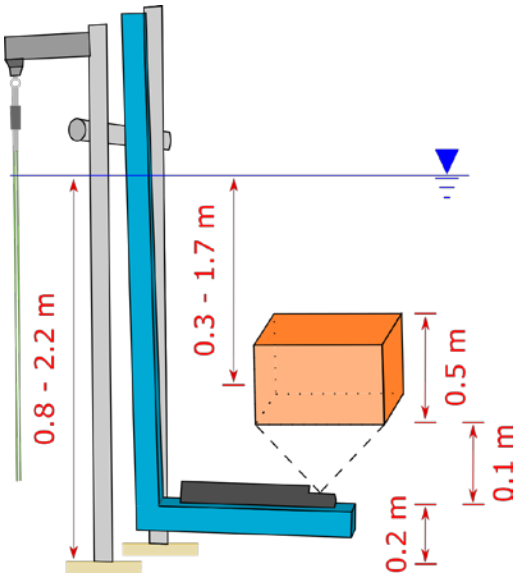

Fig. 15 – Unscaled schematic of ADCP sampling volumes and other notable dimensions

For studies or projects that involve a fixed period of field research, the ideal outcome is naturally to have complete and uninterrupted data collection throughout the allotted time span. Reality often prevents such ideal coverages, however, as is seen in the data collection summary seen in Table 5. Reasons for periods of missing data include:

- Periodic sensor maintenance (i.e., pulling ADCP from the site for battery exchanges, data downloads, memory wipes, and biofouling removal)
- Sensor failure (i.e., wave gauge lines snapping and water sampler pump failure)
- Corrupted measurements (i.e., the raised bed level post-dredging covering the altimeter, covering the water sampler tube intake end, and preventing the ADCP mount arm from fully extending)
- Power loss (i.e., batteries powering the camera and server dying after overnight freezes and build-up of bird waste on solar panels preventing requisite battery charging)
- Unavailable data (i.e., incomplete timeseries of USCG provided AIS data)

Table 5 – Overview of the available instrumentation and when valid data exists for each instrument

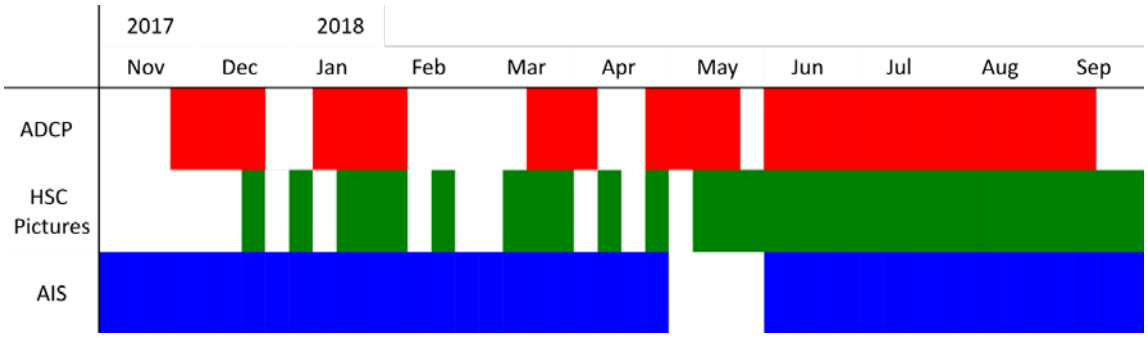

3.3 Measured In-Situ Conditions

All time stamps in the following sections are noted as following UTC reference time unless otherwise stated.

3.3.1 Wind

Wind-generated waves are the product of surface-level wind shears imparting energy into a body of water. The straight-line distance the wind travels along the water body's free surface, known as the fetch, is therefore a key determinant for how much energy transfer the shear force ultimately engenders. Fetch lengths for irregularly shaped shorelines can be calculated using the effective fetch method proposed by ERDC in the Shore Protection Manual [ERDC, 1977]. This method is performed via delineating 15 radials spaced 6° apart with the central radial matching the predetermined direction of wind propagation. As there are 7 radials to either side of the central radial, a 90° wide zone radiating from the site is created. It is assumed that any energy transmission by the wind will occur within this 90° zone (i.e., within 45° to either side of the primary propagation direction). Each radial is extended outward until the shoreline is reached, and after the radial distances are calculated they are then multiplied by the cosine of the corresponding angle made with the primary direction. The product of each radial length and angle cosine are then summed and divided by the sum of all the angle cosines, resulting in the effective fetch (16):

$$F_{eff} = \frac{\sum X_i \cos(\alpha_i)}{\sum \cos(\alpha_i)} \tag{16}$$

Wherein X_i is the distance from the site to the shoreline along radial i and α_i is the angle between the central radial and radial i. Figure 16 shows an example of radial delineations in GB for wind propagating in both north-northeasterly and west-southwesterly directions. These directions were chosen due to each providing the maximum effective fetch to either side of the bay; the site is notably located leeward of the dredge disposal island to the southeast.

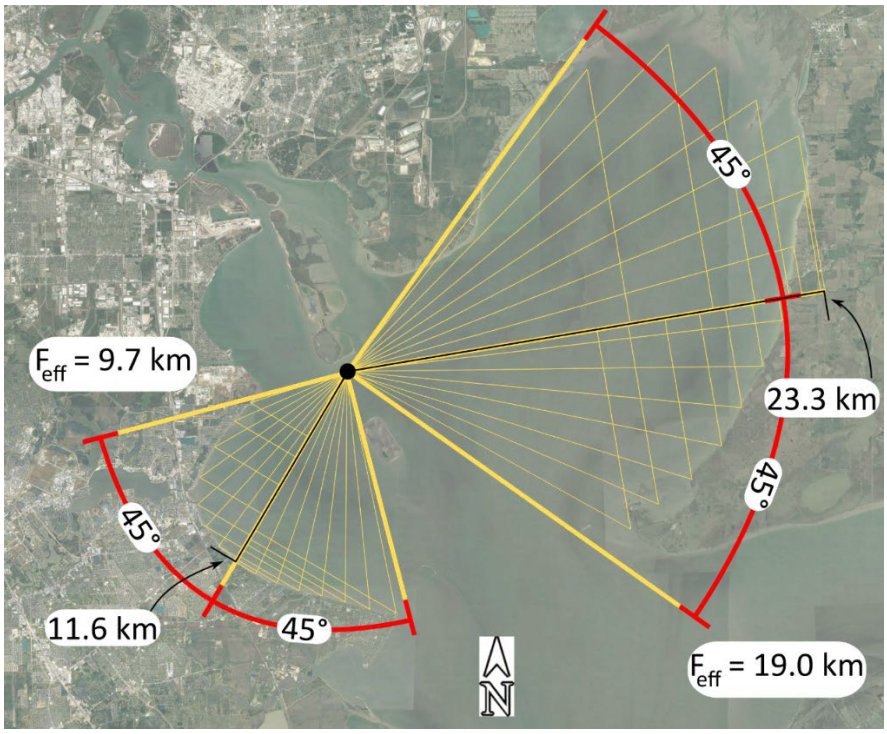

Fig. 16 – Illustration of how the maximum effective fetches were calculated for the irregular shoreline of Galveston Bay using the method recommended by ERDC (1977).

Reported wind values are as measured by the National Oceanic and Atmospheric Administration (herein NOAA) station "MGPT2" located at Morgan's Point (Fig. 9). The magnitude and direction of a sustained velocity value are the average over a 6-minute span, while the gust magnitude and direction record the single highest measurement during that same 6 minutes. The 6-minute

timespans are centered around the reported timestamp. A timestamp of 12:00 thus represents measurements from 11:57-12:03.

Wind directions are noted to have undergone two translations: first, a shift from the clockwise meteorological axis orientation (i.e., North at 0° and East at 90°) to a counterclockwise engineering orientation (i.e., East at 0° and North at 90°) followed by a second shift from directions defined by the heading of origin to directions defined by the heading of travel (i.e., a direction that was 270° is now 90°). These translations synchronize the wind direction axis with the axis orientation used during hydrodynamic analysis.

Figure 17 highlights the variance present throughout the year of data collection via partitioning the verified NOAA wind record by season. The subplots are organized into directional bins with widths of 22.5° and are centered around either a cardinal (i.e., north), intercardinal (i.e., northeast), or secondary intercardinal (i.e., east-northeast) direction. Two key data streams are overlaid: the bin measurement frequency (i.e., the left, black ordinate) and the corresponding average velocity of each bin (i.e., the right, red ordinate).

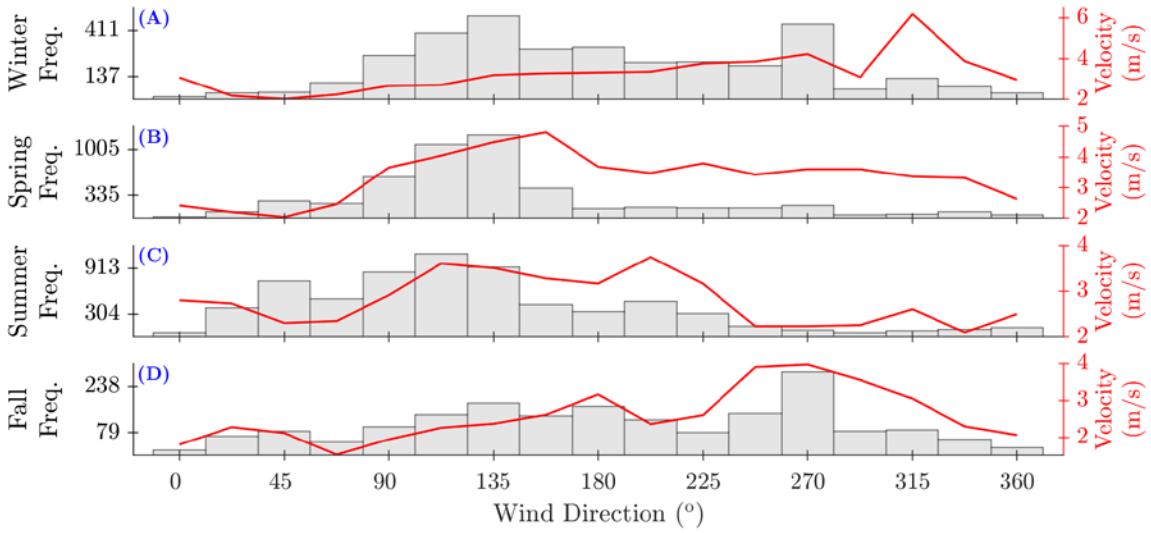

Fig. 17 – Seasonal histograms of the wind direction at the site overlaid by the corresponding mean wind velocity for each directional bin. Values recorded by NOAA meteorological station MGPT2, located near Morgan's Point, Texas.

Table 6 delves deeper into the frequency distributions via aggregating the directional bins into 5 nonuniform groups based off the expected frontal and sea/bay breeze processes discussed in section *3.1.3.* As an example, group 2 ranges from 78.8-168.8° and encompasses winds blowing anywhere between north and west-northwest, or roughly onshore at the site. Onshore-directed winds may be the product of sea/bay breezes, mT fronts moving inland from the Gulf of Mexico, or cP/mP fronts reversing direction northwards after penetrating into the Gulf.

To arrive at a single seasonal value for each grouping, the individual measurements were first partitioned into sets bounded by the starting and ending timepoints of the ADCP bursts. A single averaged value was calculated for each burst and typically consisted of 2 or 3 values. A maximum of 3 values (i.e., 18 minutes of measurements) were potentially able to occur during a 17.5-minute ADCP burst due to the NOAA timestamps reporting the 6-minute collection period midpoint as previously discussed. With each burst now reporting a single average wind direction and velocity magnitude value, the middle time index of each burst was used to determine what season the burst belonged to. The seasonally categorized values then underwent one final sorting relative to the 5 directional bin groupings to give the tabulated results.

Table 6 – Distribution of binned seasonal wind directions normalized to frequency per bin degree. Cell shades correspond to direction frequency with darker shades indicating greater frequency. Shade changes occur at 0.2, 0.4, and 0.6 frequency counts per degree.

	Seasonal Frequency Distribution $\left({Group\ Frequency}/{Degree}\right)$				
Group #	1	2	3	4	5
Group range (Group size)	0.0-78.8° (78.8°)	78.8-168.8° (90°)	168.8-236.6° (67.8°)	236.6-303.8° (67.2°)	303.8-360° (56.2°)
Winter	0.08	0.48	0.33	0.31	0.13
Spring	0.15	0.74	0.14	0.12	0.07
Summer	0.32	0.55	0.24	0.06	0.08
Fall	0.15	0.34	0.30	0.42	0.17

Directional observations from Fig. 17 and Table 6 include:

- The directional frequencies across the grouped bins show similar behavior during the fall/winter seasons and to a lesser extent during the spring/summer seasons.

- Group 2, or the directions between the north bin minimum (i.e., 78.8°) and the west-northwest bin maximum (i.e., 168.8°), were the most consistent directional grouping throughout the year.
    - The largest grouping as it represents 25% of the total bin range;
    - The dominate wind direction during winter (43.2%), spring (66.6%), and summer (49.5%), also the second most dominate direction during fall (30.6%);
    - There is a moderate overlap between group 2 directions and several of the radials drawn for the western reach's effective fetch in Fig. 16 (i.e., just under half of the radials).
- Group 3, or the directions between the west bin minimum (i.e., 168.8°) and the southwest bin maximum (i.e., 236.3°), were the second most consistent directional grouping during the year.
    - Group 3 wind directions have nearly complete overlap with the radials drawn for the eastern reach's effective fetch in Fig. 16.

Wind velocity magnitudes are organized in Table 7 using the same approach of aggregating the directional bins into 5 groupings as was done for the directional frequencies in Table 6. The mean and maximum values reported in Table 7 correspond to the seasonally sorted mean and maximum magnitudes from each group of binned wind directions. As an example, the burst with the second highest maximum wind magnitude in the fall (11.6 m/s) was found to propagate in a direction corresponding to group 3, yet the average value of all bursts associated with group 3 (2.8 m/s) remains below the 50th percentile average velocity magnitude (3.0 m/s).

Table 7 – Average and maximum seasonal velocities measured across each grouping of directional bins. Cell shades corresponds to velocity magnitude with darker shades indicating greater magnitude. Shade changes occur at 2.5, 3.5 and 4.5 m/s for the mean velocity magnitudes and at 7, 9, and 11 m/s for the maximum velocity magnitudes.

	Seasonal Velocities ($^{m}/_{s}$)				
Group #	1	2	3	4	5
Group range (Group size)	0.0-78.8° (78.8°)	78.8-168.8° (90°)	168.8-236.6° (67.8°)	236.6-303.8° (67.2°)	303.8-360° (56.2°)
Winter Mean	2.3	3.0	3.5	4.0	4.9
Spring Mean	2.2	4.2	3.7	3.5	3.2
Summer Mean	2.4	3.4	3.4	2.2	2.4
Fall Mean	2.0	2.3	2.8	3.9	2.6
Winter Max	5.5	7.5	8.2	8.8	12.1
Spring Max	5.2	9.7	11.5	8.8	9.8
Summer Max	9.2	8.9	8.7	6.7	4.9
Fall Max	5.1	6.6	11.6	8.9	8.2

Velocity magnitude observations from Fig. 17 and Table 7 include:

- Group 5, or the directions between the southeast bin minimum (i.e., 303.8°) and the east bin midpoint (i.e., 360°), recorded the largest average burst velocity (4.9 m/s) and the burst with the largest maximum velocity (12.1 m/s) during the winter season.
    - Frontal activity peaks in the winter months [Henry, 1979].
    - The front creating the 12.1 m/s maximum burst magnitude was likely of the mP variety.
        - mP fronts often constitute the majority of frontal systems in winter months
        - mP fronts usually enter the Gulf of Mexico west of Galveston while cP fronts enter from the east [Henry, 1979]. As group 5 propagates east-southeasterly, there is a strong indication the frontal system would perforce arrive from the west.
    - Notably, group 5 was essentially the least frequent direction of wind propagation (Table 6). This implies there is a relatively considerable wind-wave energy divergence in this group of binned directions that is dependent on the presence of frontal activity.
- Not only were group 1 bins the second least frequent directions of propagation (Table 6), but these directions also consistently reported the weakest average velocity magnitudes (2.2 m/s $^{+}/_{-}$ roughly 0.2 m/s, Table 7).
    - Indicates frontal systems seldom propagated in a northeasterly direction.
    - The maximum burst velocity magnitudes were extremely consistent throughout the year (5.3 m/s $^{+}/_{-}$ roughly 0.2 m/s) with the notable exception of Summer (9.2 m/s), potentially indicating the presence of a strong mT system
        - mT fronts most commonly active during the summer [Schroeder & Buck, 1970].

3.3.2 Hydrodynamics

A visual summary of the measured current velocity magnitudes and directions during the entirety of the data collection period is found in the right panel of Fig. 18 and the corresponding wind record is to the left. The approximate headings of the +u (i.e., perpendicular onshore) and +v (i.e., parallel alongshore towards the HSC) axes are also shown in red. The hydrodynamic record includes a total of 29,214,720 timepoints; each timepoint details the instantaneous water surface elevation, current velocity magnitude, and current velocity direction. The wind record includes a total of 73,308 6-minute averaged timepoints.

The background current at the site is fairly uniform over the 10-month collection period (right panel of Fig. 18) while the wind again shows clear onshore directional dominance (left panel of Fig. 18) in agreement with Tables 6-7. The uniformity of the current magnitudes and directions

is expected given both the relatively long period of data collection and the site location being a confined tidal basin.

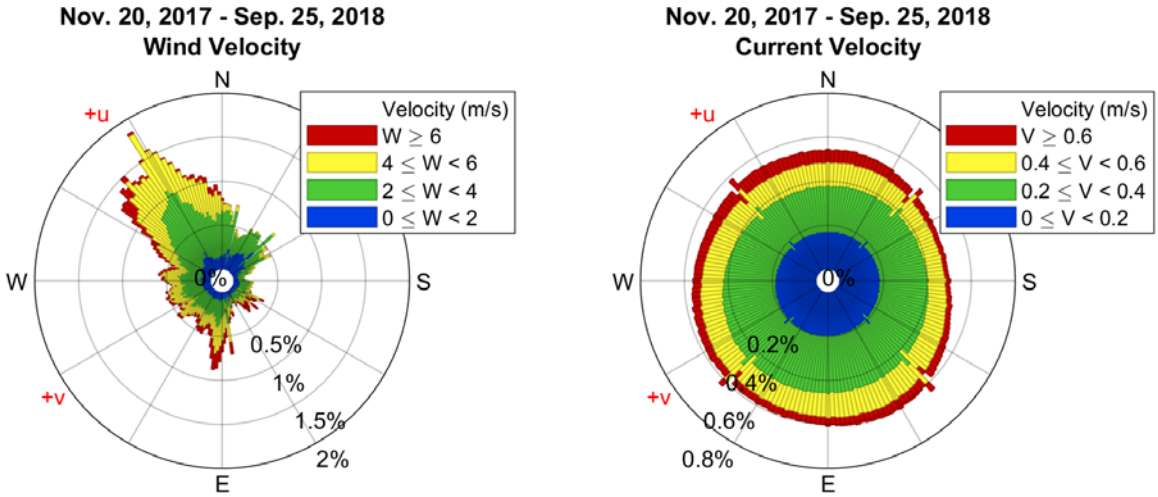

Fig. 18 – Wind rose styled plots of the wind (left) and current (right) measurements during the entire data collection period. Collection occurred from November of 2017 through September of 2018.

3.3.3 Vessel Traffic

Investigations into RQ1 (i.e., whether trends in VGW event hydrodynamics can be explained through correlations with vessel parameters) first necessitated linking individual wake events to the specific vessel responsible for generating the event. As the hydrodynamic data were time-localized, a similarly time-dependent history of vessel traffic could be used to establish such linkages. The vessel traffic information used in this project was recorded via the internationally recognized marine tracking system known as the automatic identification system (herein AIS, Fig. 19). AIS functionality is summarized by the International Maritime Organization as needing to [IMO, 2019]:

- Provide information automatically to appropriately equipped shore stations, other ships, and aircraft;
- Information to be provided include vessel parameters such as: ship identity, type, size specifications, position, course, speed, and navigational status.
- Receive automatically such information from similarly fitted ships;
- Monitor and track ships;
- Exchange data with shore-based facilities.

AIS transponders are mandated for any passenger ship, any cargo ship 500+ gross tonnage not traveling internationally, and any ship 300+ gross tonnage traveling internationally. Vessels meeting any of these mandate guidelines are expected to maintain AIS operation at all times, with the exception of cases where the international agreements, rules, or standards allow for the protection of navigational information [IMO, 2019]. The commercial tanker and cargo vessels relevant to this project are noted as not qualifying for such protections and are thus expected to broadcast AIS information without exemption.

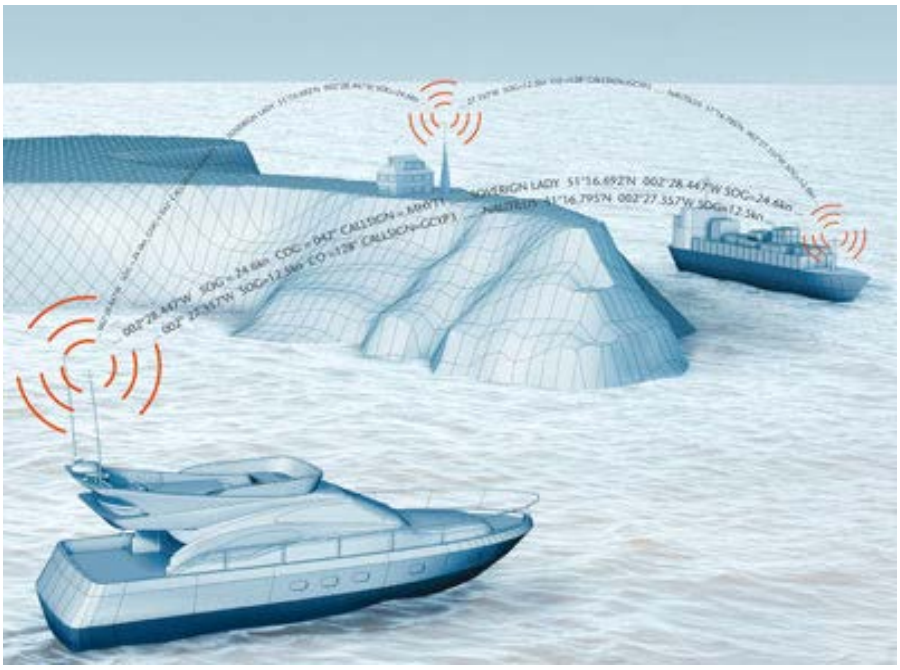

Fig. 19 – Cartoon schematic detailing the principles of AIS. Marine traffic control information can be observed passing between the vessels and shore-based station. Image adapted from IMO (2019).

AIS databases are managed by both private interests and governmental entities; the database providing informational access to this project was sourced by ERDC from the United States Coast Guard (herein USCG). Contained in the USCG AIS database were 2 main data streams: the vessel traffic timeseries and a spreadsheet compiling all available parameters for each of the vessels found in the traffic timeseries. Examples of parameters from the spreadsheet data included vessel type, draft, length, and beam; examples of the information recorded in the traffic timeseries included the timestamp, position, heading, speed, and turn rate.

In order to limit the database to records potentially relevant to this project, ERDC reduced the records down to those containing spatial coordinates falling within the circumscribed box drawn in Fig. 20. The box extents, 2.36 nautical miles vertical by 2.50 nautical miles horizontal, are set such that multiple AIS entries should be theoretically available for each transit within the project site, regardless of transit direction.

Multiple entries are expected given AIS broadcast rates are typically on the order of seconds, specifically every [MarineTraffic, 2021; USCG, 2020]:

- 180 seconds within 15 minutes prior to unmooring
- 10 seconds if sailing 0-14 knots;
- 6 seconds if sailing between 14-23 knots;
- 3.3 seconds if sailing 0-14 knots while changing course;
- 2 seconds if sailing between 14-23 knots while changing course.

Despite this study being designed to capture every wake event impacting the site, inherent limitations invariably prevented a complete capture of all events. Examples of such limitations include:

- Incomplete capture due to any portion of an event occurring outside ADCP collection periods (i.e., while no ADCPs were onsite or between the periods of active ADCP data collection);
- Events from two ships transiting in opposite directions arriving close enough such that the wakes superimposed and prevented the isolation of the wakes individually;
- Events unable to be captured during analysis due to weak hydrodynamic wake effects (i.e., transits by smaller or unloaded vessels during windy conditions and/or high tides);
- Wakes successfully captured unable to be identified due to missing AIS records.

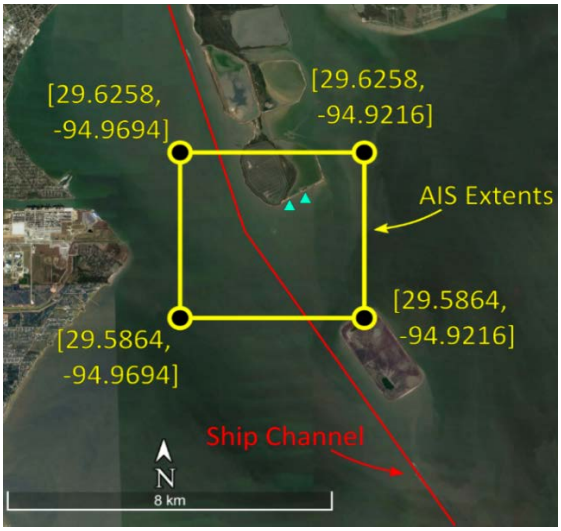

Fig. 20 – Extents of AIS data collection with the two research platforms denoted by the blue triangles.

The AIS data required minimal processing as the only adjustment was to convert the original timestamps from universal time (UTC) into local time (CST). This conversion synchronized the traffic timeseries to the time standard used in ADCP measurements, thus allowing for the desired time-dependent linkages between vessels and observed wake events to be made. The exact method for linking any given wake event to the correct generating vessel is discussed in the later methodology section (section *4.2.8*).

Summaries of key parameters from vessels positively identified during the data subset are provided in Table 8 and Fig. 21.

Table 8 – Minimum, mean, maximum, and standard deviation of select vessel parameters. Each vessel is only counted once towards the statistics, regardless of how many transits the vessel recorded.

Type	Count		Length (m)	Draft (m)	Gross Displacement (tons)	Fr_l
Cargo	948	Min	87.5	4.5	2,978	0.046
		Mean	204.3	9.2	34,599	0.13
		Max	335	14	90,745	0.32
		Std Dev	51.1	2.1	19,966	0.032
Tanker	1,346	Min	107	4.8	4,693	0.051
		Mean	187.4	9.3	31,187	0.13
		Max	277	14	85,431	0.3
		Std Dev	36.7	2	17,209	0.026

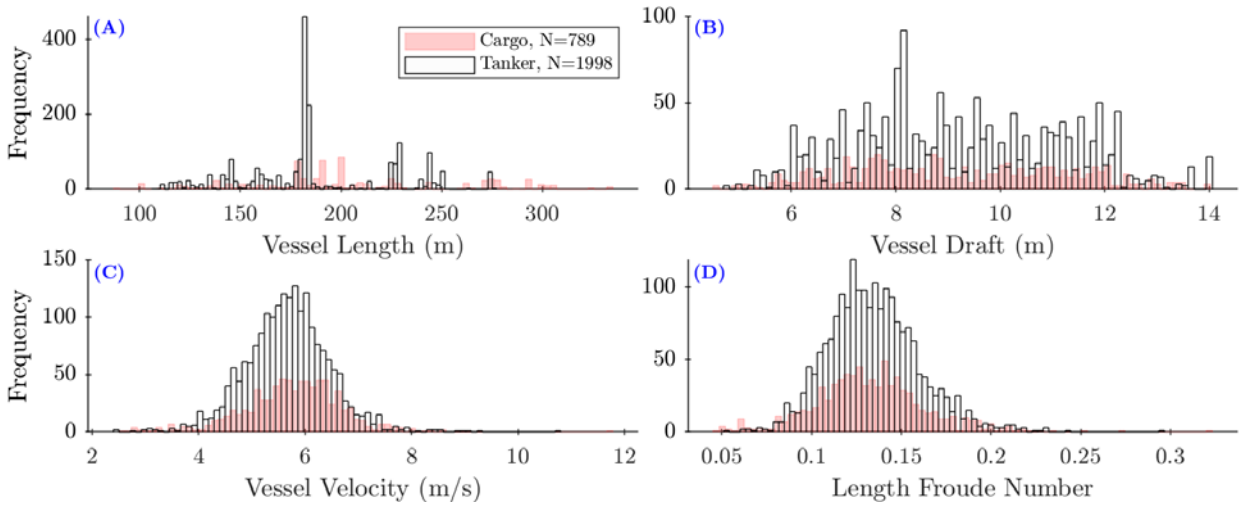

Fig. 21 – Summaries of vessel parameters corresponding with wake events identified during the study.

Additional notes on HSC deep-draft vessel traffic statistics during the study period, keeping in mind May 2018 lacked all AIS records, include:

- A total of 11,707 vessel transits were recorded
- 2,394 unique ships were identified in the study, of which 2,294 contained vessel type information
    - 948 cargo vessels (41% of vessels) made 3,548 transits (30% of transits)
    - 1,346 tanker vessels (59% of vessels) made 8,159 transits (70% of transits)
- An average of 1,372 transits occurred per month
    - February recorded the minimum average transits per day (41.2)
    - March recorded the maximum average transits per day (51.4)

Figures 22-23 provide example images of an inbound cargo and outbound tanker vessel transiting the HSC as taken by the camera mounted to platform Simon along with a higher resolution image of each vessel.

Fig. 22 – Inbound transit photo of cargo vessel MSC Heidi taken by the camera mounted to platform Simon on July 28th, 2018 at 15:05 (top) and high-resolution image of the same vessel for reference (bottom).

Fig. 23 – Outbound transit photo of tanker vessel Zaliv Baikal taken by the camera mounted to platform Simon on July 28th, 2018 at 14:55 (top) and high-resolution image of the same vessel for reference (bottom). Note the surface wake component of the event can be seen rounding the embankment as a white-capped broken wave.

4.0 Methodology

4.1 Data QA/QC

4.1.1 General

Processing raw hydrodynamic data using quality assurance and quality control techniques (herein QA/QC) is imperative for confirming collected data as accurate and substantive. Numerous avenues exist whereby measurements can experience fidelity reduction or outright corruption, ranging from user errors to environmental conditions. Table 9 lists several such sources of erroneous data that are particularly relevant to ADCP sensors, along with a few suggested methods for addressing each source [Elgar et. al, 2005; Elgar et. al 2008].

Table 9 – Sources of faulty ADCP velocity data measurements and their potential solutions. Some of the sources listed are as noted in Elgar et. al (2005) and Elgar et. al (2008).

Source	Effect	Solution
Rapidly moving particles within the sampling volume	Phantom or successive returns corrupting data measurements	QA/QC post-processing of the data stream
Excessive acoustic scatterers in the water column	Injects noise into the data signal	QA/QC post-processing of the data stream
Weak scatters unable to provide sufficiently strong returns	Low confidence in reported measurements	QA/QC post-processing of the data stream
Biofouling blocking acoustic beams (or clogging pressure transducers)	Degrades the accuracy and precision of measurements	Biofouling prevention steps pre-deployment; deep cleaning post-deployment; reduced deployment duration periods
Surfzone phenomena such as accreting beds, excess bubble entrainment, or subaerial exposures	Partial or total failure of the acoustic beams or pressure transducer	Cognizance of the local surfzone behavior across all conditions; appropriate deployment regimes; frequent instrument checks
Insufficient battery power supply	Nonstationarity in the collection process; outright sensor failure	Confirm battery status pre-deployments; appropriately planned deployment durations; awareness of collection settings relative to power usage
Instrument uses improperly programmed collection settings	Suboptimal data collection; data does not represent the intended collection parameters	Carefully review settings pre-deployment; fully understand how each setting option alters performance; ensure settings are optimized for the collection goals given the expected site conditions

4.1.2 Velocity Data Processing

Post-deployment QA/QC of the recorded velocity data took the form of the following steps:

1) *Set the signal-to-noise ratio threshold for the specific deployment*

   Signal-to-noise ratio (herein SNR) is the acoustic signal strength relative to the background noise level. The background noise level is not explicitly given by the Nortek ADCP, however the strength of measurement amplitudes while the ADCP is out of water can provide a sufficient proxy [Nortek, 2019]. Each of the project deployments experienced background noise (i.e., subaerial measurements) at either the beginning or end of the collection period. Subaerial measurements occurred at the beginning of deployments if the instrument was not installed before the predetermined start time of data collection, and occurred at all deployment endings due to measurements not ceasing until after the instrument was transported from the field site to the lab for post-deployment processing. Background noise amplitudes are noted as stationary between the start and end of the deployment. The Nortek manual only notes "…data will be questionable when [amplitude] signal levels are down around the [background] noise level" [Nortek, 2008a], however a comprehensive threshold was found to be (17):

$$SNR\ Threshold = 3 * Noise\ Floor \tag{17}$$

   Empirically adjusted SNR thresholds for acoustic Doppler instruments across various manufacturers have been found up to 8 times the noise floor [Elgar et. al, 2005]. With the amplitude strengths recorded as integer values known as counts, the noise floor was calculated using the mode value of the amplitude strengths below 50 counts. The 50-count value was chosen to split the background noises (i.e., typically 20-25 counts for the 2 Mhz ADCP) from the measured data (i.e., typically starting at around 60 counts). Figure 24 plots histograms of the amplitude strengths across the 3 ADCP axis beams (Fig. 13) during the first deployment.

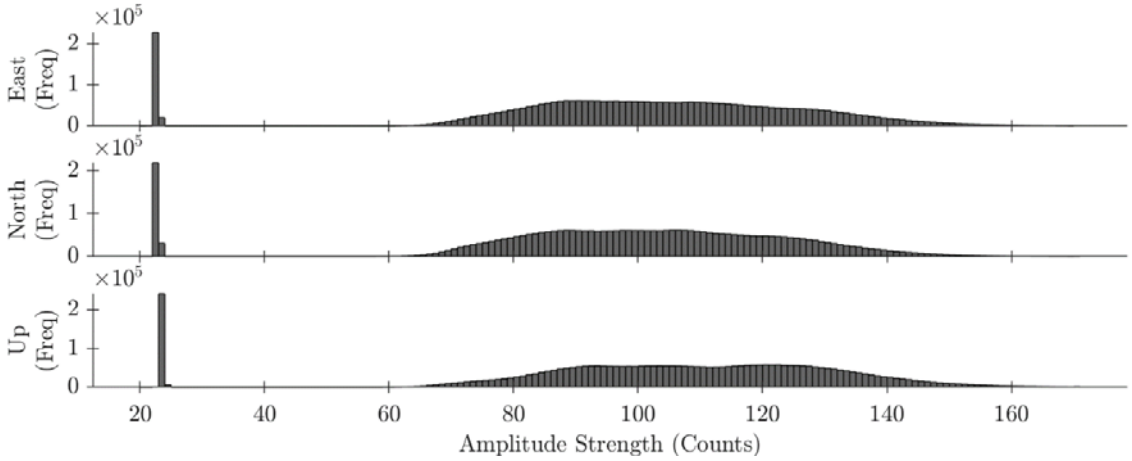

Fig. 24 – Histograms of the Easting, Northing, and Upward directed beam amplitude strengths of the ADCP during the first deployment (i.e., between November and December of 2017). The background noise level is observed via the large concentration of values at the 22- and 23-count bins while the potentially valid data are the values spread between 60 and 160 counts.

2) *Set the maximum feasible velocity threshold*

As a check for unreasonably high velocity magnitudes that would otherwise pass QA/QC using the amplitude value, velocity component thresholds were set at 1.5 m/s for the northing and easting beams (i.e., the u and v components after conversion from ENU coordinates into uv coordinates) and 1 m/s for the upwards beam.

3) *Determine how many measurements failed the SNR or maximum velocity thresholds in each burst*

To pass the velocity QA/QC, each 17-minute burst of 2048 datapoints was required to have less than 50 datapoints (i.e., 2.4% of the burst) failing either the SNR or feasible velocity magnitude thresholds across any of the 3 beams. The 50-datapoint allowance was set using (18) [Elgar et. al, 2005]:

$$n_i = 25 * f_s \tag{18}$$

Wherein n_i is the number of allowable erroneous datapoints in the burst along beam i and f_s is the sampling frequency of the instrument.

4) *Address erroneous measurements if necessary*

Bursts with 1 or more beams containing between 1 and 49 instances exceeding SNR or velocity magnitude thresholds were corrected by replacing erroneous datapoints with values predicted by cubic spline interpolation. Bursts with 1 or more beams containing 50 or more erroneous points were tossed altogether as the overall burst was then considered corrupted.

5) *Convert velocity component coordinates from ENU to uv*

The translation of velocity components from an ENU coordinate system over to uv was accomplished using (19):

$$uv = \frac{ENU}{\cos(\alpha)} \tag{19}$$

Wherein uv is the cross-shore perpendicular (i.e., u) or alongshore parallel (i.e., v) component value, ENU is the easting (i.e., roughly alongshore) or northing (i.e., roughly cross-shore) component value, and α is the angle between the ENU and uv axes. For this site, α was 31° (Fig. 25). As the positive v component points alongshore parallel towards the HSC, the easting component is also noted as needing to be "flipped" via multiplying the value by negative 1.

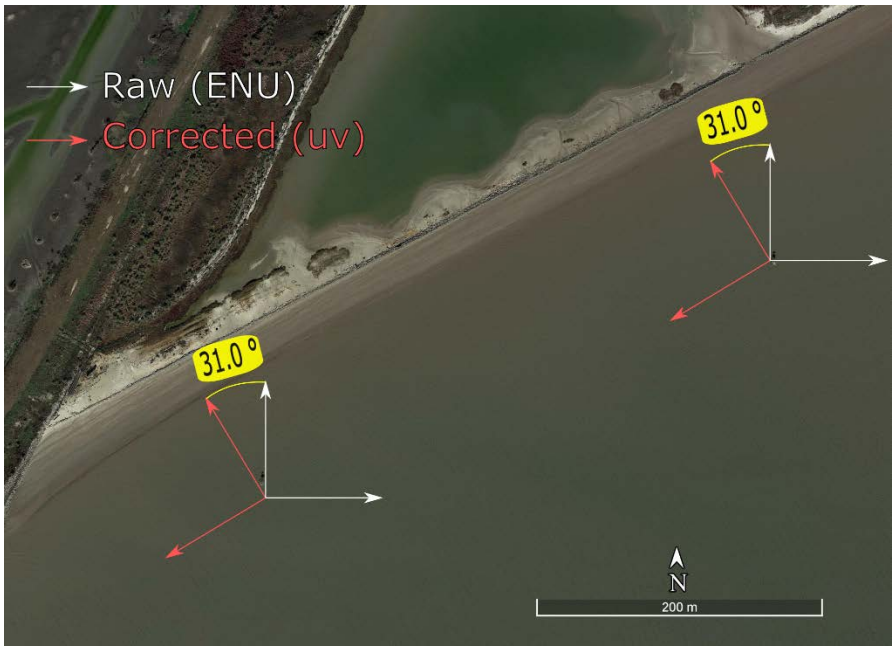

Fig. 25 – Illustration of ENU (i.e., white arrows) and uv (i.e., red arrows) axes orientations at the site. Each set of arrows originate at one of site platforms.

4.1.3 Pressure Data Processing

The QA/QC process for the pressure data was notably different than that for the velocity data. This discrepancy was due to the velocity measurements having the ability to gauge fidelity using acoustic return amplitudes, in contrast to the pressure measurements which had no such supporting indicators. The post-deployment QA/QC of the recorded pressure data took the form of the following steps:

1) *Identify peaks and troughs in the pressure data for each burst*

   Without referencing the pressure-velocity relationship defined by LWT, invalid pressure measurements were distinguished via identifying outliers in the recorded timeseries. As single-point outliers take the form of large deviations from the surrounding values, it was assumed corrupted measurements would exist as a peak or trough in the signal. The pressure-velocity relationship derived in LWT was not utilized due to 2 main reasons: the inability of the relationship to determine whether the pressure measurement, velocity

measurement, or a combination of both constituted the incorrect value(s), and the additional error introduced by the inclusion of interpolated velocity values.

2) *Differentiate each burst of pressure data into first and second order differentials*

Single-point outliers in the pressure signal naturally present unusually strong jumps or spikes between successive points. Taking both the first differential (i.e., the rate of sea-surface elevation change) and second differential (i.e., the acceleration in the rate of sea-surface elevation change) of the pressure signal thus elucidates the corrupted pressure measurements by identifying potential instances of infeasible or unnatural first and second order rates of change.

3) Determine the location of outliers in both differentials for each burst

The potential occurrences of infeasible rates of sea-surface elevation changes are confirmed via searching for outliers. The median absolute deviation (i.e., MAD) method was used for determining outliers (20):

$$MAD = \frac{-1}{\sqrt{2} * erfcinv\left(\frac{3}{2}\right)} * median(|A_i - median(A)|) \quad (20)$$

Wherein $erfcinv$ is the inverse complementary error function, A_i is the i^{th} value in the vector A, and a MAD of 3 or greater indicates A_i as an outlier.

4) Correlate peak/trough locations with identified rate of change outliers

A pressure measurement must exist as a peak or trough in the recorded signal and constitute an outlier in both orders of signal differentials to be classified as invalid.

5) Address erroneous measurements if necessary

Pressure transducer data is less susceptible to multi-measurement periods of unfavorable collection conditions as compared to acoustic Doppler velocity data (i.e., the majority of error sources listed in Table 9 are only applicable to acoustic Doppler sensors). With invalid pressure measurements therefore assumed as single-point occurrences, a limit to how many invalid measurements could be allowed per burst was rendered unnecessary; all pressure measurements classified as invalid were corrected by simply averaging the surrounding values. The per-burst limit on invalid velocity measurements is noted to serve as a proxy for identifying bursts impacted by extended periods of unfavorable collection conditions (i.e., on

the timescale of tens of seconds), thus without a similar susceptibility to these periods, the pressure signal has no need to be limited using this proxy.

4.1.4 Pressure verification using NOAA tidal records

Water surface elevation data (i.e., the pressure timeseries) passing QA/QC was given a final validity check via comparison to the Morgan's Point NOAA tide station located about 8.75 km northeast (Fig. 9). To accomplish this, verified tidal records from the station were divided into 10 different timeseries, whereby each timeseries had starting and ending record timestamps that matched one of the 10 ADCP deployments. The NOAA tidal records were then interpolated using a cubic spline such that the original timeseries of 6-minute measurements were transformed into 0.5-second measurements to match the ADCP sampling rate. Figure 26 plots the results of subtracting each ADCP water surface elevation measurement from the interpolated NOAA tidal record with a matching timestamp.

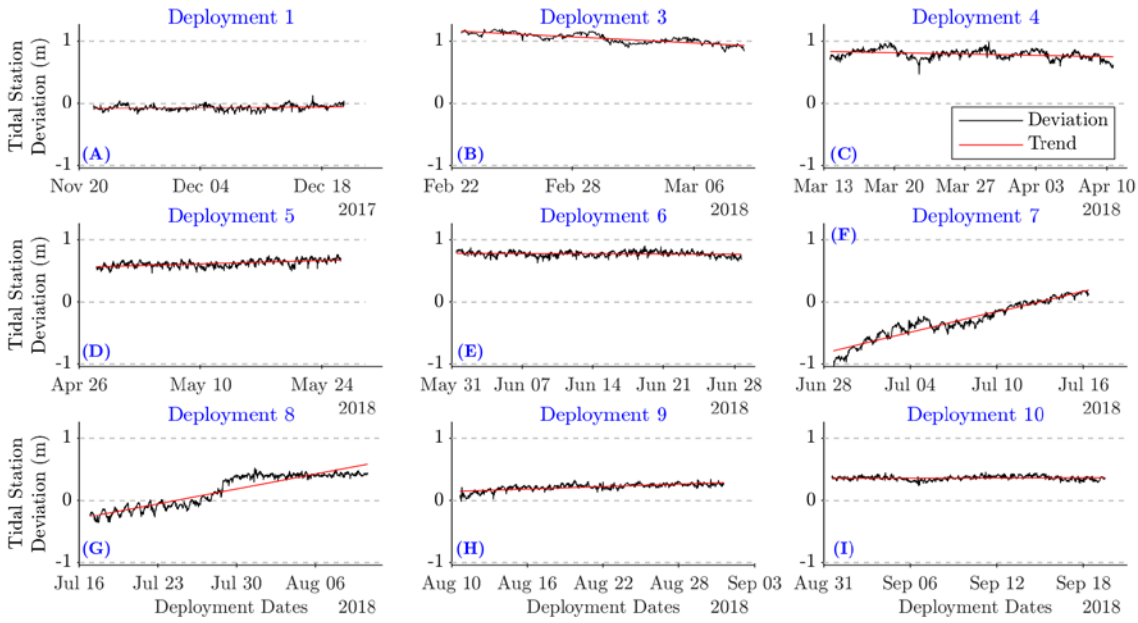

Fig. 26 – Deviations between verified NOAA tidal station records and the measured water levels from each ADCP deployment. Deployment 2 excluded due to a relatively major deviation across the full deployment. NOAA data from tide station 8770613 at Morgan's Point. Datum used for comparison was the "Station Datum" set by NOAA.

The ADCP water surface elevation timeseries were expected to show a mostly flat, linear deviation from the NOAA tidal record in order to pass final verification. This expectation stems from both measurement stations being located just a few kilometers apart in the same bay, meaning long-term changes in water levels would concurrently affect both sites. Potential causes of problematic water surface deviations could include biofouling accumulation on the pressure transducer, inadequate cleaning of the pressure transducer between deployments, or an issue in the data record from the NOAA station.

Deployments 1, 3, 4, 5, 6, 9, and 10 each passed without issue, however deployments 2, 7, and 8 (Fig. 26 panels F-G) either partially or fully failed inspection. Deployment 2 exhibited a deviation between -1 and -2 meters throughout the entire record and was excluded entirely from analysis. Deployment 7 (panel F) shows a fairly constant increasing slope throughout the deployment in addition to beginning with a deviation that is atypically negative and was removed from any analyses that required depth considerations. Deployment 8 (panel G) also starts unusually negative and linearly increases up until roughly halfway through the deployment, where it then flatlines for the remainder of the deployment. Since the second half of deployment 8 (roughly around July 29th) otherwise resembles the expected deviation, only the first half of the deployment was excluded from depth-dependent considerations.

4.2 Wake Identification

4.2.1 Decision Algorithm Overview

The process of identifying a VGW from in-situ measurements took the form of a multifaceted algorithm that coalesced multiple data streams into a final decision on whether an event arrival was occurring at any given moment. In all, a total of 5 different analysis techniques were eventually integrated into the algorithm, each attempting to provide an additional layer of confidence for the final outcome.

The need for numerous considerations was magnified due to both a small fraction of vessels missing AIS records and the methodology used to determine the vessel transits potentially found in any given ADCP data burst occasionally failing to register all relevant transits. These factors not only prevented the algorithm from relying on vessel transit logs, but also meant identification must occur completely independent of the AIS data, since logs were then essentially reduced to providing confirmation only. How the methodology for determining vessel transits in each data burst could occasionally miss transits is discussed in section *4.2.8.*

4.2.2 Multiresolution Analysis

The initial step in the decision chain was to deconstruct the pressure into discrete frequency bins with a Multiresolution Analysis. In this technique, orthonormal bases are derived for orthogonal projections onto orthogonal complements of closed subspaces known as Hilbert spaces (14). With the orthogonal basis defined, a timeseries is able to be mathematically partitioned into scaled components that still maintain time localization. This translates in practice to a water surface elevation profile decomposing into frequency bins scaled into octaves, that, once superimposed back over one another, recreate a surface profile identical to what was initially started with. The ability to maintain time localization is especially noteworthy considering Fourier Transforms, a mainstay in signal processing and coastal engineering, are unable to preserve time dependent signal events, such as VGW.

An example of a full multiresolution decomposition is shown in Fig. 27, where the original detrended water surface elevation profile of a complete ADCP data burst is shown in the topmost panel (panel A). The following panels then each contain the proportional amount of signal variance at any given time that originates from the corresponding range of time periods; adding the values of each scaled panel at time period t = x will result in the exact same t = x value found in the original signal. With each drop in bin level comes a drop in period octave, continuing until the highest frequency panel is bounded by the sampling frequency of the data series. For the second panel down, panel B, this would equate to wave energies found between the 128 to 256 second range, while the bottommost panel, panel I, designates energies between 1 and 2 seconds, the shortest periods considered during this analysis.

A unique benefit to multiresolution decomposition for VGW events in particular is the isolation of the Bernoulli and Havelock wake components. A Bernoulli pressure wave creating the large drawdown and subsequent surge is readily seen in Fig. 27 starting around the 02:35 timestamp in panels B-C, while the high frequency Havelock surface waves arrive soon after the 02:36 timestamp in panels G-I.

The deconstructed water surface elevation timeseries provided in Fig. 27 is the starting point for several of the analysis methods, including the first direct addition to the decision chain – a statistical summary of the burst. By taking the 8 individual bins and aggregating them into 3 (i.e., hi/mid/low frequencies), an indication of whether a wake is contained in the burst may be readily observed (Fig. 28).

This indication is a result of the extreme deviation from stationarity experienced by each deconstructed frequency bin upon arrival of a VGW. The abrupt arrival of the VGW wave packet radically alters the statistical summaries of the combined high and mid frequency bins (Fig. 28, panels D and C), especially when contrasted against equivalent bins from bursts without any VGW events. Figure 29 illustrates a typical example of a multiresolution analysis regrouped into 3 bins for a wakeless burst for reference.

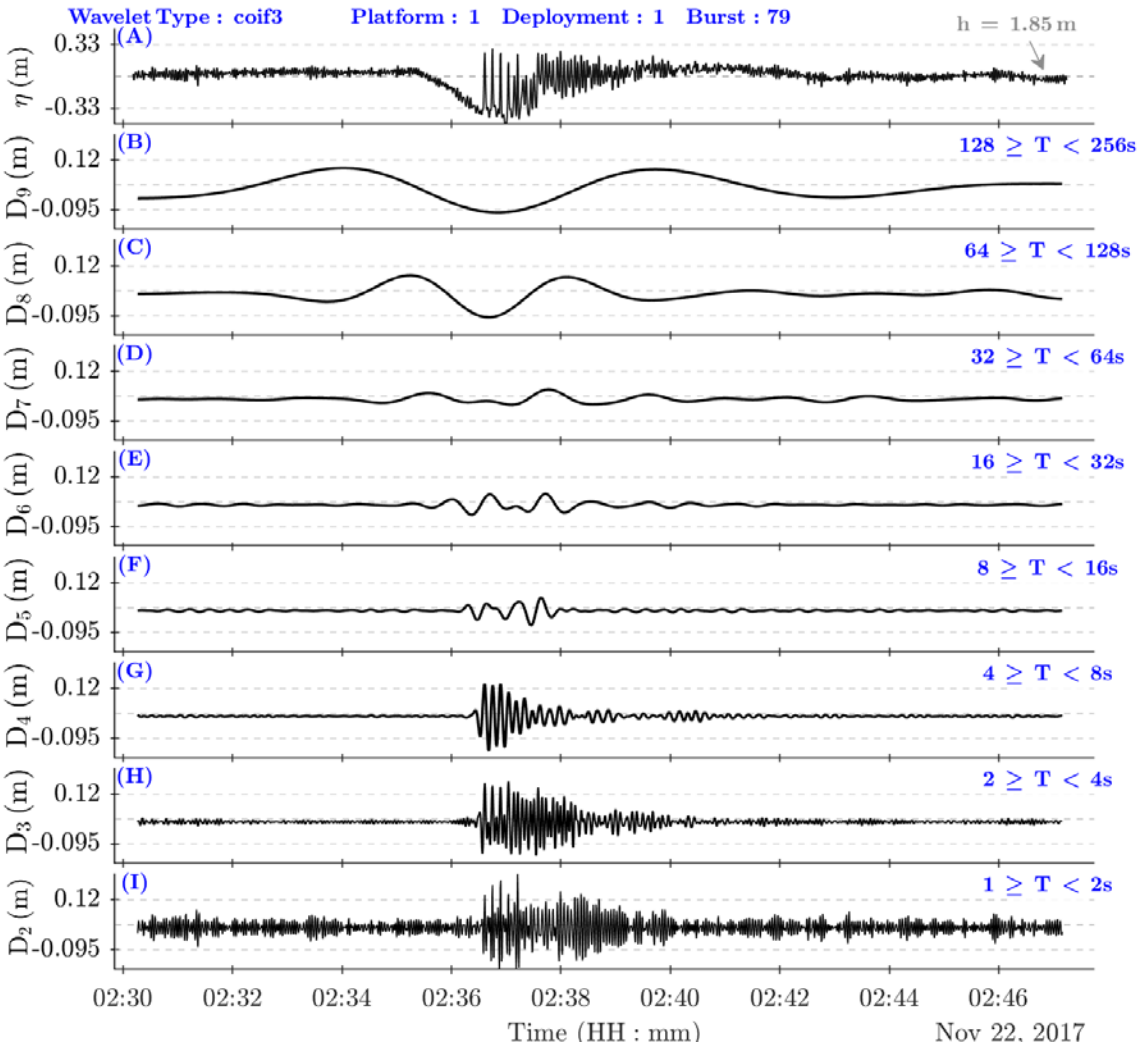

Fig. 27 – Multiresolution analysis of a water surface elevation time series containing an inbound wake event arriving just after 02:36.

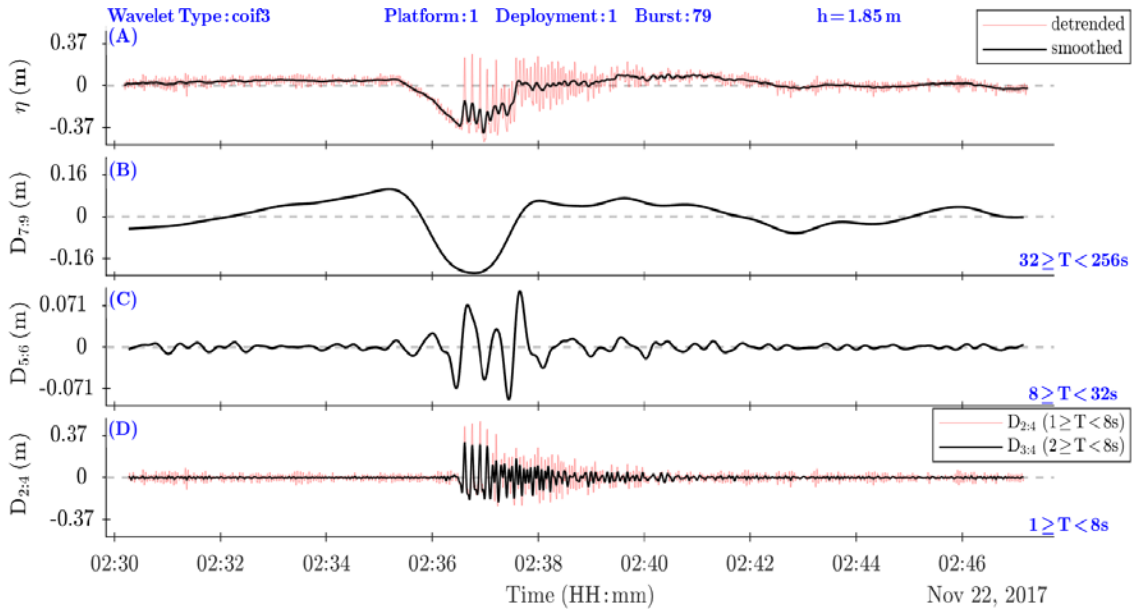

Fig. 28 – The decomposed signal of a burst containing an inbound wake regrouped into 3 main frequency bins. High frequency (panel D) now contains 1-8 second periods, mid frequency (C) contains 8-32 second periods, while the low (B) contains the remaining 32-256 second periods. Original detrended water surface elevation show on top (A).

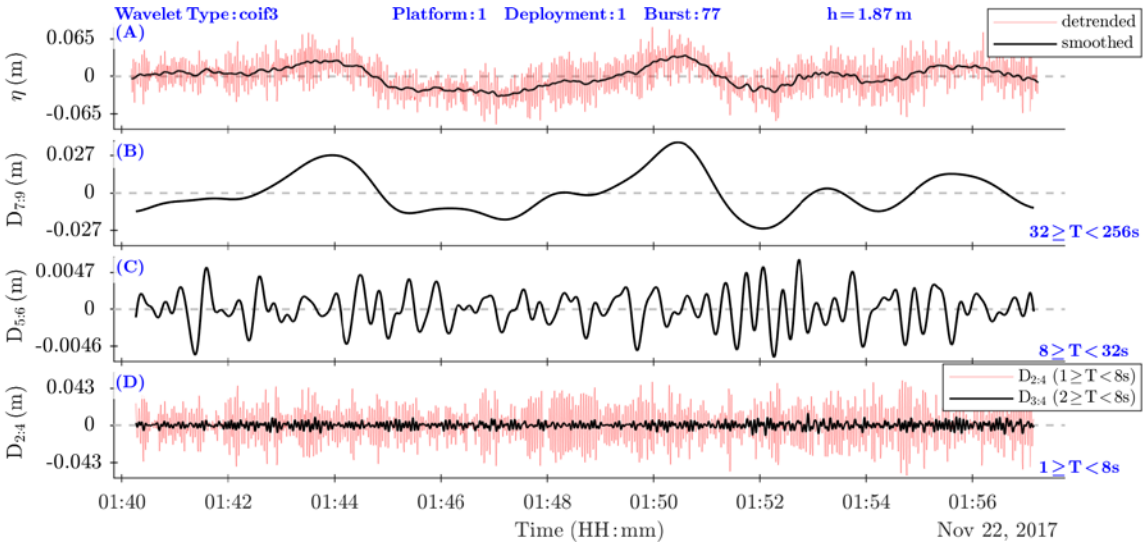

Fig. 29 – Example of decomposed signal regrouped into the 3 main frequency bins for a wakeless burst.

4.2.3 Burst Hydrodynamic Statistics

Figure 30 provides an example for the combined high and mid frequency bin (Fig. 28, panels D and C) discrepancies observed across 22 bursts (panel A) in the 4 statistical measures forming the first direct addition to the decision algorithm. The 4 statistical measures forming the first component of the decision algorithm and their respective equations are defined as:

1) The total magnitude change (Fig. 30, panels D and G) in the burst (21):

$$\Delta M_{x:y} = \max\left(D_{x:y}\right) - \min\left(D_{x:y}\right) \tag{21}$$

Wherein $\Delta M_{x:y}$ is the total change in magnitude of bin $D_{x:y}$, $D_{x:y}$ is the bin containing the combined frequencies *x:y*, and *x:y* are the lower and upper bound indexes of the included frequencies of the bin. For example, frequency bin $D_{3:4}$ is the combination of frequency bins 3 and 4 (Fig. 26, panels H and G; Fig. 28-29, panel D black line), forming the combined high frequency bin.

2) Maximum variance of a 12-second sliding window (Fig. 30, panels E and H) in the burst (22):

$$S^2{}_{x:y,max} = \max\left(\frac{1}{n-1}\sum_{i=t-12}^{t+12}(A_i - \mu)^2\right) \quad , \quad t = 1{:}N \tag{22}$$

Wherein $S^2{}_{x:y,max}$ is the maximum variance of a moving 12-second window centered about time index t, A_i is the vector of values from combined frequency bin $D_{x:y}$ corresponding to the 12-second window, μ is the sample mean of A_i, N is the total number of points in the burst (i.e., 2048), and n is the number of points contained in the 12-second window (i.e., 24 as the data was collected at a 2 Hz sampling rate).

3) The kurtosis (Fig. 30, panels F and I) of the complete burst (23):

$$K_{x:y} = \frac{1}{N\sigma^4}\sum_{i=1}^{N}(A_i - \mu)^4 \tag{23}$$

Wherein $K_{x:y}$, σ, and μ are the kurtosis, standard deviation, and mean of the combined frequency bin $D_{x:y}$, respectively. Kurtosis, a fourth moment of the data distribution, is a measure of how prone to outliers the distribution is. For a distribution that is defined by a discrete water surface elevation timeseries, outliers take the form of relatively large deviations from the mean surface level in the timeseries. The effects of VGW events (i.e., wherein waves of considerably larger wave heights arrive and then cease within a timespan of about 3 minutes) thus inject these surface elevation outliers into the data, and the outliers are reflected by larger kurtosis values calculated for the timeseries.

4) Bin energy as a fraction of the total energy (Fig. 30, panels B and C) in the burst (24):

$$e_j = \sum f_j(x)^2 \tag{24}$$

$$f_j(x) = \sum_{k=0}^{N-1} d_{j,k} * 2^{\left(-j/2\right)} * \Psi(2^{-j}x - k) \tag{25}$$

Wherein e_j is the summed energy for detail bin j, $f_j(x)$ is the detail vector for bin j, k is the sample index ranging from 0: N-1, N is the total sample size, $d_{j,k}$ is the detail coefficient for bin j at point k, and Ψ is the function of the wavelet defining the transform.

Bursts containing a VGW exhibit statistical responses that can reach over 20x larger than those of non-VGW bursts (Fig. 30). Thresholds that can demarcate definitive distinctions between bursts with and without VGW events on their own are still not possible for any statistical measure considered in (25-28), however. Comparing the minimum values of bursts with wakes (i.e., black and red markers in Fig. 30) and the maximum values of the wind-only bursts (i.e., blue markers in Fig. 30), several measures have instances of wind-only burst statistics close to or even surpassing those of bursts containing VGW events (Tables 10-11).

Table 10 – Comparing the 4 statistical measures in the combined high frequency bin using the minimum value for bursts with strong or weak wake events and the maximum value for bursts that are wind only.

Measure	Strong Wake	Weak Wake	Wind Only	Empirical Threshold
$\Delta M_{3:4}$	0.06	0.03	0.05	0.035
$S^2{}_{3:4,max}$	3.5e-4	7.7e-5	2.2e-4	1e-3
$K_{3:4}$	10.0	4.1	7.2	6
$\Sigma E_{3:4}/\Sigma E_{total}$	1.0	2.6	5.5	4

Table 11 – Comparing the 4 statistical measures in the combined mid frequency bin using the minimum value for bursts with strong or weak wake events and the maximum value for bursts that are wind only.

Measure	Strong Wake	Weak Wake	Wind Only	Empirical Threshold
$\Delta M_{5:6}$	0.09	0.04	0.02	0.1
$S^2{}_{5:6,max}$	8.4e-4	1.4e-4	6.1e-5	2e-3
$K_{5:6}$	7.4	7.8	4.5	8
$\Sigma E_{5:6}/\Sigma E_{total}$	1.3	1.4	2.6	2.7

To overcome the lack of a single statistical threshold that can definitively ascertain whether a burst contains a VGW event, an aggregation of the various measures across both high and mid combined frequency bins is necessary. The empirical thresholds set for each measure and combined frequency bin are listed in Tables 12-13, along with the mean value of bursts containing VGW and the maximum value of bursts containing wind only.

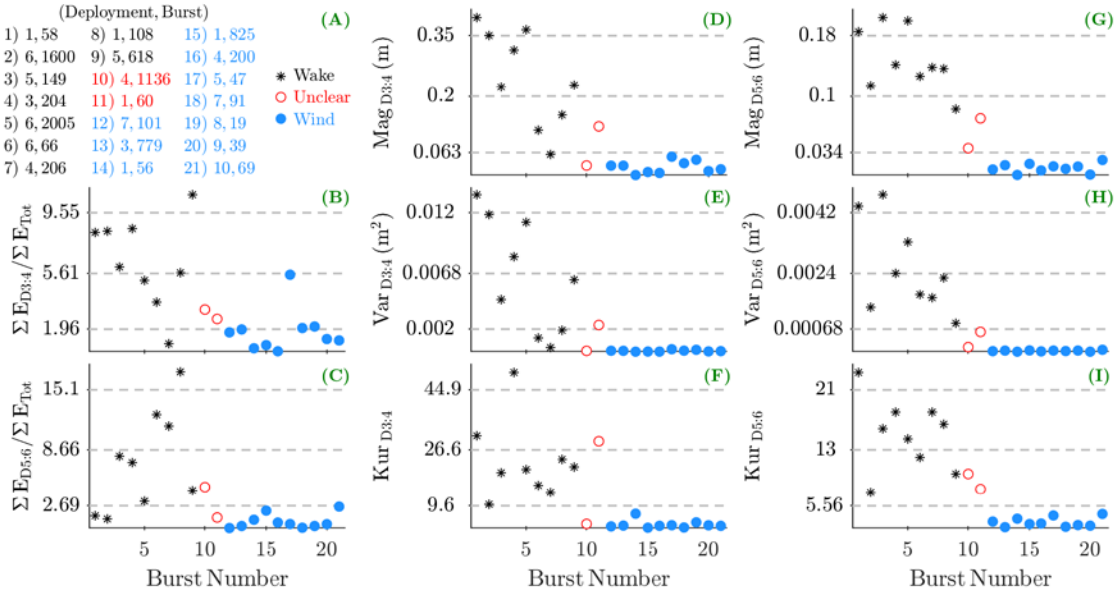

Fig. 30 – Statistical comparison of 10 bursts containing wake events (black), 10 wind-only bursts (blue), and 2 examples of bursts with unusually weak wake events (red). Summaries include total magnitude (panels D and G), maximum variance calculated from a 12-second moving window (E and H), kurtosis (F and I), and bin energies relative to the total energy of the entire signal (B and C).

Table 12 – Comparing the 4 statistical measures in the combined high frequency bin using the mean value for bursts with strong or weak wake events and the maximum value for bursts that are wind only.

Measure	Strong Wake	Weak Wake	Wind Only	Empirical Threshold
$\Delta M_{3:4}$	0.25	0.08	0.05	0.035
${S^2}_{3:4,max}$	6e-3	1.2e-3	2.2e-4	1e-3
$K_{3:4}$	22.9	16.7	7.2	6
$\Sigma E_{3:4}/\Sigma E_{total}$	6.4	2.9	5.5	4

Table 13 – Comparing the 4 statistical measures in the combined mid frequency bin using the mean value for bursts with strong or weak wake events and the maximum value for bursts that are wind only.

Measure	Strong Wake	Weak Wake	Wind Only	Empirical Threshold
$\Delta \boldsymbol{M}_{5:6}$	0.15	0.06	0.02	0.1
$\boldsymbol{S^2}_{5:6,max}$	2.5e-3	3.7e-4	6.1e-5	2e-3
$\boldsymbol{K}_{5:6}$	15.0	8.8	4.5	8
$\boldsymbol{\Sigma E}_{5:6}/\boldsymbol{\Sigma E}_{total}$	7.4	3.1	2.6	2.7

The requirement set for finalizing a burst as statistically indicating a VGW event or not was to search for at least 3 threshold exceedances across the magnitude, variance, and kurtosis related measures for both combined frequency bins. If 3 or more exceedances were found out of the possible 6, the burst was labeled as positive with strong confidence. If the burst only managed 1 or 2 exceedances, then the relative energy measure was additionally consulted. If both combined frequency bins contained an energy fraction above the corresponding threshold, the burst was then labeled as positive for a wake, except now with weak confidence. Any bursts not passing this weak confidence criteria (or having 0 exceedances across the magnitude, variance, and kurtosis measures) were assumed as not containing VGW events.

4.2.4 Mid Frequency Bin Alignments

The second direct addition to the decision chain, also utilizing the multiresolution decomposition, is perhaps the most critical as the output it provides is how the algorithm indexes potential wakes for inspection. When considering the effects of the dispersion relation from linear wave theory on a VGW packet containing a wide spectrum of periods, it should be expected that longer period waves arrive first, followed by arrivals in consecutive increases through the decomposed frequency bins (26):

$$\omega^2 = gk \sinh(kh) \tag{26}$$

$$\omega = \frac{2\pi}{T} \tag{27}$$

Wherein ω is the angular frequency of the wave.

The organization of the frequency bins in such a manner is highly unnatural, and therein presents the needed data point. Figure 31 illustrates this point, as the troughs of mid-range frequency bins align sequentially by bin upon the arrival of a wake. To first be considered, troughs must have a minimum relative prominence at least 5% of the most prominent trough in the corresponding bin. All troughs passing this initial threshold are then checked for alignment with the other bins; troughs are considered aligned if the 6th detail bin (D_6) arrives within 30 seconds after the 7th detail bin (D_7) and the 5th detail bin (D_5) arrives within 20 seconds after the D_6 bin. Beyond the 20 and 30 second arrival time thresholds, the exact time separating the trough arrivals between adjacent bins is not conditioned any further. This added flexibility is intended to increase the robustness of the analysis method as confirmed wake arrivals have been observed showing inconsistent separation durations between adjacent bins.

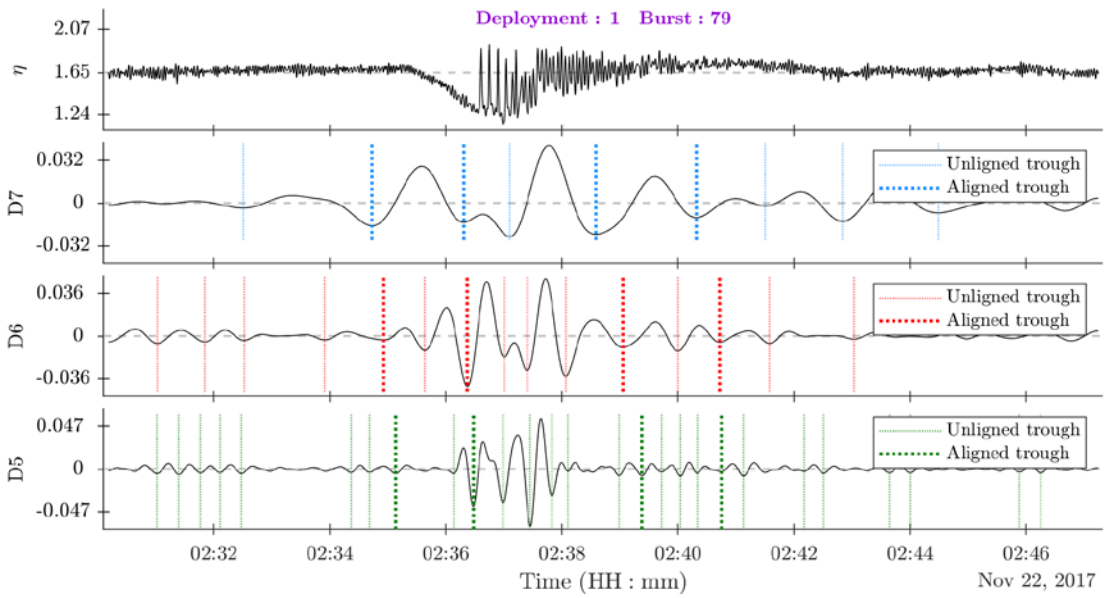

Fig. 31 – Alignments of the 5th, 6th, and 7th detail frequency bins for an arriving wake. Thin lines indicate troughs of at least 5% relative prominence, bold lines indicate trough alignments with potential linkage to a wake arrival event.

Trough alignments in the D_5-D_7 frequency bins are considered strong indicators of wakes due to the relative scarcity of naturally occurring waves in this mid frequency range. Enclosed bodies of

water such as GB are prone to low frequency motions known as seiches in addition to the standard high frequency wind-driven waves found in nearly all waterways, however very few natural bay processes will concentrate energy into the mid-range of the frequency spectrum. Once an alignment is positively identified, the point is saved according the arrival index of the D_6 trough.

4.2.5 High Frequency Bin Moving Variance

Continuing with the decomposed pressure signal, the third analysis method attempts to locate time indexes in the combined high frequency bin where abrupt changes in signal variance occur. Searching for these spikes in windowed variance is similar to how the moving variance statistic was used during the burst statistics considerations (26).

By running a moving 12-second window, enough time to capture 2 or 3 of the waves along the leading edge of a wake envelope, any wakes that include a high frequency component are rapidly identified. Identification occurs quantitatively by employing threshold up-crossings – as the 12-second windowed variance around a wake is often 50% greater than pre-wake arrival, whenever the mean value of the moving variance window throughout the entire burst is exceeded for more than 20 seconds, the event is recorded as a potential wake (Fig. 32).

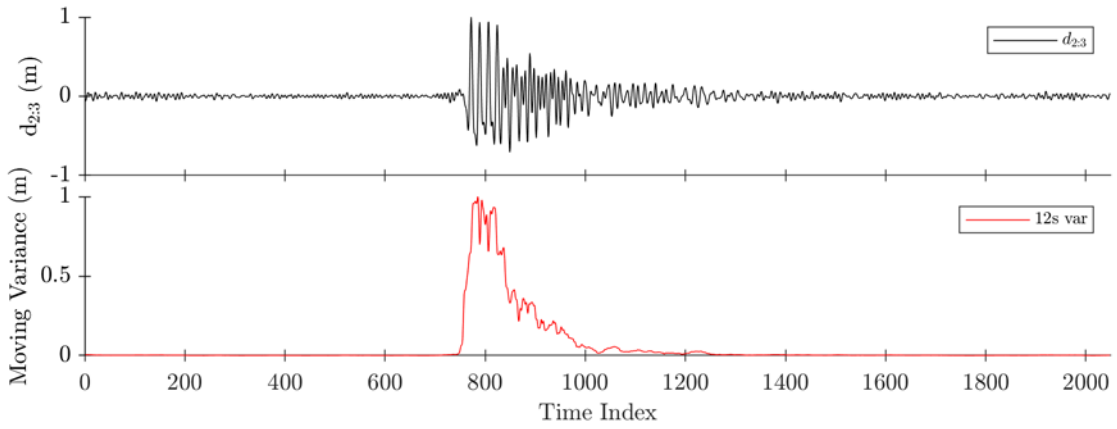

Fig. 32 – Comparing the high frequency bin with the value of a 12-second moving variance window

4.2.6 Windowed Max Displacement of Water Surface Elevations

Rather than using a short-windowed moving variance calculation similar to the high frequency bin, the fourth criterion added to the decision processes implements a longer sliding window over the smoothed pressure signal, now calculating the total magnitude change during a 90-second window (Fig. 33).

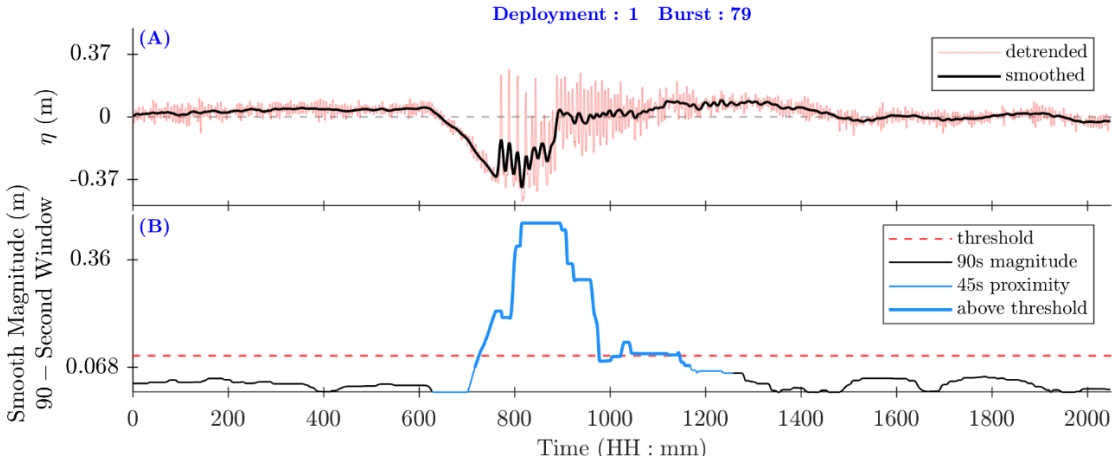

Fig. 33 – A detrended and smoothed pressure signal with a clear VGW arrival (panel A) that has undergone a 90-second moving window max magnitude threshold exceedance inspection (panel B).

By considering the total magnitude change anywhere within the 90 seconds, the goal was to allow for the entire bow component of the wake to be included. During those 90 seconds the extreme low of the drawdown contrasting with the corollary surge and arrival of the higher frequency components will typically distinguish this timepoint as a likely VGW event arrival. Additionally, choosing to run the window around the smoothed detrended pressure signal also serves to filter out most of the noise caused by background phenomena, further magnifying the relative strength of the actual VGW arrival event.

As with the moving variance of the high frequency bin (Fig. 32), a threshold exceedance inspection provides the quantitative means to declare the index as a valid wake. An empirical value of 0.07 m was found to successfully separate out VGW events from false positive events

that may have otherwise been identified. Due to wakes occasionally presenting highly irregular bow or stern components, likely due to phase issues in the propagating wave packets destructively interacting, it was found that extending the threshold exceedance indexes by 45 seconds out to each side of the exceedance span successfully overcomes any irregularities and provides the desired outcome. Because the algorithm considers output from this inspection as a vector of indexes above or within 45 seconds of an exceedance rather than requiring only the first up crossing index (as with the high frequency variance inspection), ensuring the bow component of the wake is included in the exceedance span prompted the need for a solution to irregular wake behavior.

4.2.7 Velocity Component Spanning

Wake arrival predictions dependent on cross shore (herein u) and alongshore (herein v) velocity components are far less reliable when compared to the associated pressure signal. Attempts of correlating peak or trough alignments in the smoothed u/v components would logically present a reasonable starting point, however irregularities in the velocity components across different wake events prevent dependence on this straightforward approach. To overcome these consistency issues, a robust approach was needed that could balance the need for identifying wake arrivals during high uncertainty events while also avoiding overly excessive false-positive predictions.

Rather than directly seeking peaks, troughs, or otherwise large magnitudes that may exist in the signals, the primary focus was instead shifted to extracting spans where the smoothed pressure and velocity components maintained relatively extended periods of unidirectional movement (i.e., long stretches of a positive or negative slope). Spans were first constructed using pairs of consecutive peaks and troughs as shown in Fig. 34, where green lines indicate positive slope spans and blue the negative slopes.

With the intention of avoiding repeated signal smoothing (and possible obfuscation of important details such as inflection, peak, or trough locations), the spans were instead merged, when necessary, via comparisons with adjacent spans in the opposite direction. Beginning with the last span index and iterating back towards the first index, spans in each slope direction for pressure and velocity components were tested via two possible merge conditions – conditions based on a 2- or 3-span series (Table 14). If the current index is index “x,” then span x-1 and x-2 would be the spans 1 and 2 indexes before the current index (all with the same slope direction as span x and all in the same component). As the minimum (i.e., first) index is 1, if there is a total of “n” spans for the given slope direction in the given component, the 2-span series could only merge indexes 2:n while the 3-span series could only merge indexes 3:n. The 3-span merge test was performed first and the 2-span test was only performed if the 3-span failed. If a 3-span test resulted in a successful merging, the next iteration index would jump forward by 2 to account for

the 2 earlier spans (i.e., x-2:x-1) that were merged with the current. Otherwise, the iteration index would move forward by 1 after 2-span merges or no merges by either test.

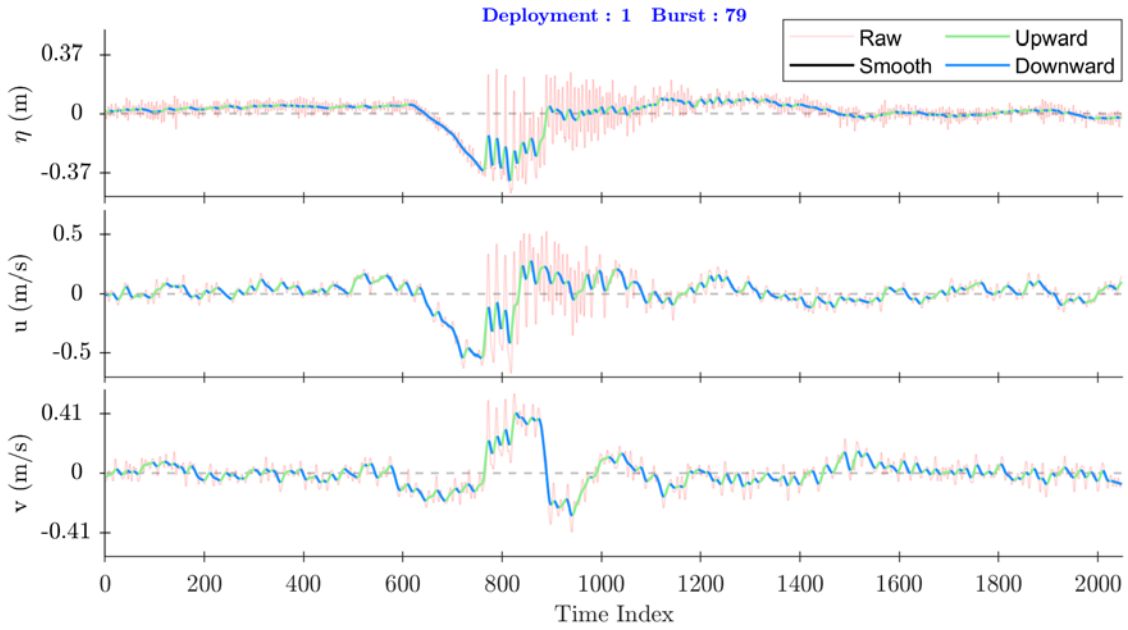

Fig. 34 – The start of the velocity span approach where upward moving spans are green and downward spans blue.

Table 14 – Description of the two conditional span tests used for merging in the pressure and velocity components.

Condition series	Indexes considered (x is current)	# of spans with matching slope considered	# of spans with opposite slope considered	Total # of spans to potentially merge as one
3-span	x-2:x	3	2	5
2-span	x-1:x	2	1	3

The specific conditions required for initial span merging by each test are as follows:

- 3-span test
  - Positive slope (x is span with index x, $start\ x$ is first magnitude in span x, etc.)
    - $Start\ x > start\ x - 2$
    - $Start\ x - 1 > start\ x - 2$
    - $End\ x > start\ x - 2$
    - $End\ x > start\ x - 1$
    - $Max\ relative\ magnitude\ of\ 2\ associated\ negative\ spans = 15\%$
      - Relative to magnitude of max negative span in the component
    - $Max\ duration\ of\ the\ two\ associated\ negative\ slope\ spans = 15\ seconds$
    - $\frac{\sum Increases\ in\ the\ 3\ positive\ spans}{\sum|Decreases\ in\ the\ 2\ associated\ negative\ spans|} > 3$
      - Ratio of gross change
    - $\frac{[Min(start\ x-1,\ start\ x)-(start\ x-2)] + [(end\ x)-Max(end\ x-2,\ end\ x-1)]}{Max(end\ x-2,\ end\ x-1)-Min(start\ x-1,\ start\ x)} > 2.5$
      - Ratio of net change

  - Negative slope (x is span with index x, $start\ x$ is first magnitude in span x, etc.)
    - $Start\ x < start\ x - 2$
    - $Start\ x - 1 < start\ x - 2$
    - $End\ x < start\ x - 2$
    - $End\ x < start\ x - 1$
    - $Max\ relative\ magnitude\ of\ 2\ associated\ positive\ spans = 15\%$
      - Relative to magnitude of max positive span in the component
    - $Max\ duration\ of\ the\ two\ associated\ positive\ slope\ spans = 15\ seconds$
    - $\frac{\sum|Decreases\ in\ the\ 3\ negative\ spans|}{\sum Increases\ in\ the\ 2\ associated\ positive\ spans} > 3$
      - Ratio of gross change
    - $\frac{[(start\ x-2)-Max(start\ x-1,\ start\ x)] + [Min(end\ x-2,\ end\ x-1)-(end\ x)]}{Max(start\ x-1,\ start\ x)-Min(end\ x-2,\ end\ x-1)} > 2.5$
      - Ratio of net change

- 2-span test
  - Positive slope (x is span with index x, $start\ x$ is first magnitude in span x, etc.)
    - $Start\ x > start\ x - 1$
    - $End\ x > start\ x - 1$
    - $Max\ relative\ magnitude\ of\ the\ associated\ negative\ slope\ span = 15\%$
      - Relative to magnitude of max negative span in the component
    - $Duration\ of\ the\ associated\ negative\ slope\ span = 15\ seconds$
    - $\frac{\sum Increases\ in\ the\ 2\ positive\ spans}{|Decrease\ in\ the\ associated\ negative\ span|} > 3$

    - Ratio of gross change
  - $\frac{(start\ x - start\ x{-}1) + (end\ x - end\ x{-}1)}{(end\ x{-}1) - (start\ x)} > 2.5$
    - Ratio of net change

- Negative slope (x is span with index x, $start\ x$ is first magnitude in span x, etc.)
  - $Start\ x < start\ x - 1$
  - $End\ x < start\ x - 1$
  - $Max\ relative\ magnitude\ of\ the\ associated\ positive\ slope\ span = 15\%$
    - Relative to magnitude of max positive span in the component
  - $Max\ duration\ of\ the\ associated\ positive\ slope\ span = 15\ seconds$
  - $\frac{\sum |Decreases\ in\ the\ 2\ negative\ spans|}{Increase\ in\ the\ associated\ positive\ span} > 3$
    - Ratio of gross change
  - $\frac{(start\ x{-}1 - start\ x) + (end\ x{-}1 - end\ x)}{(start\ x) - (end\ x{-}1)} > 2.5$
    - Ratio of net change

The relative magnitudes of each span were updated following the primary merging processes, and then a series of 6 secondary merging and trimming operations were performed in the following order:

<u>For all pressure and velocity components</u>

1) $Trim\ spans\ with\ magnitudes\ under\ 15\%\ the\ \max\ magnitude\ in\ the\ given\ slope\ direction$
2) $Merge\ 2\ adjacent\ spans\ of\ same\ slope\ direction\ if$:
   - $separated\ by\ 15\ seconds\ or\ less$
   - $there\ is\ not\ a\ span\ of\ either\ slope\ direction\ between\ them$
3) $Merge\ 2\ adjacent\ spans\ of\ opposite\ slope\ direction\ at\ the\ seperation\ midpoint\ if$:
   - $separated\ by\ 25\ seconds\ or\ less$
   - $there\ is\ not\ a\ span\ of\ either\ slope\ direction\ between\ them$

<u>For pressure component only</u>

4) $Trim\ spans\ of\ each\ slope\ direction\ with\ relative\ slopes\ less\ than\ 20\%$
   - Relative to the maximum span slope of the given span slope direction
5) $Trim\ spans\ of\ positive\ slope\ direction\ with\ durations\ longer\ than\ 90\ seconds$
   - As only spans associated with VGW events are desired, pressure spans with positive slopes lasting longer than the maximum expected duration of post-

drawdown surges (about 90 seconds) can be removed from further considerations

- As drawdown durations are highly variant relative to expected post-drawdown surges, only the positive slope directions were considered for this trimming procedure

For all pressure and velocity components

6) *Trim spans of either slope direction unconnected to a span of opposite slope direction*
    - Connections defined as spans of a given pressure or velocity component and a given slope direction having a shared start or end point with a span of the opposite slope direction

With the span merging and trimming procedure complete, a list of span connection points in the u/v velocity components was next determined. Table 15 lists the connection types for wake events in each direction. The connections are noted as only considering the bow portion of an event due to the bow portion of a wake providing the greatest discrepancy between inbound and outbound wake events. This discrepancy is a function of how closely the respective u/v span connection points are aligned (bow portions are typically closer) and how strong the magnitudes of the u/v span connection points are (bow portions are typically larger). The clearer discrepancy is a result of the bow portion arriving during relatively quiescent hydrodynamic activity while the stern portion arrives as remnants of the bow portion are still present (Table 15).

Table 15 – Velocity component span connection details for the bow portion of wake events in each transit direction.

Vessel heading	Slopes of connecting spans at bow		Connection type at bow	
	u	v	u	v
Inbound	Positive-Negative	Positive-Negative	Peak	Peak
Outbound	Positive-Negative	Negative-Positive	Peak	Trough

The next step of the velocity inspection begins by indexing each span connection occurrence (i.e., a pseudo peak or trough point). Valid u/v connection indexes must meet the following criteria:

- u component peak connections:
    - $have\ a\ shared\ point\ between\ positive\ span\ ends\ and\ negative\ span\ starts$
    - $have\ a\ positive\ slope\ component\ at\ least\ 10\ seconds\ in\ duration$
    - $have\ a\ positive\ slope\ component\ with\ a\ relative\ magnitude\ of\ at\ least\ 20\%$
- Only 1 of the last 2 conditions is required for index validation
- v component peak connections:
    - $have\ a\ shared\ point\ between\ positive\ span\ ends\ and\ negative\ span\ starts$
- v component trough connections:
    - $have\ a\ shared\ point\ between\ negative\ span\ ends\ and\ positive\ span\ starts$

As VGW event arrivals are expected to exhibit aligned u/v connections (i.e., peaks or troughs in the u and v velocity components that occur simultaneously), connections of a given smoothed velocity component without a corresponding connection in the other smoothed velocity component may be trimmed from consideration. For this alignment-based trimming to succeed, the location of the peak/trough connection indexes must accurately reflect the true location of peaks/troughs in the smoothed velocity component. Accurate representations of the true locations for the peak/trough are generally observed, however bursts containing velocity components that resemble a plateau after signal smoothing are not uncommon (Fig. 35, panel B). Plateaus in the smoothed signal occur when velocity components do not exhibit the greatest magnitudes at the start of the bow/stern portions with the magnitudes then decreasing with time. Because the largest wake waves, and by extension the largest velocity component magnitudes, are expected to arrive at the onset of the bow/stern portions (Fig. 3), instances of maximum magnitudes found later than expected indicate an irregularity with the recorded component signal. The main instigators of such irregularities are attributable to:

- hydrodynamic interferences superimposing with the wake event and thereby altering the wake's true signal (i.e., interference resulting from the arrival of a different wake event);
- bow and stern wake components that are out of phase and thus dampen during interactions;
- coincidental Doppler effect undermeasuring during the initial waves of the bow/stern portion;
- the sampling frequency is low enough to where the component magnitudes for some waves were not accurately measured after peak values occurred between successive ADCP measurements;

- wave reflections at the dike embankment spawn standing wave interferences.

Considering the above possibilities, the most likely cause of smoothed signal component plateaus is likely due to dampening interactions by out of phase bow and stern wake components whenever superimposing or standing wave interferences are not present. As the ADCP wave burst mode used in data collection had a sampling frequency of 2 Hz, the sampling frequency may have slightly magnified the irregularity, but was likely not the sole cause. Because occurrences of signal plateaus effectively shift the location of the peak/trough span connection away from its true location as noted earlier, corrections are therefore necessary.

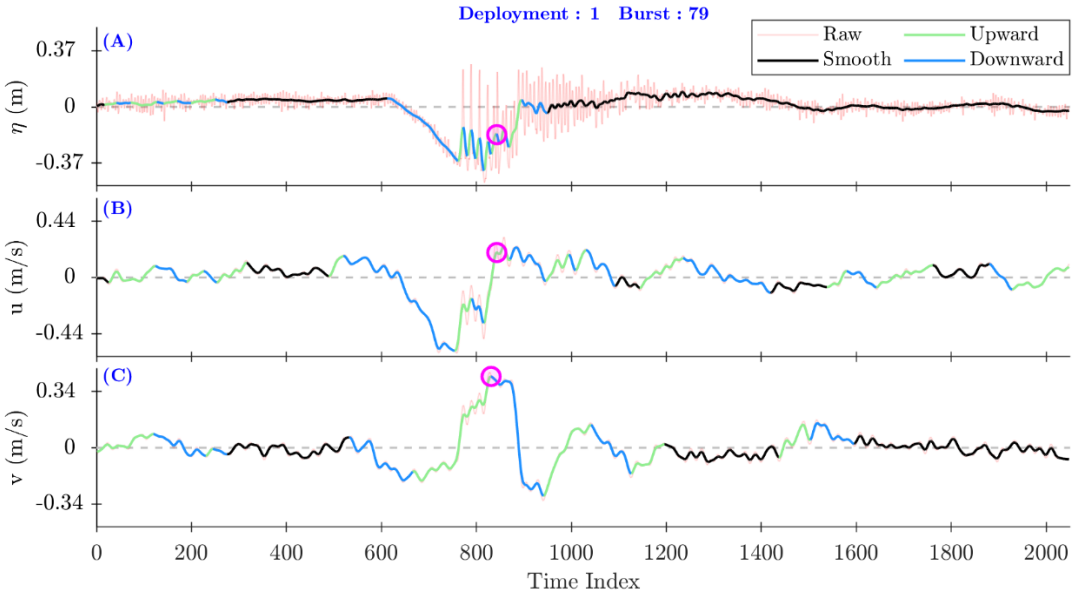

Fig. 35 – Outcome of the span merging and trimming process designed to identify periods of extended unidirectional velocity behavior. The connection point identified in the u component is noted as having been shifted slightly backward during corrective analysis after initially appearing later than expected. The shift is observed by the mid-span location of the u component connection point (circled) instead of an end of span location as would normally be expected. The correction positions the u and v component connections within the necessary proximity to be considered a potential wake; the wake passes the inspection.

When plateaus in the slope of the smoothed velocity component are identified, the point is continually shifted backward each previous wave having a magnitude similar to that of the current wave. Shifts will begin with the last wave index of the corresponding smoothed velocity component span (i.e., at the location of the wave with peak magnitude during the span) and move earlier towards the middle of the span (Fig. 35, panel B). Steps for determining whether to shift a connection point index backward are:

1) $Isolate\ the\ waves\ contained\ in\ the\ smoothed\ velocity\ component\ signal\ span$
2) $Normalize\ peak\ wave\ magnitudes\ with\ respect\ to\ the\ \max magnitude\ during\ the\ span$
3) $Shift\ the\ connection\ point\ back\ to\ the\ peak\ magnitude\ of\ the\ previous\ wave\ while\ the$:
    - $magnitude\ of\ the\ previous\ wave\ is\ within\ 40\%\ of\ the\ peak\ magnitude$
    - $normalized\ magnitude\ change\ from\ the\ current\ to\ previous\ wave\ is\ < 25\%$

A change in smoothed velocity component wave magnitudes that fails either of the 2 conditions in the 3rd step (above) indicates the next wave is no longer part of the wake packet. The process of active index correction is a direct response for needing to overcome a velocity component signal irregularity that could otherwise derail positive identification.

Following the connection index shift corrections (if any were necessary), a sorting process then ensures only valid connection indexes that correspond to a connection index in the opposite velocity component are kept. The sorting is completed by ensuring:

- $Connection\ indexes\ in\ one\ component\ correspond\ to\ connection\ in\ the\ other\ component$
    - Wake events will reach peak magnitudes in each velocity component within relatively close proximity (about 20 seconds at most, usually less than 10 seconds)
- $Connection\ indexes\ must\ align\ within\ 30\ seconds\ of\ a\ pressure\ span\ starting\ index$
    - VGW events observable in the velocity components will be observable in the pressure
- $Only\ 1\ vessel\ per\ each\ transit\ direction\ can\ exist\ within\ a\ 3-minute\ span$
    - Vessel traffic in the HSC is spaced to avoid vessels overtaking one another

Any velocity connection indexes remaining after the corrective procedures are completed are then passed along to the decision algorithm as potential VGW arrival times.

4.2.8 Decision Synthesis

On completion of each of the 5 data analysis methods discussed in sections *4.2.3*-4*.2.7*, results were fed back into the main algorithm that then initiated the synthesis of a final decision for conclusive wake identifications.

At this stage comes the first reference to the AIS records; up until now the decision chain has solely relied on measured hydrodynamic data. Vessel records timestamped between the starting and ending time index of the given ADCP burst are identified and sorted by ship MMSI into transit lists. MMSI, or Maritime Mobile Service Identity, is the internationally recognized unique identification number given to each vessel. Each transit has the heading direction gauged by general direction of travel, and with this heading, an initial prediction is made of when the vessel's wake should manifest in the ADCP measured data. This timing prediction is created by interpolating the known path of the vessel and using the interpolation to estimate when a specific latitude threshold is reached. Although a (heading-specific) fixed point is used, predictions tend to be within 5 minutes or less regardless of ship type or speed.

As was briefly mentioned in section *4.2.1.*, this approach of using latitude-based interpolation for predicting arrival times for any given wake event had the undesirable drawback of occasionally failing to correlate a wake event with the corresponding vessel. The failures would occur due to 2 potential causes:

- the vessel had unusually long gaps between successive position recordings, causing large errors in the interpolation, and/or
- the wake event arrived near the start or end of a burst, leading to interpolations with a relatively large error margin resulting in predictions shifted to the burst immediately before or after the actual burst.

Identification begins via looping through each mid frequency alignment index (section *4.2.4*). The mid frequency alignment indexes are noted as composing the "anchor" data points that guide the decision algorithm's iterations as an acknowledgement that these alignments provide the only fundamental behavior observed to occur universally across the full spectrum of wake events. A series of attempts are then made by the algorithm to find the best matches, if any exist, from results of the various analysis methods (including AIS-generated predictions) for each alignment index. The algorithm is designed to allow results from each method to be used only once, namely by the optimally matching alignment index.

Any disagreements between data sources are found and addressed, such as AIS headings not matching the heading predicted by the velocity span method or the AIS time prediction poorly matching the other method prediction indexes (i.e., the predictions are off by more than 5 minutes). Any disagreements not resolved are then designated and set aside. Disagreements are not simply tossed to ensure wakes unable to attain positive identification are still recognized as potential events, thereby avoiding erroneously identifying 2 interfering VGW events as 1 event. These lingering disagreements may result in the over exclusion of some VGW events that truly are just a single vessel after registering possible interference with a false-positive event (i.e., the disagreeing index). Considering the data collection period lasted for nearly a year, however, the final sample size should still contain enough VGW events to where the erroneously excluded events do not impact the fidelity of conclusions made during final analysis.

A final verdict is rendered by the algorithm on the basis of how complete the agreement is between each analysis method, whether the wake was likely to have experienced truncation after arriving too close to the start or end of a burst, and whether the wake likely experienced interference from the wake of a different ship after crossing paths near the site. For a VGW event to be used in analysis, the verdict must:

- Have full agreement across all inspection methods (sections 4.2.3 – 4.2.7);
- Recognize an AIS record corresponding to the VGW event that:
    - Results in an event arrival time prediction within 5 minutes;
    - Does not have any key vessel specification information missing;
- Indicate that the entirety of the wake occurred within the bounds of an ADCP burst;
- Indicate no interference occurred between the VGW event and an event from another vessel.

4.3 Vessel Transit Inventory

An inventory of vessel transits through the study site was assembled using the following steps:

1) Compiling a list of vessel MMSI numbers from the AIS database.
2) Extracting all records for each unique MMSI.
3) Partitioning the list of records into isolated transits.
    - Transits were isolated by sorting the single-ship records via timestamps and searching for instances of timestamps having more than a 30-minute difference from the record immediately prior.
    - A duration of 30 minutes was used since this stretch of time was both too long to be part of the previous transit yet short enough to where an inbound ship making a quick port call and immediately sailing outbound would not register as a single transit.
4) Determine the likeliest ADCP burst to contain each transit by matching the timestamp of the record with a latitude coordinate closest to that of platform Simon to the burst containing (or nearest to) that timestamp.
    - The vessel latitude is used as a proxy for estimating when the wake should approximately arrive at the platform.
5) Search the likeliest burst and the bursts immediately before and after for wake events identified by the algorithm with a heading matching the heading indicated by the AIS records.
    - If multiple possibilities are located then the wake event nearest in time to the latitude-based timestamp identified in step 4 is selected.
    - The bursts immediately before and after the likeliest are also searched in case the wake event arrives between bursts or the latitude-based timestamp has a large margin of error in estimating when the wake arrives.

4.4 Vessel AIS and Wake Event Correlations

Each attempted correlation between vessel characteristics and the corresponding wake events is presented with a regression equation and R^2 correlation value. Regressions were performed using 3 different curve equations – a 1st degree power function (28a), a 1st degree polynomial function (28b), and a 1st degree exponential function (28c):

$$y = ax^b \tag{28a}$$

$$y = ax + b \tag{28b}$$

$$y = ae^{bx} \tag{28c}$$

Each of the 3 curve equations were fitted to 3 different bins of data, with data bins grouped by water depth (i.e., low, mid, and high tide depths). The depth bins were established by calculating a single water surface elevation value for each burst via taking the median pressure value from the burst. To convert water surface elevations into total depth, bursts occurring before construction of the beneficial-use embankment (i.e., prior to February 5th) had their surface elevations increased by 0.4 m, or the distance between the bed level and the mounted ADCP. Following the embankment construction (i.e., after February 5th), the water surface elevations were assumed to be the full depth value as the post-dredging bed level was raised to the base of the mounted ADCP. The data was grouped into the 3 depth bins to check how (or if) water depth modulated the correlations.

The depth ranges defining each bin were determined by compiling depths from all valid bursts (i.e., all bursts excluding those from deployments 2, 7, and the first half of 8) and finding the 33rd and 66th percentile values. Low tide depths were defined by the bottom third of values, mid tide depths by the mid third, and high tide depths by the top third. After each of the 3 regression curves were calculated for each of the 3 depth bins, whichever curve provided the maximum R^2 value across all of the depths was used for the entire correlation. In other words, 9 different R^2 values (3 curves for each of the 3 different bins) were calculated for each correlation, and the curve responsible for the maximum R^2 value from the 9 calculated was used for all 3 depths.

A notable caveat to the vessel specification information is the lack of in-situ vessel displacement values in the provided AIS data. Given the choice between neglecting VGW event and vessel displacement correlations or using the unloaded displacement values found in publicly available AIS databases, the decision was made to assemble as many unloaded displacement records as possible. Any resulting displacement correlations will thus contain an error source not found in

the remaining correlations, considering these records reflect the vessel displacement prior to loading and not the displacement during the specific transit. This added margin of error is assumed due to the fact that companies tend to avoid sailing unloaded vessels for maximum profits.

5.0 Results and Discussion

Vessel specifications correlated to VGW events are as provided by the USCG; any specification data not contained in the USCG dataset, including all displacement values, were pulled from websites hosting publicly accessible AIS information [MarineTraffic, 2020; VesselFinder, 2020]. Results of the VGW event identification algorithm are first summarized so the inventory of confirmed wake events can be established. Two wakes, one from each heading direction, are next presented to highlight the hydrodynamic differences resulting from either event. Each of the 2 research questions are then addressed preliminarily using analysis results from the VGW event subset.

5.1 Wake Identification Algorithm

5.1.1 Algorithm Performance

Figure 36 summarizes the results of the vessel transit inventory procedure discussed in section *4.2.9.* Table 16 provides further relevant details for each transit result classification found in Fig. 36. Of the 12,183 transits isolated in the AIS data during the period of data collection:

- 2,348 (19%) were translated by the algorithm into usable analysis events;
- 3,453 (29%) were generally identified by the algorithm, however whether due to arrival misidentification, interference, or the event having only partial measurements due to burst recording cutoffs (Table 16);
- 2,202 (18%) were completely missed by the algorithm;
- 4,108 (34%) were missed due to an offsite ADCP or occurring during a burst of unusable ADCP data;
- Event classification totals were essentially evenly split between transit heading directions.

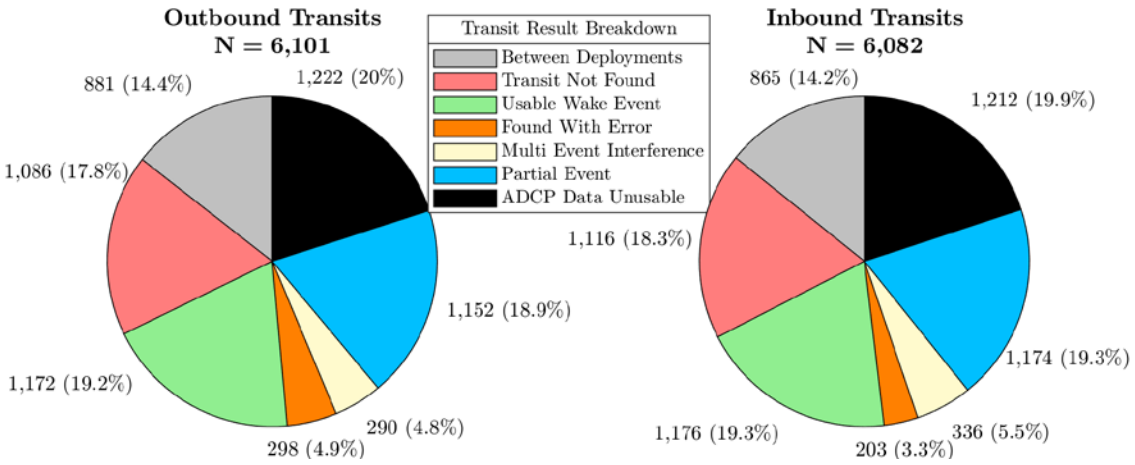

Fig. 36 – Breakdown of wake identification algorithm results.

Table 16 – Notable details for the potential transit classifications found in Fig. 36

Result	Notes
Between deployments	The transit occurred while ADCP instruments were offsite for period maintenance.
Transit not found	The transit was identified in the AIS data but not in the ADCP data. Wake events were missed due to the event having imperceptible hydrodynamic effects or obfuscation by interference from another wake (i.e., wakes from transits in both directions arrive simultaneously and the algorithm only identified a single wake start).
Usable wake event	-
Found with error	The algorithm identified the wake event but erroneously determined the exact starting time of the wake arrival. Such errors could occur during unfavorable meteorological conditions, if wakes events provided weak hydrodynamic signatures (i.e., smaller vessels), or wake events exhibited atypical hydrodynamic behavior on arrival.
Multi event interference	The algorithm correctly detected the wake event, however a wake event from a transit in the opposite direction was either also detected at some point before the event ended or was still ongoing when the current wake event began.
Partial event	A portion of the wake event was detected but the wake either arrived before the burst began or was unable to finish before the burst ended.
ADCP data unusable	The transit occurred during a burst that was tossed due to QA/QC or excluded from analyses after comparisons to the NOAA tidal record.

5.1.2 General Discussion

Of the 8,003 transits occurring during bursts of valid ADCP data, roughly 75% were at least partially identified by the algorithm. From the approximately 25% of transits remaining, it is unclear exactly how many were missed by outright failure by the algorithm due to a large fraction of the missed wakes having arrived in the roughly 3 minutes between bursts where the ADCP was inactive. The main areas where the algorithm performance efficiency could be further optimized is in the 501 transits (roughly 4%) where identification generally occurred but the exact arrival point was incorrect, and in the fraction of the 25% of missed transits that arrived mid-burst and should have received identification. In reality, the number of transits missed due to outright failure is certainly lower than the 2,202 listed, considering a non-negligible number of two superimposing wakes resulted in only a single identification (i.e., only 1 “multi wake interference” classification instead of what should have been 2).

5.2 Wake Hydrodynamics of the Two Transit Directions

5.2.1 Inbound

An isolated inbound wake event from the cargo vessel *EMS TRADER* (200 m length, 30 m breadth, 7.7 m draft) is observed between about 19:13-19:17 in Fig. 37. The wind-driven hydrodynamics, provided for perspective in Fig. 38, are from the timespan between about 19:22-19:26, well after the wake event had subsided and the site had returned to quiescent conditions.

Figure 38 illustrates the contrasting current velocity directions and magnitudes observed at the site during and after the inbound wake event recorded in Fig. 37. Tables 17-18 summarize key hydrodynamic statistics from each of the velocity bins in Fig. 38. Just under 50% of the quiescent current direction measurements were between 140-230°, indicating the background current direction to be roughly parallel with the shoreline (i.e., 210°) and flowing towards the HSC.

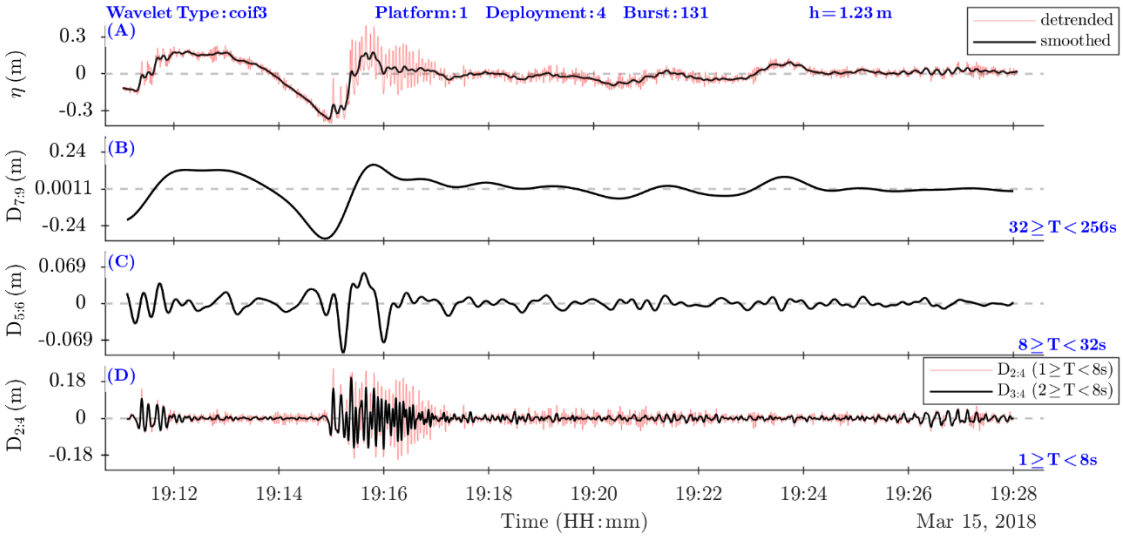

Fig. 37 – Multiresolution analysis of a burst with an inbound wake event from cargo ship EMS Trader between 19:13-19:17. For the comparison to quiescent conditions found in Fig. 38, a comparable timespan between 19:22-19:26 was selected.

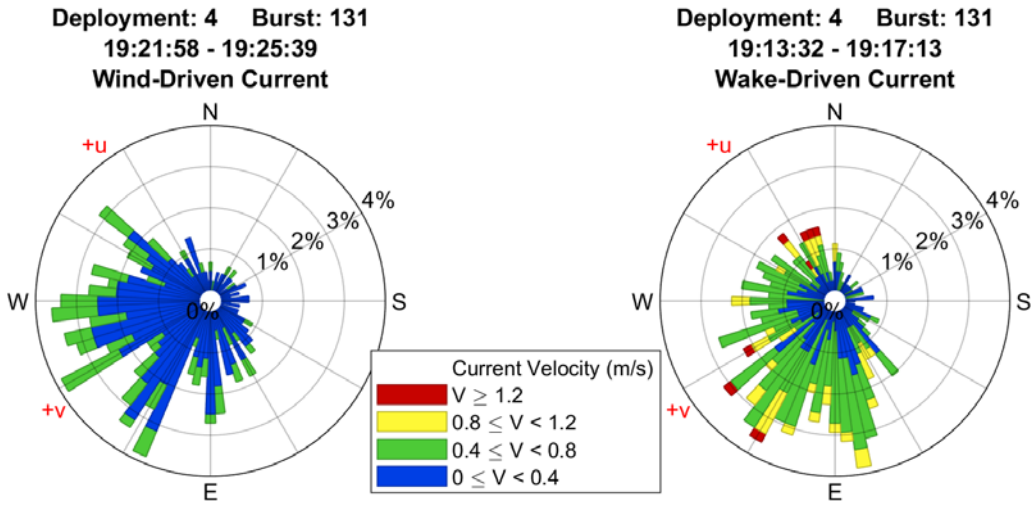

Fig. 38 – Wind rose styled plots of the quiescent wind-driven current (left) compared to the current resulting from an inbound wake event (right). Both hydrodynamic periods were recorded in the same 17-minute burst of ADCP data.

Table 17 – Calculated hydrodynamic statistics during and after an inbound wake event.

	Velocity (m/s)			Direction (°)			
Current Driver	Max	Mean	Std. Dev.	At Max Vel	Mean	Std. Dev	Mode
Wind	0.79	0.29	0.15	277.6	201.5	72.8	210
Inbound VGW	1.65	0.5	0.27	109.8	212.5	74.7	280
Difference	**0.86**	**0.21**	**0.12**	**-167.8**	**11.0**	**1.9**	**70**

Note - In the "Difference" row (row 4), positive velocity values (columns 2-4) indicate a greater inbound VGW event-driven current value while negative values indicate a greater wind-driven current value.

Table 18 – Calculated hydrodynamic statistics during and after an inbound wake event.

Current	Frequency (%) per Velocity (m/s) Bin				Mean Direction (°) per Velocity (m/s) Bin			
Driver	V<0.4	0.4≤V<0.8	0.8≤V<1.2	V≥1.2	V<0.4	0.4≤V<0.8	0.8≤V<1.2	V≥1.2
Wind	78.3	21.7	0	0	201.8	200.5	-	-
Inbound VGW	37.9	50.6	9.7	1.8	209.7	216.5	212.9	157
Difference	**-40.4**	**28.9**	**9.7**	**1.8**	**7.9**	**16.0**	**-**	**-**

Note - In the "Difference" row (row 4), positive frequency values (columns 2-5) indicate a greater frequency in the inbound VGW event-driven current while negative values indicate a greater frequency in the wind-driven current.

A considerable strengthening in current velocity is clearly observed during the wake event, as well as a slight coincident shift in mean current directions. When split into the draw down (i.e., partial low-frequency Bernoulli wave) and surface waves (i.e., high-frequency Havelock waves) components, the inbound VGW-driven current is observed to actually consist of 2 distinct, time-dependent behaviors (Fig. 39, Tables 19-20). Splitting the wake event (Fig. 38, right panel) into the separate components thus allows for higher resolution comparisons to be made, both when comparing the wake event with quiescent conditions and when contrasting the 2 different wake component behaviors against each other.

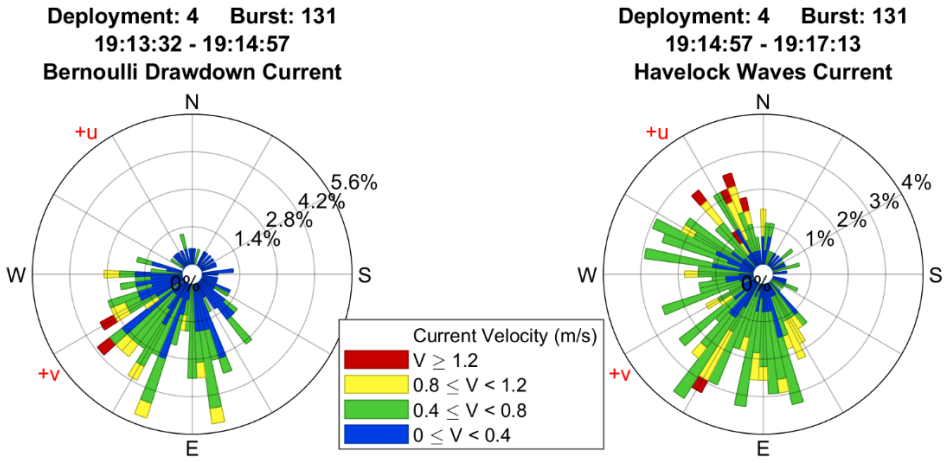

Fig. 39 – Wind rose styled plots of the current during the two main wake components, the low-frequency Bernoulli wave drawdown (left) and the high-frequency Havelock surface wave packet (right).

Table 19 – Calculated hydrodynamic statistics during the low frequency drawdown and high frequency surface wave components of the inbound wake event.

	Velocity (m/s)			Direction (°)			
Current Driver	Max	Mean	Std. Dev.	At Max Vel	Mean	Std. Dev	Mode
Wind	0.79	0.29	0.15	277.6	201.5	72.8	210
Drawdown	1.23	0.42	0.25	217.7	230.2	70.8	250
Difference	**0.44**	**0.13**	**0.1**	**-59.9**	**28.7**	**-2.0**	**40**
Surface Waves	1.65	0.56	0.27	109.8	201.5	75.0	235
Difference	**0.86**	**0.27**	**0.12**	**-167.8**	**0**	**2.2**	**25**

Note - In the "Difference" rows (row 4 & 6), positive values (columns 2-4) indicate a greater inbound VGW event-driven current component value while negative values indicate a greater wind-driven current value. Each component "Difference" row is relative to the quiescent, wind-driven conditions.

Table 20 – Calculated hydrodynamic statistics after the inbound wake event, during the low frequency drawdown inbound wake component, and during the high frequency surface wave inbound wake component.

Current Driver	Frequency (%) per Velocity (m/s) Bin				Mean Direction (°) per Velocity (m/s) Bin			
	V<0.4	0.4≤V<0.8	0.8≤V<1.2	V≥1.2	V<0.4	0.4≤V<0.8	0.8≤V<1.2	V≥1.2
Wind	78.3	21.7	0	0	201.8	200.5	-	-
Drawdown	53.8	38.6	6.4	1.2	223.5	239.5	233.5	214.0
Difference	**-24.5**	**16.9**	**6.4**	**1.2**	**21.7**	**39.0**	**-**	**-**
Surface Waves	27.8	58.2	11.7	2.2	193.1	207.0	205.8	138
Difference	**-50.5**	**36.5**	**11.7**	**2.2**	**-8.7**	**6.5**	**-**	**-**

Note - In the "Difference" rows (row 4 & 6), positive velocity frequency values (columns 2-5) indicate a greater frequency in the inbound VGW event-driven current component while negative values indicate a greater frequency in the wind-driven current. Each component "Difference" row is relative to the quiescent, wind-driven conditions.

Both the drawdown and surface wave phases of an inbound VGW event have considerably different current velocity magnitudes relative to quiescent conditions, and to a lesser extent between themselves:

- The maximum and mean current velocities (Table 19) are roughly:
  - 50% stronger than quiescent magnitudes during the drawdown phase.
  - 100% stronger than quiescent magnitudes during the surface wave phase.
- The proportion of current velocities under 0.4 m/s present clear contrasts (Table 20), as the fraction of magnitudes below 0.4 m/s compose:
  - 78% of the quiescent period.
  - 54% of the drawdown phase.
  - 28% of the surface waves phase.
- The surface waves create magnitudes at or above 0.8 m/s at a rate twice that of the drawdown (Table 16b), as approximately:
  - 7.5% of the 90-second drawdown is above 0.8 m/s.
  - 14% of the 135-second surface wave phase is above 0.8 m/s.

The greatest deviation from the quiescent current direction was during the surface wave phase, however this is partly due to the quiescent current flowing towards the HSC and thus coincidently matching the flow direction observed during the drawdown. As the drawdown is the result of water surface displacements emanating from the vessel, the current flow during this event will invariably concentrate in the direction of the HSC regardless of quiescent flow directions. Additional current direction results include:

- 49% of the quiescent current direction measurements were between 140-230°.
- 72% of the drawdown phase current direction measurements were between 180-300°.
- The current during the surface wave phase was split into 2 main oscillatory directional bins:
    - 34% between 90-180° (i.e., around the +u direction).
    - 46% between 210-300° (i.e., between +v and -u).
- The max cross-shore velocity magnitude, 1.65 m/s, was within 10° of shore-normal (i.e., +u) and occurred during the surface wave phase.
- The max alongshore velocity magnitude, 1.23 m/s, was within 8° of shore-parallel towards the HSC (i.e., +v) and occurred during the drawdown phase.

5.2.2 Outbound

An isolated outbound wake event from the tanker vessel *EVERGLADES* (250 m length, 44 m breadth, 8.4 m draft) is observed between about 16:33-16:38 in Fig. 40. The wind-driven hydrodynamics, provided for perspective in Fig. 41, are from the timespan between about 16:27-16:32, well before the wake event had started and while the site experienced quiescent conditions.

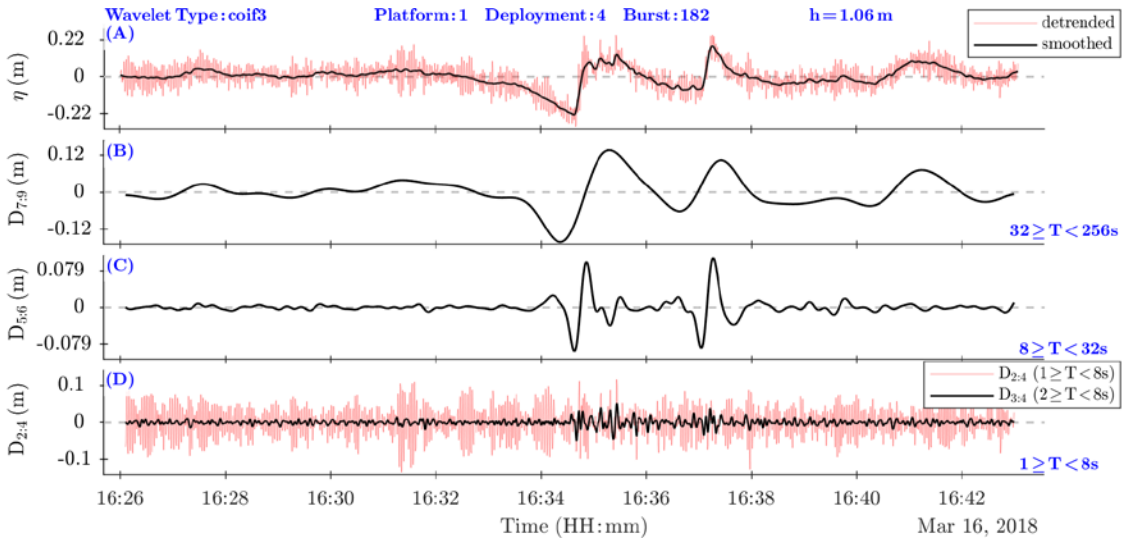

Fig. 40 - Multiresolution analysis of a burst with an outbound wake event from the tanker vessel EVERGLADES between 16:33-16:38. For the comparison to quiescent conditions found in Fig. 41, a comparable timespan between 16:27-16:32 was selected.

Figure 41 illustrates the contrasting current velocity directions and magnitudes observed at the site before and during the outbound wake event shown in Fig. 40. Tables 21-22 summarize key hydrodynamic statistics from each of the velocity bins in Fig. 41. Just under 40% of the quiescent current direction measurements were between 60-150°, indicating an onshore background current direction (i.e., 120°).

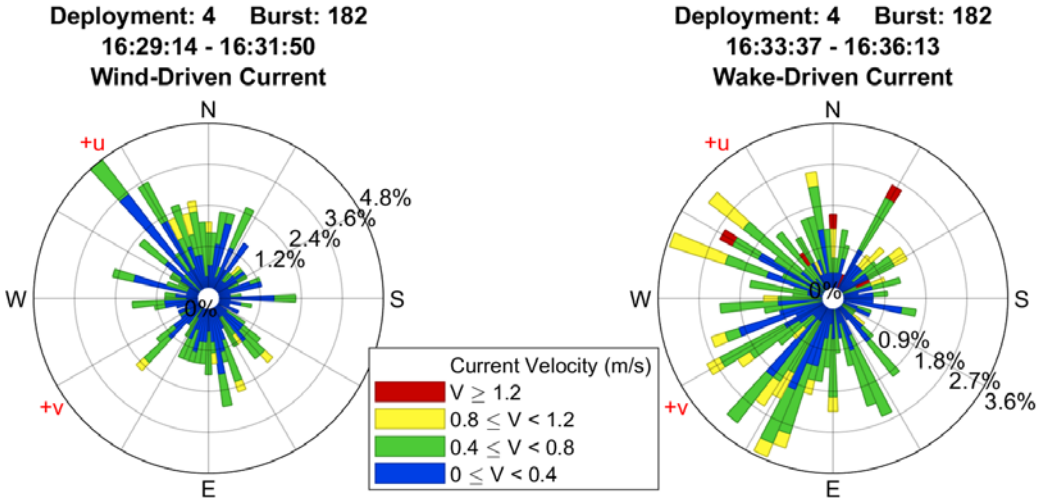

Fig. 41 – Wind rose styled plots of the quiescent wind-driven current (left) compared to the current resulting from an outbound wake event (right). Both hydrodynamic periods were recorded in the same 17-minute burst of ADCP data.

Table 21 – Calculated hydrodynamic statistics during and after an outbound wake event.

	Velocity (m/s)			Direction (°)			
Current Driver	Max	Mean	Std. Dev.	At Max Vel	Mean	Std. Dev	Mode
Wind	1.04	0.39	0.2	114.1	175.8	96.8	130
Outbound VGW	1.36	0.49	0.26	92.3	181.9	90.3	160/245
Difference	**0.32**	**0.1**	**0.06**	**-21.8**	**6.1**	**-6.5**	**20/120**

Note - In the "Difference" row (row 4), positive velocity values (columns 2-4) indicate a greater outbound VGW event-driven current value while negative values indicate a greater wind-driven current value.

Table 22 – Calculated hydrodynamic statistics during and after an outbound wake event.

Current Driver	Frequency (%) per Velocity (m/s) Bin				Mean Direction (°) per Velocity (m/s) Bin			
	V<0.4	0.4≤V<0.8	0.8≤V<1.2	V≥1.2	V<0.4	0.4≤V<0.8	0.8≤V<1.2	V≥1.2
Wind	57.8	38.3	3.8	0	175.0	177.2	173.7	-
Outbound VGW	39.4	48.7	9.9	1.9	187.6	185.3	161.1	85.9
Difference	**-18.4**	**10.4**	**6.1**	**1.9**	**12.6**	**8.1**	**-12.6**	**-**

Note - In the "Difference" row (row 4), positive velocity frequency values (columns 2-5) indicate a greater frequency in the outbound VGW event-driven current while negative values indicate a greater frequency in the wind-driven current.

A slight strengthening of the current velocity magnitudes is observed during the wake event, as well as a coincident shift in current direction. As with the inbound event, partitioning the outbound VGW event (Fig. 41, right panel) into the 2 main components allows for higher-resolution insights into the different hydrodynamic conditions present during the wake (Fig. 42, Tables 23-24).

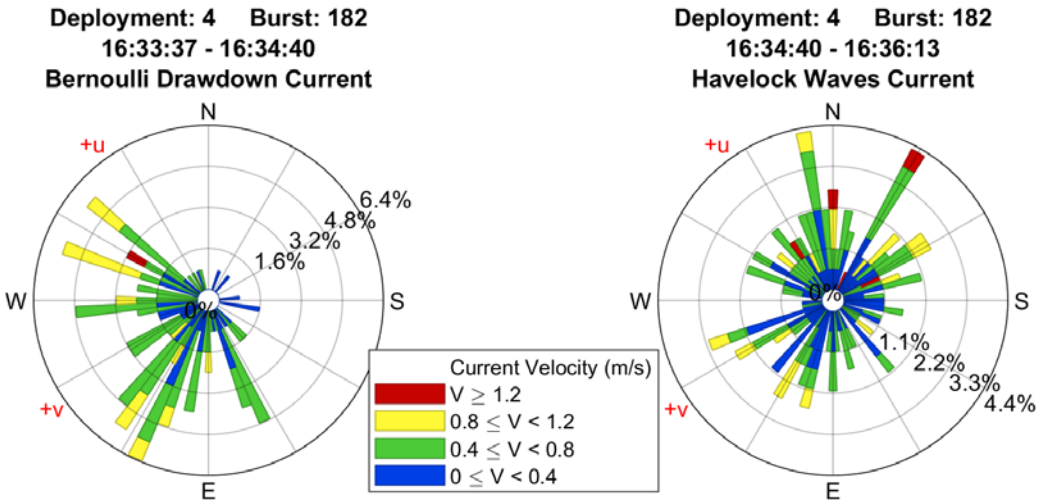

Fig. 42 - Wind rose styled plots of the current during the two main wake components, the low-frequency Bernoulli wave drawdown (left) and the high-frequency Havelock surface wave packet (right).

Table 23 – Calculated hydrodynamic statistics during the low frequency drawdown and high frequency surface wave components of the outbound wake event.

	Velocity (m/s)			Direction (°)			
Current Driver	Max	Mean	Std. Dev.	At Max Vel	Mean	Std. Dev	Mode
Wind	1.04	0.39	0.2	114.1	175.8	96.8	130
Drawdown	1.23	0.52	0.24	152.1	215.8	60.3	245
Difference	**0.19**	**0.13**	**0.04**	**38.0**	**40.0**	**-36.5**	**115**
Surface Waves	1.36	0.48	0.27	92.3	159.4	99.6	60/100
Difference	**0.32**	**0.09**	**0.07**	**-21.8**	**-16.4**	**2.8**	**-70/-30**

Note - In the "Difference" rows (row 4 & 6), positive values (columns 2-4) indicate a greater outbound VGW event-driven current component value while negative values indicate a greater wind-driven current value. Each component "Difference" row is relative to the quiescent, wind-driven conditions.

Table 24 – Calculated hydrodynamic statistics after the outbound wake event, during the low frequency drawdown inbound wake component, and during the high frequency surface wave inbound wake component.

Current	Frequency (%) per Velocity (m/s) Bin				Mean Direction (°) per Velocity (m/s) Bin			
Driver	V<0.4	0.4≤V<0.8	0.8≤V<1.2	V≥1.2	V<0.4	0.4≤V<0.8	0.8≤V<1.2	V≥1.2
Wind	57.8	38.3	3.8	0	175.0	177.2	173.7	-
Drawdown	30.2	57.9	11.1	0.8	217.2	219.0	199.7	152.1
Difference	**-27.6**	**19.6**	**7.3**	**0.8**	**42.2**	**41.8**	**26.0**	**-**
Surface Waves	45.5	42.2	9.6	2.7	174.3	206.1	135.4	72.6
Difference	**-12.3**	**3.9**	**5.8**	**2.7**	**-0.7**	**28.9**	**-38.3**	**-**

Note - In the "Difference" rows (row 4 & 6), positive frequency values (columns 2-5) indicate a greater frequency in the outbound VGW event-driven current component while negative values indicate a greater frequency in the wind-driven current. Each component "Difference" row is relative to the quiescent, wind-driven conditions.

Each phase of the wake event was distinct from the quiescent conditions, however more so in current velocity directions than magnitudes. Comparing the quiescent and outbound VGW component velocity magnitudes and contrasting the 2 wake components against each other indicate that:

- The max velocity magnitudes were 18% and 33% greater during the drawdown and surface wave phases relative to the quiescent period, respectively (Table 23).

- The mean velocity magnitude was about 31% and 23% greater than the mean quiescent magnitude during the drawdown and surface wave phases, respectively (Table 23).
- Although the drawdown phase had a slightly greater mean magnitude, the surface wave phase had a similar fraction of magnitudes at or above 0.8 m/s (Table 24).
    - 11.9% of the roughly 60-second drawdown had magnitudes at or above 0.8 m/s compared to 12.3% of the roughly 90-second surface wave phase.
    - Both wake phases had rates of magnitudes at or above 0.8 m/s approximately 3 times larger than the 3.8% of the 150-second quiescent period.
- The surface wave phase contained the largest proportion of magnitudes over 1.2 m/s (Table 24).
    - 2.7% of surface waves were above 1.2 m/s, compared to 0.8% of the drawdown and no values during the quiescent conditions.

The current direction patterns observed during the quiescent period, wake drawdown phase, and wake surface wave phase were highly variant, notably due to the unique hydrodynamics present during an outbound VGW event. Rather than the standard shore-normal wave approach, outbound VGW events refract around the site shoreline in a shore-parallel manner (i.e., in the -v direction). The resulting current direction observations include:

- The quiescent condition was fairly spread across all directions, however the directions with maximum frequency were in the onshore direction (Fig. 41, left panel).
- 90% of the drawdown was within 90° of -v, shore-parallel towards the HSC (Fig. 42, left panel).
- 61% of the surface wave phase oscillated within 45° of shore parallel (Fig. 42, right panel):
    - 33% within 45° of +v.
    - 28% within 45° of -v.
- 100% of the current magnitudes above 1.2 m/s during the surface wave phase were between 25-125° (Fig. 42, right panel).
    - Due to currents at the offshore platform refracting towards the shore at a -v heading.

5.2.3 General Discussion

The current direction and magnitude details discussed in sections *5.1.1-5.1.2* reflect the hydrodynamics expected during VGW events from transits in both inbound and outbound directions.

Drawdowns from each event gravitated towards the HSC, however the outbound events resulted in an average direction just 5° over +v, 15° closer than the average direction of inbound events (Figs. 39 and 42, left panels and Tables 19 and 23). This 15° split in mean drawdown directions is a natural outcome considering the outbound vessels approach from the Northwest and inbound vessels approach from the South (Fig. 9).

The different approach directions yield an important caveat in how the wakes were delineated, specifically due to the dissimilar nature of the bow and stern wake component interactions (Fig. 3) during each VGW event. As can be seen in Fig. 37, the inbound wake arrives as a relatively continuous event, with the bow and stern components only distinguishable by two prominent troughs in the mid frequency bin (Fig. 37, panel C). These troughs arrive at around 19:15:15 and 19:60:00, and are therefore separated by about 45 seconds. Outbound wakes, in contrast, resemble 2 discontinuous events where the bow and stern components are much more clearly defined. In Fig. 40, each panel presents a clear split in hydrodynamic impacts as the bow arrives at 16:34:40 while the stern arrives 140 seconds later at 16:37:00. This considerable change to continuity is likely due to the close proximity of the outbound vessel with the nearby embankment parallel to the HSC. The interaction between the shoreline and the confined wake delays the stern arrival through shoaling and refraction processes, resulting in greater separation between the components. Because of the discontinuity in bow and stern components of outbound wakes, the analysis in section *5.2.2* only considers the bow portion of the wake (i.e., the event is truncated at 16:36:13 rather than 16:38:00). This truncation is intended to isolate the surface wave phase as much as possible, as the hydrodynamics of the stern component drawdown phase would otherwise obfuscate the hydrodynamics unique to the surface wave phase.

Although Fig. 37 and Fig. 40 pertain to VGW events from particular ships, the general hydrodynamic trends found in each (i.e., inbound VGW event trends from Fig. 37 and outbound VGW events trends from Fig. 40) are broadly, but not exactly, similar across all VGW events with similar transit heading directions. Examples of the discrepancies between different VGW events with similar transit headings include the exact magnitudes of wave heights, the duration of the wake events, and the time separating the arrivals of the bow and stern wake event components.

Figure 43, an image from a previous paper using the HSC for a study site, illustrates this interaction for an inbound vessel having already passed the platform site and traveling along the shoreline [Tate et al., 2008]. The current velocity disturbance measured in the wake section to the right of the vessel is nonsymmetric with the disturbance to the left; the trailing edge for the right half of the wake event lags behind the corresponding edge for the left half. This lag leads to a longer distance between the bow-related leading edge and stern-related trailing edge of the disturbance, yielding the additional 100 seconds observed between the outbound bow and stern components.

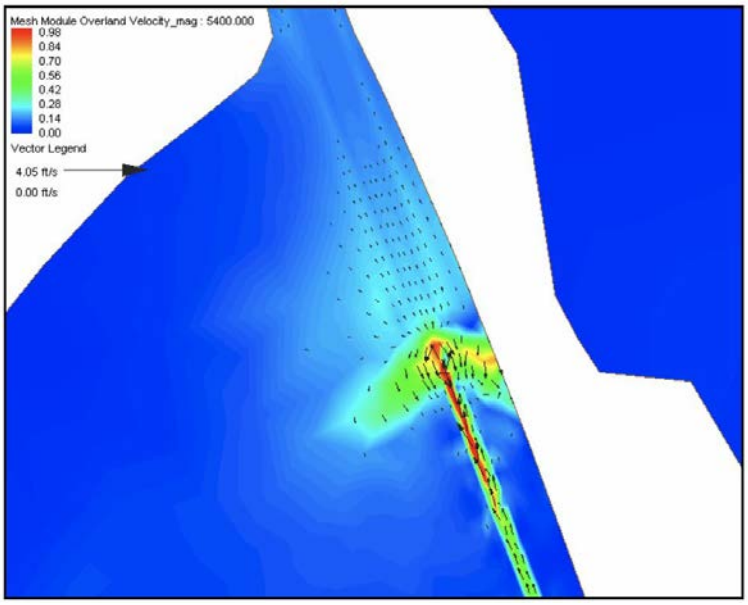

Fig. 43 – Model of a wake disturbance field for an inbound vessel defined using current velocities. The right half of the disturbance appears to lag behind the left half following shoaling and refraction along the surfzone. Figure adapted from Tate et al. (2008).

Unlike the drawdowns, the surface wave components of the VGW events impacted the site along completely different axes (Figs. 39 and 42, right panels and Tables 19 and 23). The inbound surface waves arrived on a shore-normal wave attack angle, while the refracting outbound surface waves traveled shore-parallel. A major difference between the VGW events was the form of the surface waves; inbound waves arrived unbroken from the relatively deeper offshore direction while the outbound waves, refracting along the shoreline surfzone, propagated as a disorganized packet of broken waves. The effects of this wave structure disparity can be understood by comparing the high frequency bin of the combined multiresolution analysis (i.e., 1-8 second wave periods), where the inbound event (Fig. 37, panel D) records a surface wave component possessing considerably more wave energy relative to the high frequency bin of the outbound event (Fig. 40, panel D). Using the ability of multiresolution analyses to quantify the signal energy present in each frequency bin (28), this translates to the high-frequency bin containing 36% of the energy measured during the inbound wake event but only 16% of the outbound wake energy.

A secondary impact of the inbound surface waves propagating as an organized and unbroken wave packet is the greater velocity magnitudes contained in the high frequency waves relative to the outbound wake surface waves (Tables 19-20 and Tables 23-24). The inbound surface waves recorded maximum and mean velocities 21% and 16% greater than the outbound surface waves,

respectively. Additionally, outbound surface wave current magnitudes were only at or above 0.4 m/s for 55% of the event as compared to the 72% of inbound wakes. The extended periods of greater current velocity magnitudes during inbound VGW events most likely lead to increased erosion and corollary sediment transport rates at the site.

5.3 Correlating AIS Vessel Data with Observed Wake Characteristics (RQ1)

For the VGW events both positively identified and usable, dimensional correlations were attempted using vessel specifications including length, beam, draft, summer deadweight tonnage, gross deadweight tonnage, and block coefficients. The specifications were correlated to hydrodynamic statistics including total energy, significant wave height, max wave height, mean period, drawdown duration, drawdown magnitude, max u component velocity, and max v component velocity. Nondimensional correlations were attempted using the depth Froude number, length Froude number, and modified Froude number presented by Kriebel & Seelig (2005) against the nondimensionalized velocity head value. Only the vessel specifications resulting in relatively strong correlations are presented, all of which are for transits with an inbound heading. Outbound headings did not result in notable correlations for any of the parameters, most likely due to the fact that extensive wave transformations had already taken place (i.e., wave breaking, shoaling, and refracting).

For sections *5.3.1-5.3.2,* the number of samples in each depth bin were N=153 for the low tide bin, N=244 for the mid tide bin, and N=371 for the high tide bin. Section *5.3.3,* correlations for a uniform ship length, had sample sizes reduced to N=46, N=87, and N=105 for the respective low, mid, and high tide bins. The lower number of sample sizes compared to the total number of valid wakes is due to instances of incomplete AIS data wherein complete vessel specifications were unavailable.

5.3.1 Vessel Length

Figure 44 presents the correlations between vessel hull length and the observed VGW event hydrodynamic statistics of total event energy (panel A), mean period (B), significant wave height (C), and maximum wave height (D). Figure 45 presents the correlations between vessel hull length and the observed VGW event hydrodynamic statistics of drawdown duration (panel A), drawdown magnitude (B), max u velocity (C), and max v velocity (D). Vessel length was the second-best performing parameter in the correlation analyses, including a regression of R^2=0.26 for significant wave heights and R^2=0.3 for drawdown durations, both for while the depth was at higher tides.

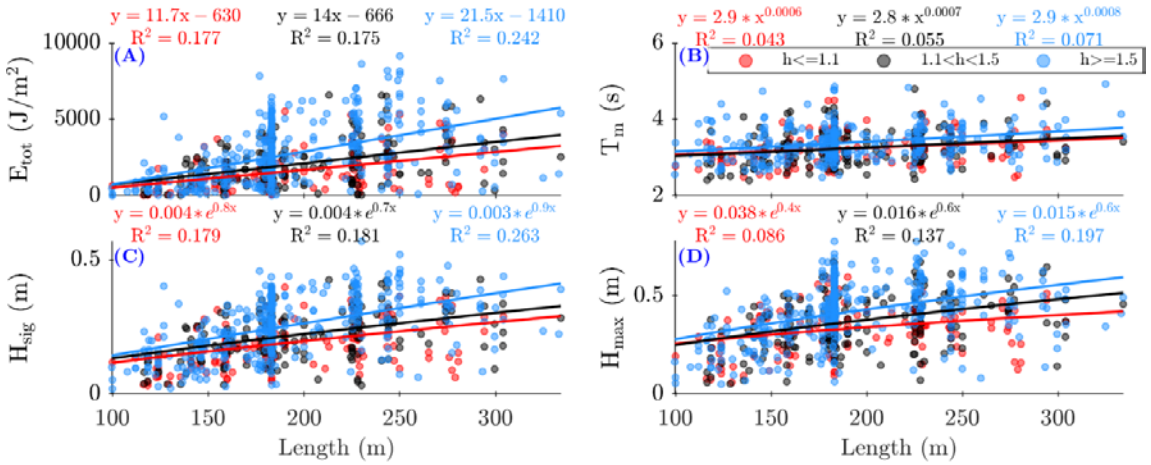

Fig. 44 – Correlations between the vessel length and hydrodynamic parameters of total wave energy, mean wave period, significant wave height, and maximum wave height (panels A-D, respectively). Low tide depths (below 1.1 m) are red, mid tide depths (between 1.1 and 1.5 m) are black, and high tide depths (over 1.5 m) are blue. Regression equations and correlation fit values are found above each panel and are color coded to match the corresponding depth represented.

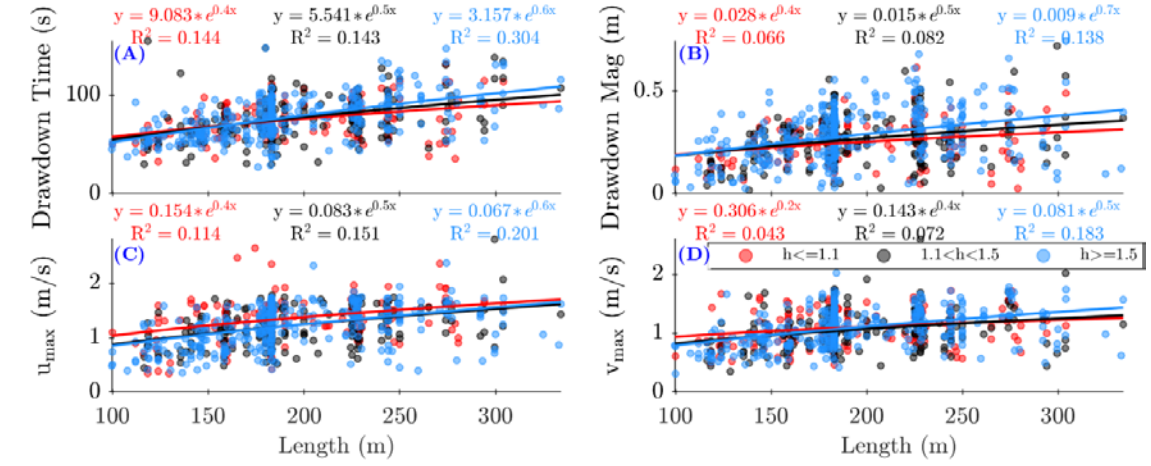

Fig. 45 – Correlations between the vessel length and hydrodynamic parameters of drawdown duration, drawdown magnitude, maximum u velocity, and maximum v velocity (panels A-D, respectively). Low tide depths (below 1.1 m) are red, mid tide depths (between 1.1 and 1.5 m) are black, and high tide depths (over 1.5 m) are blue. Regression equations and correlation fit values are found above each panel and are color coded to match the corresponding depth represented.

As is observed across each of the correlation plot panels in Figs. 44-45 (and will continue to be observed in the coming correlation figures), the R^2 values tended to improve with deeper depths. This trend can be explained, at least in part, by the fact that less hydrodynamic transformations will occur in the propagating waves as the water becomes deeper.

5.3.2 Gross Tonnage

Figure 46 presents the correlations between vessel design gross tonnage and the observed VGW event hydrodynamic statistics of total event energy (panel A), mean period (B), significant wave height (C), and maximum wave height (D). Figure 47 presents the correlations between vessel design gross tonnage and the observed VGW event hydrodynamic statistics of drawdown duration (panel A), drawdown magnitude (B), max u velocity (C), and max v velocity (D). The vessel design gross tonnage was the best performing parameter in the correlation analyses, including a regression of R^2=0.32 for significant wave heights and drawdown durations, both again while the depth was at higher tides.

The gross tonnage is specifically noted as the design tonnage due to the in-situ tonnage information not being available. Design tonnage is the displacement of the vessel alone, typically listed by the vessel manufacturer. Using the design tonnage is less of an issue for transits of vessels with unloaded conditions, however transits of loaded vessels will have a considerably underestimated tonnage value relative to the design tonnage. This higher margin of error in tonnage values likely explains why block coefficient correlations performed poorly, as these statistics have a direct dependence on tonnage accuracy (1f). Had the exact vessel tonnage information been available, the gross tonnage and block coefficient correlations would likely have seen a notable improvement in the R^2 value.

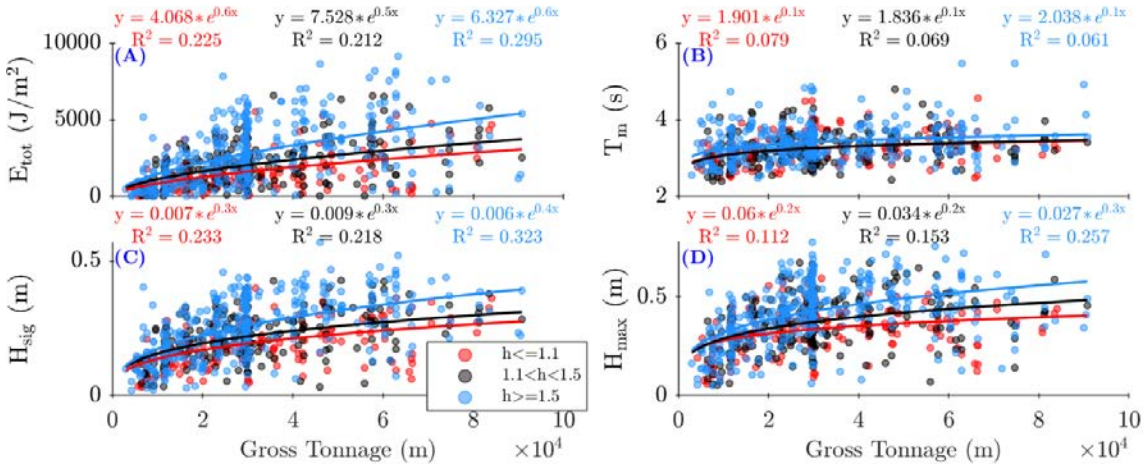

Fig. 46 – Correlations between the vessel design gross tonnage and hydrodynamic parameters of total wave energy, mean wave period, significant wave height, and maximum wave height (panels A-D, respectively). Low tide depths (below 1.1 m) are red, mid tide depths (between 1.1 and 1.5 m) are black, and high tide depths (over 1.5 m) are blue. Regression equations and correlation fit values are found above each panel and are color coded to match the corresponding depth represented.

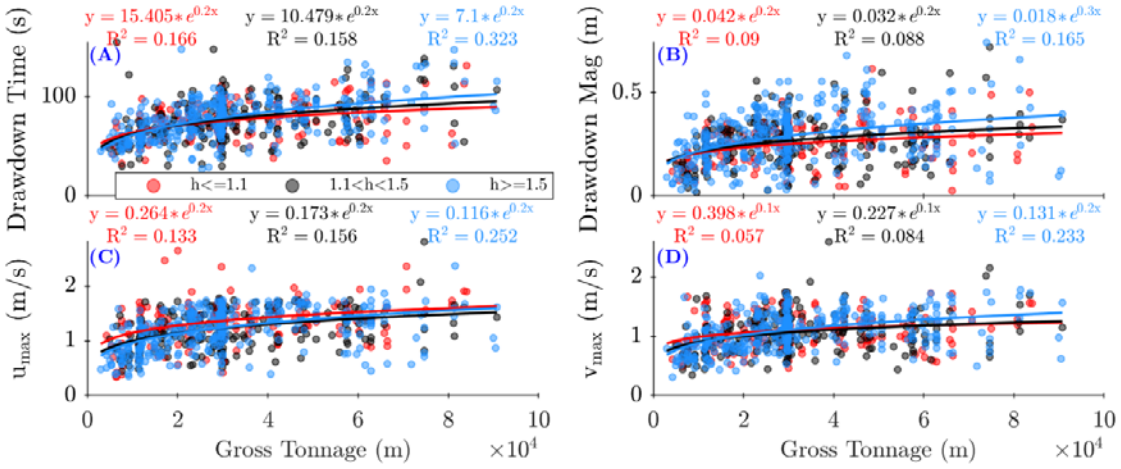

Fig. 47 – Correlations between the vessel design gross tonnage and hydrodynamic parameters of total wave energy, mean wave period, significant wave height, and maximum wave height (panels A-D, respectively). Low tide depths (below 1.1 m) are red, mid tide depths (between 1.1 and 1.5 m) are black, and high tide depths (over 1.5 m) are blue. Regression equations and correlation fit values are found above each panel and are color coded to match the corresponding depth represented.

5.3.3 Transit Velocity for Vessels of Similar Length

Figure 48 presents the correlations between vessel velocity around the time the vessel was traveling near the platform latitude and the observed VGW event hydrodynamic statistics of total event energy (panel A), mean period (B), significant wave height (C), and maximum wave height (D) for vessels between 180 and 190 m length. This range of hull lengths was chosen due to this class of vessel providing the most potential samples while maintaining stationarity in the length specification (Fig 21, panel A). As with the correlations in *5.3.1-5.3.2,* the highest tides provided the strongest regression R^2 values, with significant wave height giving an R^2=0.34 and total event wave energy an R^2=0.31.

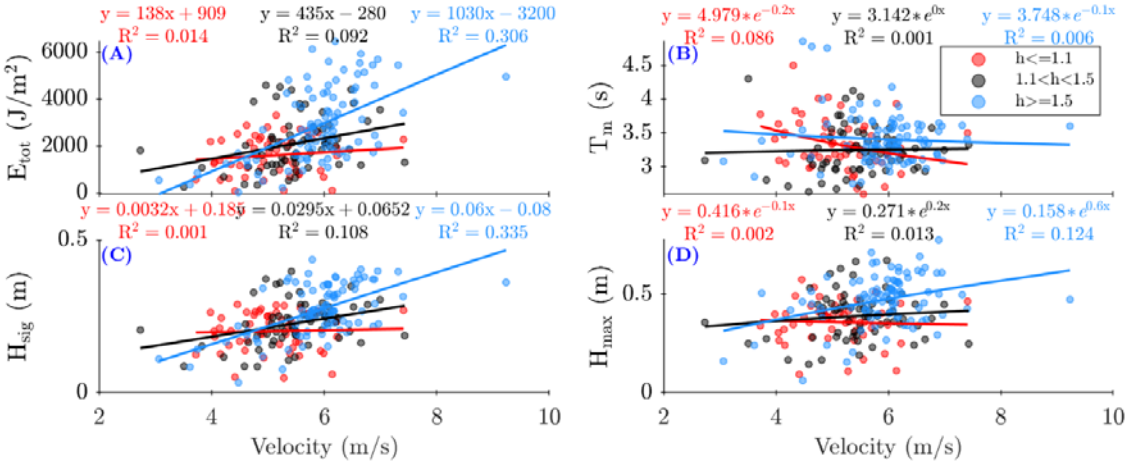

Fig. 48 – Correlations between the vessel velocity and hydrodynamic parameters of total wave energy, mean wave period, significant wave height, and maximum wave height (panels A-D, respectively). Only vessels between 180-190 m were used in order to maintain stationarity in vessel length. Low tide depths (below 1.1 m) are red, mid tide depths (between 1.1 and 1.5 m) are black, and high tide depths (over 1.5 m) are blue. Regression equations and correlation fit values are found above each panel and are color coded to match the corresponding depth represented.

5.3.4 Froude Numbers

Figure 49 illustrates the relationship between 2 forms of the nondimensional vessel velocity head (gH_{sig}/V^2 in panels A, C, E, and gH_{max}/V^2 in panels B, D, and F) and 3 forms of the Froude number (Froude depth in panels A and B, Froude length in panels C and D, and modified Froude number in panels E and F). As the gross tonnage parameter provided considerably better regression values relative to the summer deadweight tonnage, the gross tonnage was used for the displacement value in the Kriebel & Seelig (2005) modified Froude parameter equation (1d).

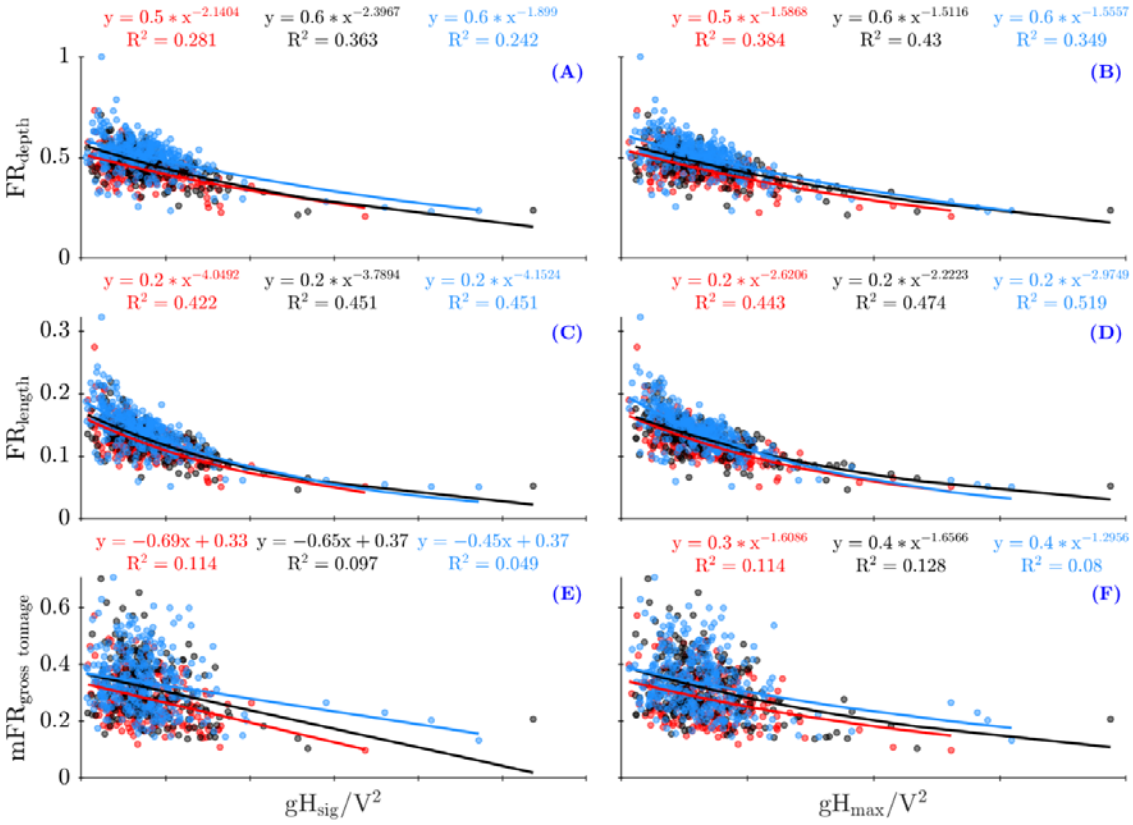

Fig. 49 – Correlations between 2 forms of the vessel velocity head and 3 forms of the vessel Froude number. Low tide depths (below 1.1 m) are red, mid tide depths (between 1.1 and 1.5 m) are black, and high tide depths (over 1.5 m) are blue. Regression equations and correlation fit values are found above each panel and are color coded to match the corresponding depth represented.

Of the 3 Froude numbers, the Froude length number was consistently the strongest performer with an R^2 between 0.42 and 0.45 across all depths when using the significant wave height form of the velocity head, and an R^2 between 0.44 and 0.52 when using the max wave height for of the velocity head. The Froude length and velocity head correlations were the strongest regression coefficient values across all of the correlation analyses. As mentioned in section *5.3.2*, the modified Froude number advanced by Kriebel & Seelig (2005) likely performed as poorly as it did due to tonnage values containing high margins of error.

5.4 Determining Wave-Condition Contributions Towards the Total Energy Budget (RQ2)

5.4.1 Energy Budget Considerations Over Entire Study Period

Table 25 and Fig. 50 provide the hydrodynamic statistics for each type of wave event considered by the study. Inbound wake events consistently resulted in the largest values measured across each statistic on a per-event basis, including:

- average maximum energy per minute values nearly 4 times higher than both wind-wave and outbound wake events;
- a peak max energy per minute value nearly 2 times higher than wind-wave and 3 times higher than the peak of outbound wake events;
- average significant and max wave heights around 3 times higher than wind-wave and 2 times higher than outbound wake events;
- a max significant wave height about 2 times higher than the max of wind-wave and outbound wake events.

Figure 51 illustrates the temporal (left chart) and measured energy (right chart) breakdown of each wave event classification able to be isolated across the entire study period. Isolated VGW events are complete, positively identified events unaffected by interference from any additional VGW events. Isolated wind events are from entire ADCP bursts where AIS records and statistical checks discussed in section *4.2.3* confirm no deep-draft nor shallow-draft (i.e., tug or barge) VGW events occurred. As the wake events were delineated using an assumed 3.5-minute duration, wind event values were found via calculating the average energy per minute during the burst and multiplying that value by 3.5 so as to create events with durations matching those of the wake events.

Table 25 – Summaries of hydrodynamic statistics for each wave event classification.

Statistic		Wind Only N = 5,426	Outbound Wake Events N = 1,176	Inbound Wake Events N = 1,172
Max Energy Per Minute (J/m^2*min)	Mean	235.5	238.7	1,209.9
	Max	2,885.4	1,766.4	5,330.3
	Std Dev	303.3	195.7	858.9
Significant Wave Height (m)	Mean	0.075	0.10	0.23
	Max	0.31	0.33	0.57
	Std Dev	0.056	0.043	0.10
Max Wave Height (m)	Mean	0.13	0.18	0.37
	Max	0.58	0.49	0.82
	Std Dev	0.092	0.068	0.14
Mean Wave Period (s)	Mean	2.57	2.79	3.32
	Max	3.79	4.32	5.57
	Std Dev	0.22	0.33	0.43

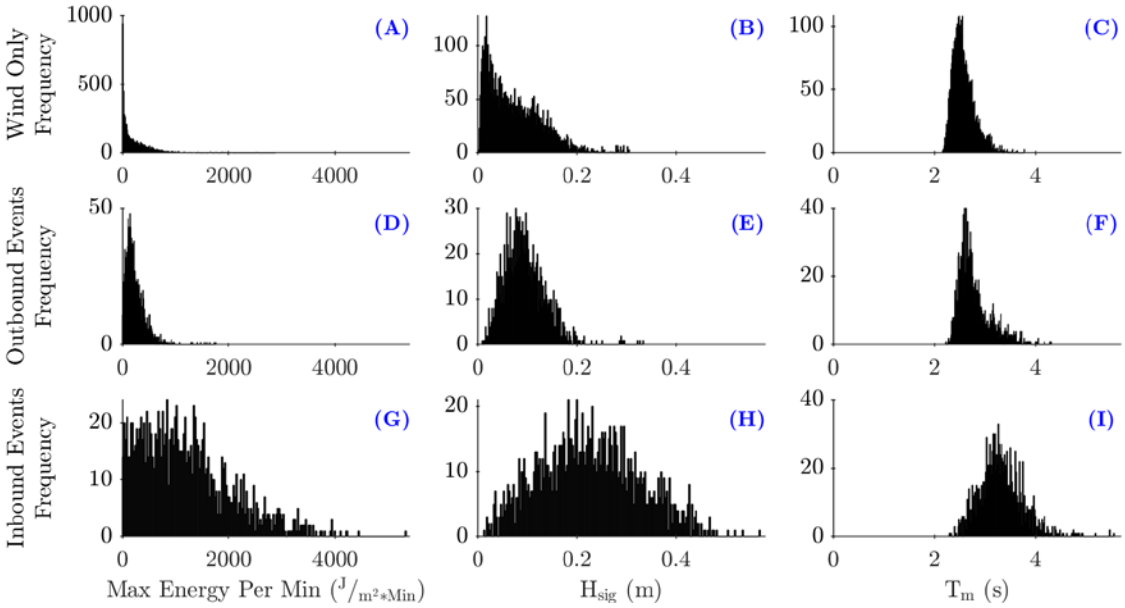

Fig. 50 – Histograms of hydrodynamic statistics for each wave event classification.

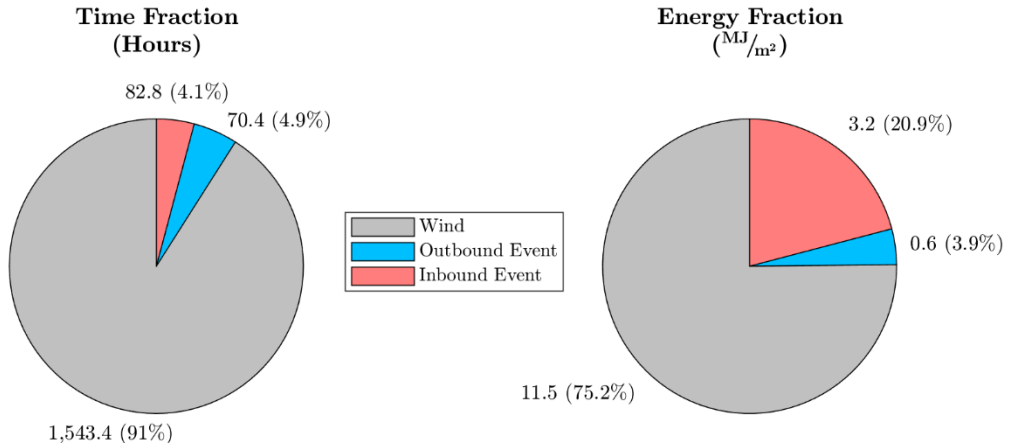

Fig. 51 – Breakdowns of the time fraction (left) and measured energy fraction (right) of wind-only bursts, inbound wake events, and outbound wake events able to be isolated during the entire study period.

Figure 51 is a clear indication of the outsized impact inbound wakes pose to the site relative to wind waves and outbound VGW events. Despite only occurring during about 4% of the time, inbound VGW events consisted of about 20% of measured wave energy. Interestingly, outbound VGW events were actually responsible for a lower energy fraction (about 4%) than the time fraction (about 5%), an observation likely due to the poorly formed wave shape that wakes events from outbound vessels propagate with.

The energy fraction of inbound wake events is noted to be likely even higher when considering the number of wakes the analysis was not able to include, whether due to partial capture, interference with another VGW event, or missed identification due to an inactive ADCP or algorithm error. Similarly, the time fraction of wind-only events is noted to be likely higher considering the exclusion of the remaining time periods in bursts surrounding wake events that would have been wind-only wave action, and also the exclusion of wind-only bursts where the AIS data or calculated hydrodynamic statistics prevented a high-confidence classification as such. As was previously mentioned, the wind-only component of the time and energy budgets only considered entire bursts that were able to be definitively identified as only having wind-generated wave forcings.

A caveat to Fig. 51 is that the total wave energy budget (the rightmost chart) may be slightly misleading when considering the wave energies through the scope of erosion rates. Despite the wind-wave events constituting 75% of the measured wave energy, in reality this total energy value is the cumulative result of numerous waves with notably smaller wave heights (Table 25 and Fig. 50) and weaker current velocity magnitudes (sections *5.2.1-5.2.2)*. Since vessel wakes often result in a sediment-entraining drawdown event (i.e., from the scraping forces created by

the retreating water) immediately followed by a packet of waves containing relatively large wave heights (Table 25 and Fig. 50) and current velocities (sections *5.2.1-5.2.2)*, sediment transport rates are likely to greatly increase during these VGW events. The greater transport rates from VGW events would stem from both an increased volume of fine-grain sediment erosion along with the erosion of coarser-grain sediments that would otherwise be unaffected by the weaker wind-wave energies. Confirmation of the increased transport rates induced by VGW events could take the form of sediment transport equations or pickup functions using the known in-situ conditions and measured hydrodynamic data; while not having been performed yet, such calculations are expected to follow the completion of this analysis.

5.4.2 Energy Budget Considerations Over a Two-Week Period

Figure 52 illustrates a high-resolution look into a 2-week period during March 2018, plotting the wind direction and velocity (panels A-B) and the max measured energy per event (panel C). Confirming the trends found in Figs. 50-51 and Table 25, the inbound VGW events are observed as the dominant source of wave energy at the site while outbound VGW events are essentially indistinguishable from the background wind-only events.

Although several cold fronts pass over the site as denoted by the sudden wind direction changes on March 18th, 19th, 22nd, and 25th, the wind velocities (and by extension wind event energies) are generally found to follow the daily cyclical pattern of the sea breeze effect (section *3.1.3*). A clear frontal impact, however, is the cold front arriving on March 19th that resulted in a sustained change in the wind direction over a roughly 3-day period. As this new direction provided a much smaller fetch length (Fig. 16), the wind-wave energy was considerably dampened during this time period as is reflected by the essentially negligible wind and outbound VGW event energies that were measured (Fig. 52, panel C, black and red dots). While the wind and outbound VGW event energies were subdued, inbound VGW events appear to have been unaffected, as the largest wave energy event during the 2-week period was during this frontal event.

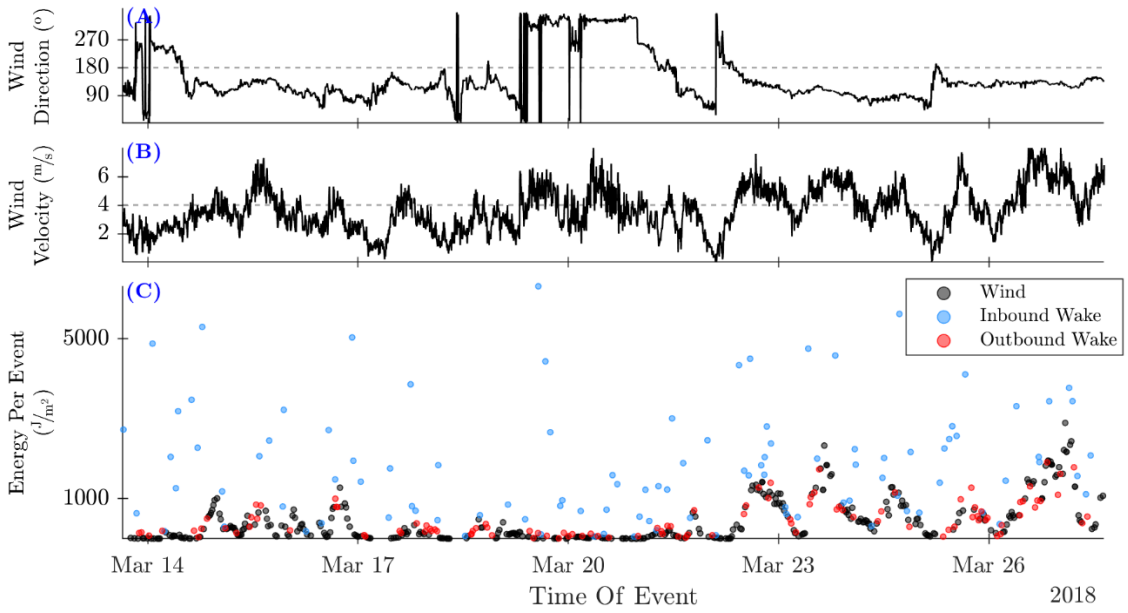

Fig. 52 – Two-week timeseries of the wind direction (panel A), wind velocity (panel B), and measured energies of the wind and vessel wake events (panel C) between March 13 and March 27, 2018.

6.0 Conclusions

Following a 10-month data collection campaign in Galveston Bay, Texas, a time-to-frequency domain analysis technique known as wavelet transformation was successfully utilized to study the hydrodynamic effects of deep-draft vessel generated wake events in a shallow bay environment. The wavelet transforms allowed for time-localized, high-resolution decompositions of water surface elevation timeseries into multiple frequency-bounded subbands using a method known as multiresolution analysis. Each subband was an octave larger than the previous, resulting in a full spectrum of 9 subbands detailing wave period information ranging from the highest frequencies (0.5-1 second wave periods) to the lowest frequencies (128-256 second wave periods) pertinent to wake events. Reaggregation of the multiple subbands down to 3 main combined frequency ranges, a high (1-8 second wave period), mid (8-32 second wave period), and low (32-256 second wave period) frequency range, provided a clear understanding of the low- and mid-frequency Bernoulli waves and high-frequency Havelock surface wave components constituting the wake events.

A multi-layered algorithm capable of positively identifying wake event arrivals in hydrodynamic data sets was next created. The algorithm analyzed the results of the multiresolution analysis and current velocity data to predict when nonstationary events found in the collected data signified the onset of a wake event. Considerations guiding the decision-making process of the

algorithm included outlying hydrodynamic statistics along with the simultaneous presence of a Bernoulli wave drawdown, packet of Havelock surface waves with notable increases in wave height, and current velocities sustaining unnatural trends in flow magnitudes and directions. Results of the algorithm were then compared with the AIS records to determine the exact vessel responsible for each identified wake event. The algorithm was able to identify roughly 75% of the 8,003 vessel transits occurring during windows of deployed hydrodynamic sensors, with a considerable portion of the remaining 25% of transits missed due to necessary periods of inactive data collection.

Following the matching of the wake events to the corresponding vessels, vessel parameters including length, draft, summer deadweight tonnage, gross deadweight tonnage, block coefficients, and Froude numbers were correlated with hydrodynamic statistics including total wave energy, significant and max wave height, mean wave period, drawdown duration and magnitude, maximum onshore and alongshore velocity components, and the nondimensional velocity head. Of the attempts, most vessel parameters did not exhibit noteworthy hydrodynamic correlations except for vessel length (R^2=0.26 for significant wave height and R^2=0.3 for drawdown duration during higher tides), unloaded gross tonnage (R^2=0.32 for significant wave height and drawdown duration during higher tides), depth Froude number (R^2=0.43 for max wave height velocity head during mid tides), and length Froude number (R^2=0.52 for max wave height velocity head during high tides). Across all the correlations, periods of lower tidal elevations provided the weakest correlations while higher tidal elevations tended to provide the strongest. These few parameters that did show modest correlations were specifically for vessel transits having an inbound traveling direction, as outbound transits consistently resulted in poor correlation regressions. The cause of the poor correlation performance by outbound transits is due to the nature of the propagating wave forms; outbound wake events propagate parallel to the shoreline as packets of broken waves due to the proximity of the embankment along the starboard side of the vessel.

Energy budget considerations confirm inbound VGW events as constituting an outsized source of the total wave energy impacting the site, while the total wave energies of outbound VGW events were often indistinguishable from the background wind-waves. Inbound VGW events recorded average maximum and significant wave heights multiple times larger than the background wind-waves, while outbound VGW events recorded average maximum and significant wave heights only around 30% higher than the background wind-waves. As with the weak correlations, the outbound VGW events imparted lower rates of wave energy to the site due to their propagation as broken waves along the shoreline, along with their shore-parallel propagation direction (i.e., opposed to the shore-normal directions of inbound VGW event waves that are naturally more efficient at transmitting wave energies into the shoreline).

This thesis lays the groundwork for several future analyses that would take the presented results a step further. The relatively immense inventory of isolated vessel wake events could be used to validate or improve the existing methods for predicting wake event wave heights and drawdown magnitudes in shallow-bay environments. An analysis of wake-induced erosion rates, possibly

even a full sediment transport model around the field site, could be created to assess how the measured wave energies translate to shoreline erosion. A numerical simulation modelling the generation of vessel wake events by specific ships can be supported using the correlation results and validated against the observed hydrodynamics detailed by the multiresolution analysis. Lastly, the vessel wake generation and sediment transport numerical models may be combined to investigate how a potential long-term increase in vessel traffic rates or a deepening of the ship channel to accommodate larger vessel classes would impact shoreline erosion.

7.0 Citations

Addison, P.S., (2017). "The Illustrated Wavelet Transform Handbook: Introductory Theory and Applications in Science, Engineering, Medicine, and Finance," 2nd ed. CRC Press, Boca Raton, FL. 446 p.

Allenstrom, B., Andreasson, H., Leer-Andersen, M., and Da-Qing, L. (2003). "Amplification of ship generated wake wash due to coastal effects," Transactions of the Society of Naval Architects and Marine Engineers 111. pp 61-77.

Chadwick, A., (2021). "Shallow-water Wave Theory." Coastal Wiki. Webpage. URL http://www.coastalwiki.org/wiki/Shallow-water_wave_theory

Daubechies, I., Grossman, A., Meyer, Y., (1986). "Painless non-orthogonal expansions," *Journal of Mathematics and Physics* 27. pp 1271-1283.

Daubechies, I., (1988). "Orthonormal basis of compactly supported wavelets," *Communications on Pure and Applied Mathematics* 41. pp 909-996.

Daubechies, I., (1990). "The Wavelet Transform time-frequency localization and signal analysis," *IEEE Transactions on Information Theory* 36(5). pp 961–1004.

Daubechies, I., (1992). "Ten lectures on wavelets," *Wavelets and Their Applications,* Lecture given at the Conference Board of the Mathematical Sciences Conference on Wavelets and Their Applications, Regional Conference Series in Applied Mathematics. Lowell, MA, 1990.

Elgar, S. & Raubenheimer, B., Guza, R.T., (2001). "Current meter performance in the surf zone," *Journal of Atmospheric and Oceanic Technology* 18. pp 1735–1746.

Elgar, S., Raubenheimer, B., Guza, R.T., (2005). "Quality control of acoustic Doppler velocimeter data in the surfzone," *Measurement Science and Technology* 16. pp 1889–1893.

Elgar, S. & Raubenheimer, B., (2008). "Wave dissipation by muddy seafloors," *Geophysical Research Letters* 35. 5 p.

Engineering Research and Development Center (ERDC), (1977). "Chapter 3.4: Wind Information Needed for Wave Prediction," *Shore Protection Manual*. Vol. 1, 3rd ed, U.S. Army Corps of Engineers Coastal Research Center, Vicksburg, MS. 541 p.

Engineering Toolbox, (2003). "Specific Heat of Some Common Substances," Webpage. URL https://www.engineeringtoolbox.com/specific-heat-capacity-d_391.html

Farge, M., (1992). "Wavelet Transforms and their applications to turbulence," *Annual Review of Fluid Mechanics* 24. pp 395–457.

Froude, W., (1874). "Experiments with H.M.S. Greyhound," *Transactions of the Society of Naval Architects and Marine Engineers* 15(1). pp 36-73.

Gamage, N.K.K., (1990). "Detection of coherent structures in shear induced turbulence using wavelet transform methods," *Ninth Symposium on Turbulence and Diffusion,* American Meteorological Society. pp 453-454.

Gamage, N.K.K. & Hagelberg, C.R., (1993). "Detection and Analysis of Microfronts and Related Events," *Journal of the Atmospheric Sciences* 50(5). pp 750–756.

Gilmer, B. (2018). "Proximity Counts: How Houston Dominates the Oil Industry," *Forbes*, Webpage. URL https://www.forbes.com/sites/uhenergy/2018/08/22/proximity-counts-how-houston-dominates-the-oil-industry/#7964a8261078

Grossmann, A. & Morlet, J., (1984). "Decomposition of Hardy functions into square integrable wavelets of constant shape," *SIAM Journal on Mathematical Analysis* 15. pp 723–736.

Grossman, A., Morlet, J., Paul, T., (1985). "Transforms associated to square integrable group representations," *Journal of Math and Physics* 26. pp 2473-2479.

Grossman, A. & Morlet, J., (1985). "Decomposition of functions into wavelets of constant shape and related transforms," *Mathematics and Physics: Lectures on Recent Results*. pp 135-165.

Hagelberg, C.R. & Gamage, N.K.K., (1994). "Structure-preserving wavelet decompositions of intermittent turbulence," *Boundary-Layer Meteorology* 70. pp 217–246.

Havelock, T.H., (1908). "The propagation of groups of waves in dispersive media, with application to waves on water," *Proceedings of the Royal Society* 81. pp 398–430.

Henry, W.K. (1979). "Some Aspects of the Fate of Cold Fronts in the Gulf of Mexico," *Monthly Weather Review*, Notes and Correspondence 107. pp 1078–1082.

Herbich, J.B. & Schiller Jr., R.E. (1984). "Surges and waves generated by ships in a constricted channel," *Coastal Engineering Proceedings 1984.* pp 3212-3226.

International Maritime Organization (IMO), (2019). "AIS Transponders," Webpage. URL https://www.imo.org/en/OurWork/Safety/Pages/AIS.aspx

Kaiser, G., (1994). “A Friendly Guide to Wavelets,” Birkhäuser. 300 p.

Kocen, M., (2013). “Observations of Sea-Breeze Fronts Along the Houston Gulf Coast,” Master of Science Thesis for the Department of Earth and Atmospheric Science, University of Houston. 76 pp.

Kriebel, D.L. & Seelig, W.N., (2005). "An empirical model for ship-generated waves," *Proceedings of the 5th International Symposium on Ocean Wave Measurement and Analysis*, Madrid, Spain. 19 p.

Kumar, P. & Foufoula-Georgiou, E., (1997). “Wavelet analysis for geophysical applications,” *Reviews of Geophysics* 35(4), American Geophysical Union. pp 385-412.

Mallat, S.G., (1989a) “Multiresolution approximation and wavelet orthonormal bases of L^2 ($\mathbb{R}$),” *Transactions of the American Mathematical Society* 315(1). pp 69-88.

Mallat, S.G., (1989b). “A theory for multiresolution signal decomposition: the wavelet representation,” *IEEE Transactions on Pattern Analysis and Machine Intelligence* 11(7). pp 674–693.

MarineTraffic, (2020). Webpage. URL marinetraffic.com

MarineTraffic, (2021). “How often do the positions of the vessels get updated on MarineTraffic?” Webpage. URL https://help.marinetraffic.com/hc/en-us/articles/217631867-How-often-do-the-positions-of-the-vessels-get-updated-on-MarineTraffic-

Massel, S.R., (2001). "Wavelet Analysis for Processing of Ocean Surface Wave Records," *Ocean Engineering* 28. pp 957–987.

MathWorks, (2019). “Choose a Wavelet.” Webpage. URL https://www.mathworks.com/help/wavelet/gs/choose-a-wavelet.html

Meyer, Y. (1989). "Orthonormal Wavelets," *Wavelets*, Inverse Problems and Theoretical Imaging Series. Springer. pp 21-37.

Meyer, Y.F., (1990). "Wavelets and Applications," *Proceedings of the International Congress of Mathematicians.* pp 1619–1626.

Meyers, S.D., Kelly, B.G., O’Brien, J.J., (1993). "An Introduction to Wavelet Analysis in Oceanography and Meteorology: With Application to the Dispersion of Yanai Waves," *Monthly Weather Review* 121. pp 2858–2866.

Morlet, J., Arens, G., Fourgeau, I., Giard, D., (1982). “Wave propagation and sampling theory,” *Geophysics* 47. pp 203-236.

NOAA, (1989). “Galveston Bay: Issues, Resources, Status, and Management,” NOAA Estuary-of-the-Month Seminar Series No. 13, NOAA Estuarine Programs Office. U.S. Department of Commerce. 114 p.

NOAA, (2021a). “El Nino & La Nina (El Nino-Southern Oscillation),” Webpage. URL https://www.climate.gov/enso

NOAA, (2021b). “El Nino-Southern Oscillation Cold & Warm Episodes by Season,” Webpage. URL https://origin.cpc.ncep.noaa.gov/products/analysis_monitoring/ensostuff/ONI_v5.php

Nortek, (2008a). “Aquadopp Current Profiler User Manual,” Nortek Doc. No. N3009-103 Revision C. 83 p.

Nortek, (2008b). “Aquadopp HR Current Profiler User Manual,” Nortek Doc. No. AHR00-0101-0508. 39 p.

Nortek, (2019). “How is SNR given in Storm?” Nortek Support Center Online FAQ, Webpage. URL https://support.nortekgroup.com/hc/en-us/articles/360029829711-How-is-SNR-given-in-Storm-

Percival, D.B., & Guttorp, P., (1994). "Long-memory processes, the Allan variance and wavelets," *Wavelets in Geophysics*. pp 325- 344.

Percival, D.P., (1995). "On estimation of the wavelet variance," *Biometrika* 82(3). pp 619–631.

Percival, D.P. & Mofjeld, H.O., (1997). "Analysis of subtidal coastal sea level fluctuations using Wavelets," *Journal of the American Statistical Association* 92(439). pp 868–880.

Port of Houston, (2018). “Port Statistics,” Webpage. URL https://porthouston.com/about-us/statistics/

Qiu, L. & Meng, H.E., (1995). “Wavelet spectrogram of noisy signals.” *International Journal of Electronics*, 79. pp 665–677.

Rayson, M.D., Gross, E.S., Fringer, O.B., (2015). “Modeling the Tidal and Sub-Tidal Hydrodynamics in a Shallow, Micro-Tidal Estuary,” *Ocean Modelling* 89, pp 29–44.

Schroeder, M.J. & Buck, C.C., (1970). “A Guide for Application of Meteorological Information to Forest Fire Control Operations,” U.S. Department of Agriculture Forest Service Handbook 360, Webpage. URL https://www.nwcg.gov/publications/pms425-1/air-masses-and-fronts

Scully, B.M. & McCartney, A.C., (2017). "Use of AIS and AISAP for analysis of vessel wakes in Charleston Harbor: A case study," *Coastal and Hydraulics Engineering Technical Note CHETN-IX-46,* Coastal Hydraulics Lab, U.S. Army Corps of Engineers Engineer Research and Development Center. Vicksburg, MS. 11 p.

Soomere, T., (2007). "Nonlinear Components of Ship Wake Waves," *Applied Mechanics Reviews* 60. pp 120-137.

Sorensen, R.M., (1967). “Investigation of Ship-Generated Waves.” *Journal of the Waterways and Harbors Division* 93(1). pp 85–99.

Sorensen, R.M., (1973). "Ship-generated waves," *Advances in Hydroscience* 9. pp 49-83.

Sorensen, R.M. & Weggel, J.R., (1985). "Development of ship wave design information," *Coastal Engineer*ing 1984. Presented at the 19th International Conference on Coastal Engineering, American Society of Civil Engineers, Houston, TX. pp. 3227-3243.

Sorensen, R.M., (1997). "Prediction of vessel-generated waves with reference to vessels common to the Upper Mississippi River system," *ENV Report 4*, Prepared for the Rock Island, St. Louis, and St. Paul U.S. Army Engineer Districts. 50 p.

Stumbo, S. & and Fox, K., (1998). “Prediction, measurement, and analysis of wake wash from marine vessels,” *Marine Tech* 36. pp 248-260.

Tate, J.N. & Berger, R.C., (2006). "Houston-Galveston Navigation Channels, Texas Project: Navigation Channel Sedimentation Study, Phase 1," Report No. ERDC/CHL TR-06-8. Coastal Hydraulics Lab, U.S. Army Corps of Engineers Engineer Research and Development Center, Vicksburg, MS. 126 p.

Tate, J.N., Berger, R.C., Ross, C.G., (2008). "Houston-Galveston Navigation Channels, Texas Project: Navigation Channel Sedimentation Study, Phase 2," Report No. ERDC/CHL TR-08-8. Coastal Hydraulics Lab, U.S. Army Corps of Engineers Engineer Research and Development Center, Vicksburg, MS. 183 p.

Thomson, W. (Lord Kelvin), (1887). “On ship waves,” *Transactions of the Institute of Mechanical Engineers* 8. pp 409–433.

Todd, F.H., (1967). “Resistance and propulsion,” *Principles of Naval Architecture*, Society of Naval Architects and Marine Engineers. Chapter 7.

Torrence, C. & Compo, G.P., (1998). "A practical guide to Wavelet analysis," A*merican Meteorological Society* 79(1). pp 61–78.

Torsvik, T., Dysthe, K., Pedersen, G., (2006). "Influence of variable Froude number on waves generated by ships in shallow water," *Physics of Fluids* 18. 11 p.

Torsvik, T. & Soomere, T., (2008). "Simulation of patterns of wakes from high-speed ferries in Tallinn Bay," *Estonian Journal of Engineering* 14(3). pp 232-254.

Torsvik, T., Soomere, T., Didenkulova, I., Sheremet, A., (2015). “Identification of ship wake structures by a time-frequency method,” *Journal of Fluid Mechanics* 765. pp 229-251.

United Nations (UN) (2017). "Review of Maritime Transport," *United Nations Conference on Trade and Development.* United Nations Publications. 114 p.

United States Coast Guard (USCG), (2020). "AIS Frequently Asked Questions," United States Coast Guard Navigation Center, Department of Homeland Security, Alexandria, VA. Webpage. URL https://www.navcen.uscg.gov/?pageName=AISFAQ

Velegrakis, A.F., Vousdoukas, M.I., Vagenas, A.M., Karambas, T., Dimou, K., Zarkadas, T., (2007). "Field observations of waves generated by passing ships: A note," *Coastal Engineering* 54. pp 369-375.

VesselFinder, (2020). Webpage. URL vesselfinder.com

Weggel, J.R. & Sorensen, R.M., (1986). "Ship Wave Prediction for Port and Channel Design," *Proceedings of the Ports '86*, ASCE Specialty Conference. Oakland, CA. pp 797-814.